SILICON NANOCAVITY LIGHT EMITTERS AT 1.3-1.5 μM WAVELENGTH

Abdul Shakoor

A Thesis Submitted for the Degree of PhD
at the
University of St Andrews

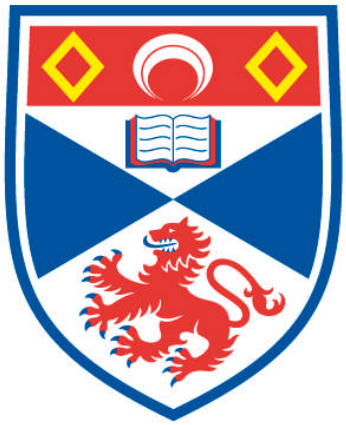

2013

Silicon nanocavity light emitters at 1.3-1.5 μm wavelength

Abdul Shakoor

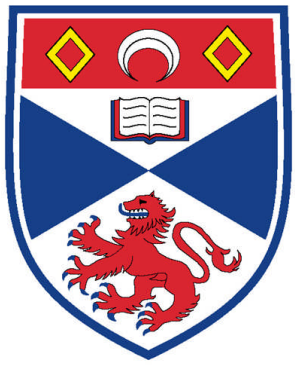

University
of
St Andrews

Thesis submitted for the degree of Doctor of Philosophy at the University of St Andrews

March 2013

To My Parents

Declarations

I, Abdul Shakoor, hereby certify that this thesis, which is approximately **40,000** words in length, has been written by me, that it is the record of work carried out by me and that it has not been submitted in any previous application for a higher degree.

I was admitted as a research student in March 2010 and as a candidate for the degree of Doctor of Philosophy in March 2010; the higher study for which this is a record was carried out in the University of St Andrews between 2010 and 2013.

Date: 15th March 2013 Signature of Candidate: _____

I hereby certify that the candidate has fulfilled the conditions of the Resolution and Regulations appropriate for the degree of Doctor of Philosophy in the University of St Andrews and that the candidate is qualified to submit this thesis in application for that degree.

Date: 15th March 2013 Signature of Supervisor: _____

In submitting this thesis to the University of St Andrews I understand that I am giving permission for it to be made available for use in accordance with the regulations of the University Library for the time being in force, subject to any copyright vested in the work not being affected thereby. I also understand that the title and the abstract will be published, and that a copy of the work may be made and supplied to any bona fide library or research worker, that my thesis will be electronically accessible for personal or research use unless exempt by award of an embargo as requested below, and that the library has the right to migrate my thesis into new electronic forms as required to ensure continued access to my thesis. I have obtained any third-party copyright permissions that may be required in order to allow such access and migration, or have requested the appropriate embargo below.

The following is an agreed request by the candidate and supervisor regarding the electronic publication of this thesis:

Access to printed copy and electronic publication of thesis through the University of St Andrews.

Date: 15th March 2013

Signature of Candidate: _____ Signature of Supervisor _____

Acknowledgements

First of all I would like to pay my regards and thanks to my parents. Without their support, motivation and prayers it would not have been possible for me to succeed. I am very grateful for their understanding about my continued absence.

I would like to thank Prof. Thomas Krauss and Dr. William Whelan Curtin for providing me with the opportunity to work on this interesting PhD project. Their guidance and help throughout the project is highly appreciated. Thank you for all the experimental, theoretical and administrative support throughout my PhD studies and for your highly valuable comments on my thesis report.

This work was supported by the Era-NET NanoSci LECSIN project which also involved the University of Catania and the University of Pavia, both based in Italy and Neel institute, based in Grenoble, France. I am thankful to all the people from these groups who were involved in this project. I would especially like to acknowledge the following people as they directly contributed to this project.

At the University of Pavia

Dr Roberto Lo Savio and Dr Matteo Galli for carrying out the photoluminescence measurements and for useful discussions.
Dr Simone Portalupi for his support in fabrication during his stay at St Andrews.
Dr Dario Gerace and Prof Lucio Andreani for useful discussions and theoretical support.

At the University of Catania

Dr Giorgia Franzò and Dr Paolo Cardile for ion implantation and annealing of the samples.
Dr Simona Boninelli for transmission electron microscopy of the samples.
Dr Maria Mirritello for deposition of erbium disilicate films.
Prof Francesco Priolo and Dr Alessia Irrera for useful discussions.

At my own University of St Andrews I would like to extend special thanks to Dr Christopher Reardon for his multi dimensional support, which included both scientific and administrative support. Thank you for proof reading my thesis and providing some eye catching artwork. Your effort to create a friendly environment and keeping the group together by organizing social activities are highly appreciated.

I would like to thank Dr Karl Welna for all the useful discussions and helping me to understand the modelling of photonic crystal cavities.

The technical support provided by Steve Balfour and Callum Smith is highly appreciated. Thank you for keeping all the equipment in order which allowed the experiments to run continuously. I am also grateful to Mr. Scott Johnston for taking care of posting the samples through out the project.

I would like to thank all my colleagues and friends at the department for providing a friendly working environment. Especially I am grateful to Dr Isabella, Dr Andrea, Dr Marco Grande, Dr Karl and Annett Klemm.

I would like to acknowledge the continuous support from my siblings, Dr Fatimah, Dr Aminah and Dr Bilal. Thank you for all your well wishes and support.

Finally, I would like to thank my examiners Prof Jonathan Finley and Prof Gerald Buller for taking out time from their busy routine to act as referees and Dr Tom Brown for acting as convener for my PhD exam.

Abstract

Silicon Photonics has been a major success story in the last decade, with many photonic devices having been successfully demonstrated. The only missing component is the light source, however, as making an efficient light source in silicon is challenging due to the material's indirect bandgap. The development of a silicon light source would enable us to make an all-silicon chip, which would find many practical applications. The most notable among these applications are on-chip communications and sensing applications.

In this PhD project, I have worked on enhancing silicon light emission by combining material processing and device engineering methods. Regarding materials processing, the emission level was increased by taking three routes. In all the three cases the emission was further enhanced by coupling it with a photonic crystal (PhC) cavity via Purcell effect. The three approaches taken in this PhD project are listed below.

1. The first approach involves incorporation of optically active defects into the silicon lattice by hydrogen plasma treatment or ion implantation. This process results in broad luminescence bands centered at 1300 and 1500 nm. By coupling these emission bands with the photonic crystal cavity, I was able to demonstrate a narrowband silicon light emitting diode at room temperature. This silicon nano light emitting diode has a tunable emission line in the 1300-1600 nm range.
2. In the second approach, a narrow emission line at 1.28μm was created by carbon ion implantation, termed "G-line" emission. The possibility of enhancing the emission intensity of this line via the Purcell effect was investigated, but only with limited success. Different proposals for future work are presented in this regard.
3. The third approach is deposition of a thin film of an erbium disilicate on top of a PhC cavity. The erbium emission is enhanced by the PhC cavity. Using this method, an optically pumped light source emitting at 1.54 μm and operating at room temperature is demonstrated.

A practical application of silicon light source developed in this project in gas sensing is also demonstrated. As a first step, I show refractive index sensing, which is a simple application for our source and demonstrates its capabilities, especially relating to the lack of fiber coupling schemes. I also discuss several proposals for extending applications into on-chip biological sensing.

List of Publications

A. Journal Papers

1. R. Lo Savio, M. Miritello, **A. Shakoor**, P. Cardile, K. Welna, L. C. Andreani, D. Gerace, T. F. Krauss, L. O'Faolain, F. Priolo, and M. Galli, "Enhanced 1.54 μm emission in Y-Er disilicate thin films on silicon photonic crystal cavities," (under review in optics express).

2. **A. Shakoor,** R. Lo Savio, P. Cardile, S. L. Portalupi, D. Gerace, K. Welna, S. Boninelli, G. Franzò, F. Priolo, T. F. Krauss, M. Galli and L. O'Faolain, "Room temperature all-silicon photonic crystal nanocavity light emitting diode at sub-bandgap wavelengths," Laser Photonics Rev. 7 (1) 114-121 (2013).

   Appeared as a front cover of a journal "Laser and Photonics Review", January (2013) issue.

3. **A. Shakoor**, R. Lo Savio, S. L. Portalupi, D. Gerace, L. C. Andreani, M. Galli, T. F. Krauss, and L. O'Faolain, "Enhancement of room temperature sub-bandgap light emission from silicon photonic crystal nanocavity by Purcell effect," Physica B 407, 4027-4031 (2012).

4. R. Lo Savio, S. L. Portalupi, D. Gerace, **A. Shakoor**, T. F. Krauss, L. O'Faolain, L. C. Andreani, and Matteo Galli, "Room temperature emission at telecom wavelengths from silicon photonic crystal nanocavities ," Appl. Phys. Lett. 98, 201106 (2011).

   Appeared as a research highlight in Nature Materials.
   Titled "Silicon does it" Nature Materials 10, 480 (2011).

Under preparation

5. S. Boninelli, **A. Shakoor**, R. Lo Savio, G. Franzò, M. Galli, T. F. Krauss, L. O'Faolain, and F. Priolo, "Hydrogen induced defects in Si photonic nanocavities," Journal of Applied Physics.

B. Conferences

B.1 Oral presentations

1. **A. Shakoor** et al, “Tunable Sub-bandgap silicon based light source at room temperature,” European Optical Society Annual Meeting (EOSAM), Aberdeen, United Kingdom, 25th -28th September (2012).
2. **A. Shakoor** et al, “Narrow linewidth silicon nano light source at telecommunication wavelengths,” Photon 12, Durham, United Kingdom, 3rd-6th September (2012).
3. **A. Shakoor** et al, “Enhancement of photoluminescence of silicon photonic crystal nanocavity by plasma treatment,” European Materials Research Society (EMRS), spring meeting, Nice, France, 9th-13th May (2011).

B.2 Poster Presentations

1. **A. Shakoor** et al, “Sub-bandgap photoluminescence of Si PhC nanocavity at room temperature,” IEEE Group IV Photonics, London, United Kingdom, 14th-16th September (2011).
2. **A. Shakoor** et al, “All silicon nanolight source at 1500 nm wavelength” JSPS international school on silicon photonics, Kyoto, Japan, 16th -19th November (2011).
3. **A. Shakoor** et al, “Light emission from silicon photonic nanostructures,” PhD summer school on silicon photonics, University of St Andrews, Scotland, 3rd-8th July (2011).
4. **A. Shakoor** et al, “Photonic crystal cavities in erbium implanted silicon on insulator,” PhD summer school on Nano Optics, Aarhus, Denmark, 3rd-7th September (2010).

B.3 Conference presentations by Collaborators

1. **A. Shakoor et al,** "Room temperature electrically pumped silicon nanolight source at telecommunication wavelengths," Photonics West, San Francisco, USA, 2^{nd} -7^{th} February (2013).
2. P. Cardile, **A. Shakoor**, R. Lo Savio, S. L. Portalupi, D. Gerace, K. Welna, S. Boninelli, G. Franzò, F. Priolo, T.F. Krauss, M. Galli and L. O' Faolain, " Electroluminescence from SOI photonic crystal cavities at telecommunication wavelengths," European Materials Research Society (EMRS), spring meeting, Strasbourg, France, 14^{th} -18^{th} May (2012).
3. M. Galli, L. O'Faolain, D. Gerace, R. Lo Savio, S. L. Portalupi, **A. Shakoor,** K. Welna, L. C. Andreani, T. F. Krauss, A. Irrera, G. Franzò, F. Priolo, "Light generation in silicon Photonic crystal cavities," IEEE Group IV Photonics, London, United Kingdom, 14^{th}-16^{th} September (2011) (invited).
4. R. Lo Savio, S. L. Portalupi, M. Galli, D. Gerace, L. C. Andreani, **A. Shakoor**, L. O'Faolain, T. F. Krauss, A. Irrera, G. Franzo', and F. Priolo, "Photoluminescence spectroscopy of silicon photonic crystal nanocavities," CLEO/Europe, Munich, Germany, May (2011).
5. L. O'Faolain, M. Galli**, A. Shakoor**, R. Lo Savio, S. Portalupi, K. Welna, D. Gerace, G. Guizzetti, L. C. Andreani, T. Krauss, A. Irrera, G. Franzo', and F. Priolo, "Enhanced light emission from silicon using photonic crystal nanocavities," Integrated Photonics Research, Silicon and Nanophotonics, Toronto, Canada, June (2011).
6. E. R. Martins, J. Li, **A. Shakoor**, and T. F. Krauss, "Scattering loss reduction in sub-wave length gratings for solar cell applications," Renewable Energy and the Environment, Austin, Texas, USA, November (2011).

TABLE OF CONTENTS

CHAPTER 3

ENHANCING SILICON EMISSION BY INCORPORATING HYDROGEN DEFECTS AND PURCELL EFFECT 60

CHAPTER 4

ROOM TEMPERATURE ALL-SILICON PHOTONIC CRYSTAL NANOCAVITY LIGHT EMITTING DIODE 101

CHAPTER 5

REFRACTIVE INDEX SENSING USING LIGHT EMISSION FROM SILICON PHOTONIC CRYSTAL NANOCAVITIES 119

Introduction

Silicon (Si), a group IV element in the periodic table, is the backbone of the electronics industry. Silicon is used as a single material platform for electronics devices. Following the success of silicon in the electronics industry, the possibility of using it for photonics devices has been investigated extensively within the last few decades to benefit from a number of advantages it can offer. These are: silicon is cheap, abundantly available in nature, its processing is easy with well established fabrication pilot lines and since electronics is based on silicon, it is relatively easy to merge the electronics and photonics functionalities on a single chip.

Silicon has already found some success in developing some high performance photonics components, especially the passive ones. If we review the progress of silicon based on-chip photonics components, it would become obvious that silicon photonics is on the road to success.

The area where silicon has not achieved much success so far is using it for the development of an efficient light source, either a laser or a light emitting diode. It is difficult to make a light source in silicon due to its indirect bandgap. Due to the indirect bandgap of silicon, the electrons and holes have different momentum and since photons have a negligible momentum, the momentum conservation would not be established for the radiative recombination. Only if a third particle, a phonon, with the correct momentum is involved, the carriers will combine radiatively. Thus, the probability of radiative emission is very low in silicon, causing the development of an efficient silicon light source very challenging. If the radiative recombination rate in silicon could be increased, it would be possible to make silicon based light sources having emission levels that can be used for practical applications. One such application can be to use its emission to make an on-chip refractive index sensor. This could give rise to a cheap, disposable, easy to use gas or biological sensor, which would constitute a real application.

The effort to develop an efficient silicon light source is mostly driven by the silicon photonics community for its on-chip communication applications. As time progresses, the demands of higher data processing speeds and bandwidths have increased manifold. So far, the semiconductor industry has been successful in increasing the processing

speeds and bandwidths by first increasing the on-chip integration density of the components and then increasing the number of cores. So far successful, but this approach will soon reach its limit due to high losses of copper interconnects and unavoidable capacitive delays in the electronic chip. High integration density means long electrical interconnects being squeezed into a very small area, also causing thermal and electromagnetic interference issues. These fundamental limitations in electronic chips indicate that soon, a purely electronic approach will reach its limit and the use of alternate data carriers, which can offer higher speeds and bandwidths, becomes inevitable. This has prompted research into the use of photons instead of electrons as the data carriers, offering higher data processing speeds and bandwidths. This approach has the added advantage of low loss and lack of electromagnetic interference. Due to these advantages, the future of using light instead of current has been predicted in the famous saying "Today, optics is a niche technology. Tomorrow, it's the mainstream of every chip we build" (Patrick Gelsinger, Intel Sr. Vice President).

The advantage of having higher speeds and bandwidths is meaningful only if there is a high integration density of the photonic components which requires miniaturized devices. High integration density is easier to achieve if a single material platform is used, as in electronics, a field whose success can be attributed to the fact that it managed to find a single material platform. This helped to simplify and standardize the fabrication processes and enabled the making of miniaturized devices. Similarly, if we want to have widespread applications of on-chip photonics, a single material platform will be required. The question arises: which material is most suitable for this purpose? The choice of material depends on number of factors, including good optical properties to make efficient components, low cost, abundance in nature, easy processing, ease of integration with electronics and others. Considering the fact that silicon is available in abundance in nature, it is cheap, the mass-manufacturing of silicon components is well-established and that all electronics is based on silicon, contributes to making the integration of photonic and electronic functionality on a single chip easier. Therefore, silicon seems to be the most suitable material platform for integrated photonics. Although silicon seems a feasible choice based on the factors discussed above, the most fundamental requirement is that of a light source. Except for the development of a light source, silicon has achieved good progress in developing all essential components.

Waveguides with low optical losses [1,2] and small cross sections [3] have been demonstrated by using silicon on insulator (SOI) technology. Silicon detectors can be made, even though this is not very straight forward at telecommunication wavelengths (1300-1600 nm), as silicon does not have absorption in this range; some alternative approaches such as using Ge/Si [4] or the incorporation of defect states [5] have been successful, however. Similar to detectors, it is also not very straightforward to make modulators in silicon due to its centrosymmetric crystalline structure. Silicon lacks the linear electro-optic Pockels effect, which is typically used for electro-optic modulation, so the plasma dispersion effect (injection or depletion of carriers to change the refractive index) or the electro absorption effect in GeSi, showing modulation speed of 40 GHz [6,7] are being used. Thus, in terms of passive components, signal modulation and detection, silicon photonics has shown very promising progress.

The real challenge to date remains the development of an efficient light source. This lack of light source is the only remaining hurdle for using silicon as a single material platform for photonic chips. To overcome this issue, the present solution is to bond light sources made in the direct bandgap III-V materials onto silicon chips, also termed “hybrid integration” [8]. This method works, but is not fully compatible with CMOS processing as well as incurring significant cost. The real solution lies in the development of an efficient light source in silicon itself. The desired features of this light source are: room temperature operation, electrical pumping, small size, sub-bandgap emission (for interconnect applications) and narrow emission line. All these requirements are difficult to meet, but in the last decade, a lot of progress in the enhancement of silicon light emission has been made. Notable among these are the use of quantum confinement in silicon nanocrystals to demonstrate electroluminescence (EL) [9] and optically pumped gain [10] in the visible and near infrared range, stimulated emission in the quantum wells by utilizing quantum confinement approach as well [11]. Optical gain has been demonstrated by incorporation of rare earth ions into silicon [12] with optically pumped transparency demonstrated in erbium doped silicon nitride cavities [13]. An optically pumped silicon laser based on Raman effect has been demonstrated [14] but the size of the device is large (cm scale) which precludes large integration density, thus not offering much advantage over the hybrid approach. Furthermore, there is no possibility of electrically pumping this device. A direct

transition can be achieved by using highly doped strained germanium to demonstrate optically and electrically pumped lasing [15-17]. Silicon light sources based on defect luminescence have also been demonstrated [18,19]. All these techniques have shown some promise but they do not combine all the features listed above as either they operate only at low temperature [19], have emission at the band-edge [11,18] or lower wavelengths [9,10] where silicon is intrinsically absorbing, or are too large in size [14]. Details of these different approaches along with their shortcomings are discussed in detail in Chapter 1.

The aim of this PhD work is to try and solve the problem of the low radiative recombination rate in silicon, to enhance its emission and to demonstrate a silicon light source that combines all the features listed above. The approach taken is to combine material processing techniques to enhance the emission from silicon and to combine this with device engineering to further enhance it. The emission from silicon is first enhanced by the incorporation of optically active defects by hydrogen plasma treatment or ion implantation, which constitutes the material processing aspects. Using this approach, followed by forming gas annealing (FGA), a 500x enhancement of the sub-bandgap photoluminescence (PL) compared to the PL level of as-bought silicon on insulator wafer at same wavelengths is achieved. This enhanced PL from silicon material is then further increased by coupling it with a photonic crystal nanocavity by exploiting the Purcell effect. The nanocavity provides a narrow emission line with a further 300-fold enhancement, thus having overall 150,000 times higher PL level compared to the PL from the as-bought silicon on insulator (SOI) wafer. Using this approach, I was able to demonstrate an electrically pumped, all-silicon nanolight source that operates at room temperature and that has a narrow emission line tunable over the entire telecommunication (1300-1600 nm) range. The output power of this device is 5 pW (integrated over the fundamental emission line) or 45 pW (integrated over the whole 1100-1600 nm band) with a power spectral density of 10 pW/nm. This value of power spectral density is the highest ever reported from any silicon emitter, even without restricting the room temperature and sub-bandgap operation. Though these power levels are not yet sufficient for on-chip interconnect application, which requires power levels in the micro-watt range yet our light source can find applications in the gas/biological sensing, which do not require higher power levels.

In addition to enhancing emission by hydrogen plasma treatment and ion-implantation, two other approaches to make a silicon light source are investigated. One is using the 1.54 μm emission of erbium by either doping it in silicon or by depositing a layer of erbium compound on top of the silicon photonic crystal (PhC) cavity. The investigations show that doping silicon with erbium is not a very successful technique as the erbium emission line does not couple with the cavity to benefit from the Purcell effect. In contrast, depositing an erbium compound on top of the PhC cavity is a promising approach. Using this approach, a silicon light source with an output power of 85 pW has been demonstrated. The third approach is to create a narrow emission line in silicon by carbon implantation. This emission line is called the G-line and has a wavelength of 1.3 μm. We found out that the G-line does not work well with PhC cavities because the lifetime of the carriers at the etched side walls of PhC is too short, which compromises the G-line emission that has a long lifetime.

Thesis outline

The thesis is divided into 8 Chapters. Chapter 1 presents a detailed discussion of the lack of silicon light emission, followed by an overview of the different approaches taken to enhance the emission from silicon, including their shortcomings as well as introducing the approach taken in my project.

In Chapter 2, I present the design of a photonic crystal cavity with a high quality factor and a low mode volume. The details of our fabrication method for making photonic crystal structures is given, followed by a discussion of the optical setups used to measure the quality factors (Q-factors) and the photoluminescence of PhC cavities throughout the project.

In Chapter 3, I present all the results related to the defect luminescence in silicon, the hydrogen plasma treatment and the hydrogen ion implantation. Enhancement of silicon emission by both material processing and device engineering is also discussed.

In Chapter 4, I introduce an all-silicon PhC nanocavity light emitting diode based on the defect luminescence discussed in Chapter 3. The practical application of this device for refractive index sensing is described in Chapter 5.

Chapter 6 discusses the possibility of inducing a narrow emission line, i.e. the G-line into silicon by carbon implantation and describes my efforts to make an efficient silicon light source in this system. The challenges associated with G-line-PhC cavity system are discussed and alternate approaches for future work are presented.

Chapter 7 summarizes the results and discussion of using erbium emission to make a silicon light source. I discuss the problems associated with such an erbium doped silicon PhC cavity and present an alternate and successful approach of depositing a layer of erbium compound on top of the PhC nanocavity. Using this approach, I demonstrate a silicon light source operating at room temperature.

In Chapter 8, I conclude the work and provide recommendations for future work.

References

[1] E. Cortesi, F. Namavar, and R. A. Soref, “Novel silicon on insulator structures for silicon waveguides,” IEEE SOS/SOI technology conference (cat. No 89CH2796-1), Stateline, NV, USA: IEEE,109 (1989).

[2] J. Schmidtchen, A. Splett, B. Schuppert, and K.Petermann, “Low loss integrated-optical rib waveguides in SOI,” IEEE international SOI conference proceedings (Cat. No. 91CH3053-6), 142-143 (1991).

[3] S. P Chan, C. E Png, S. T. Lim, V. M. N. Passaro, and G. T. Reed, “Single mode and polarization independent SOI waveguides with small cross section,” J. Lightwave Technol. 23, 1573-1582 (2005).

[4] Y. Kang, et al., “Monolithic Ge/Si avalanche photodiodes with 340 GHz gain-bandwidth product,” Nat. Photonics 3, 59-63 (2009).

[5] A. P Knights, J. D. B Bradley, S. H. Gou, and P. E. J Jessop, Vac. Sci. Technol. A. 24, 783-786 (2006).

[6] J. Liu, D. Pan, S. Jongthammanurak, K. Wada, L. C. Kimerling, and J. Michel, “Design of monolithically integrated GeSi electro-absorption modulators and photodetectors on a SOI platform,” Opt. Express 15, 623-628 (2007).

[7] L. Liao, A. Liu, D. Rubin, J. Basak, Y. Chetrit, H. Nguyen, R. Cohen, N. Izhaky and M. Paniccia, “40Gbit/s silicon optical modulator for high speed applications,” Electron. Lett. 43, 22 (2007).

[8] K. Tanabe, K. Watanabe, and Y. Arakawa, “III-V/Si hybrid photonic devices by direct fusion bonding,” Sci. Rep. 2, 349 DOI:10.1038/srep00349 (2012).

[9] A. Marconi, A. Anopchenko, M. Wang, G. Pucker, P. Bellutti, and L. Pavesi, “High power efficiency in Si-nc/SiO_2 multilayer light emitting devices by bipolar direct tunneling,” Appl. Phys. Lett. 94, 221110 (2009).

[10] L. Pavesi, L. Dal Negro, C. Mazzoleni, G. Franzò and F. Priolo, “Optical gain in silicon nanocrystals,” Nature 408, 440-444 (2000).

[11] S. Saito, Y. Suwa, H. Arimoto, N. Sakuma, D. Hisamoto, H. Uchiyama, J. Yamamoto, T. Sakamizu, T. Mine, S. Kimura, T. Sugawara, and M. Aoki, “Stimulated emission of near-infrared radiation by current injection into silicon (100) quantum well,” Appl. Phys. Lett. 95, 241101 (2009).

[12] Hak-Seung Han, Se-Young Seo, and Jung H. Shin, "Optical gain at 1.54 μm in erbium-doped silicon nanocluster sensitized waveguide," Appl. Phys. Lett. 79, 4568 (2001).

[13] Y. Gong, M. Makarova, S. Yerci, R. Li, M. J. Stevens, B. Baek, S.W. Nam, L. Dal Negro, and J. Vuckovic, "Observation of Transparency of Erbium-doped Silicon nitride in photonic crystal nanobeam cavities," Opt. Express 18, 13863-13873 (2010).

[14] H. Rong, R. Jones, A. Liu, O. Cohen, D. Hak, and A. Fang, "A continuous-wave Raman silicon laser," Nature 433, 725-728 (2005).

[15] J. Liu, X. Sun, R. Camacho-Aguilera, L. C Kimerling, and J. Michel, "Ge-on-Si laser operating at room temperature," Opt. Lett. 35, 679-681 (2010).

[16] X. Sun, J. Liu, L.C. Kimerling and J. Michel, "Room-temperature direct bandgap electroluminescence from Ge-on-Si light-emitting diodes," Opt. Lett. 34, 1198-1200 (2009).

[17] R. E. Camacho-Aguilera, Y. Cai, N. Patel, J. T. Bessette, M. Romagnoli, L. C. Kimerling, and J. Michel, "An electrically pumped germanium laser" Opt. Express 20, 11316-11320 (2012).

[18] W. L. Ng, M. A. Lourenço, R. M. Gwilliam, S. Ledain, G. Shao, and K.P Homewood, "An efficient room-temperature silicon-based light-emitting diode," Nature 410, 192-194 (2001).

[19] S. G Cloutier, P. A Kossyrev, and J. Xu, "Optical gain and stimulated emission in periodic nanopatterned crystalline silicon," Nat. Materials 4, 887-891 (2005).

Chapter 1

Literature review and approach in this PhD project

1.1 Silicon - a poor emitter of light

Silicon is a group IV element with an indirect bandgap. This means that the valence and conduction band minima do not occur at the same point in momentum-space, as shown in Figure 1.1. Since photons of the bandgap energy have negligible momentum, this momentum mismatch cannot be easily overcome and radiative emission is a slow process. Radiative recombination requires the assistance of the third particle, namely a phonon, to compensate for the momentum mismatch. The probability of finding a phonon with the correct momentum to facilitate the radiative recombination is very low,

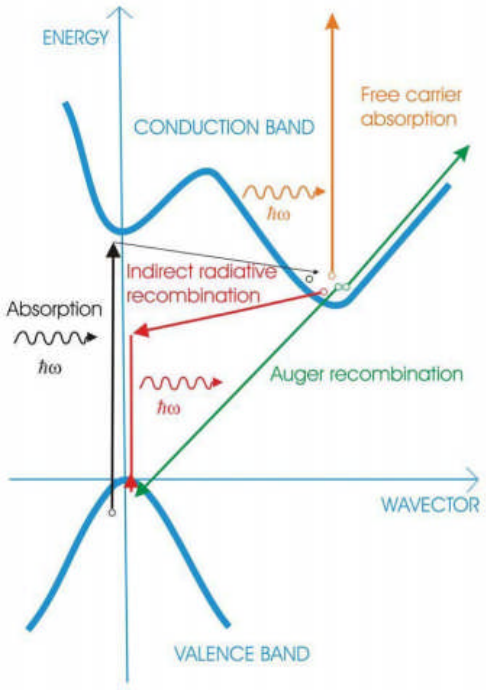

Figure 1.1: Energy diagram of silicon showing different transitions. Figure reproduced from [1][1].

which causes the low radiative rate; non-radiative processes may therefore dominate. The main routes for non-radiative recombination are Auger recombination and

recombination of carriers at surface states. In Auger recombination, the energy released by the recombination of carriers is given to another electron, which moves to a higher energy level within the same band, shown by the green arrow in Figure 1.1. This excited electron relaxes back with the release of the excess energy as thermal vibrations. A further loss mechanism is free carrier absorption (FCA), shown by the orange arrow in Figure 1.1. In this process, the excited electron absorbs the energy from the incident photon and occupies an unfilled state in the same conduction band. The indirect bandgap of silicon with various possible recombination mechanisms is shown in Figure 1.1. Thus, silicon is a poor emitter of light due to its indirect bandgap, which impedes the efforts to make an efficient silicon-based light source.

1.2 Requirements of a silicon light source

In addition to the need for enhancing the radiative emission from silicon to increase the radiative efficiency and output intensity, the silicon light source should also have the following features to find practical applications:

1. Room temperature operation: For use in our daily life, the silicon light source should operate at room temperature.
2. Electrical pumping: Though, in some applications optical pumping might be sufficient but for ease of use and integration with electronic components, the silicon light source should ideally have the ability to be pumped electrically.
3. Small size: To enable high on-chip integration density, the light source should have small dimensions, preferably in nano-scale.
4. Sub-bandgap operation: For applications in on-chip communications, the emission wavelength of the silicon light source should be above 1.1 μm, i.e, the band-gap of silicon.
5. Tunability: To find a wide spectrum of applications, the emission wavelength of the silicon light source should have a tunable range.
6. Narrow emission line or laser-like operation to have a spectrally pure signal and to allow multiple spectral channels to be used.
7. Output power in the range of microwatts and above to allow applications in on-chip communications.

In the following sections, I give a brief overview of the different approaches taken by researchers around the globe to enhance the silicon emission and evaluate those approaches against the requirements listed above.

1.3 Different approaches to enhance silicon emission

As discussed above, silicon is a poor emitter of light. Thus, some alternate approaches are required to overcome the non-radiative recombination in silicon. During the last decade, the following three main routes have been taken by researchers to increase the emission efficiency of silicon and to make a practical light source.

1. Stimulated Raman scattering based silicon laser
2. Erbium doping
3. Quantum confinement based silicon light sources

Next, I present a brief overview of these three approaches, with their advantages and shortcomings highlighted.

1.3.1 All-silicon Raman laser

The most popular silicon laser is based on stimulated Raman scattering (SRS) [2-5]. The gain coefficient of SRS in silicon is almost four orders of magnitude higher than in silica fiber. Also, due to the large refractive index of silicon, the optical mode can be confined to a much smaller area in a Si waveguide than in an optical fiber. Due to these factors, Raman gain can be achieved with chip-scale silicon devices of typically a few cm lengths. Optical gain based on SRS was first demonstrated in planar silicon waveguides [6] at room temperature. The schematic of the silicon waveguide based continuous-wave (CW) Raman laser featuring a *pin* junction to sweep out free carriers is shown in Figure 1.2(a).

The demonstration of an all-silicon Raman laser was a remarkable achievement and it overcame the prejudice that it was impossible to make a laser in silicon. Unfortunately, this device has two serious shortcomings. First, it is optically pumped and since it is based on an all-optical phenomenon, there is no possibility of electrical pumping in the future either. Secondly, the dimensions of the device are quite big, which precludes large scale integration density. Due to these two shortcomings, this device has not been able to find any practical application and it remains a research curiosity.

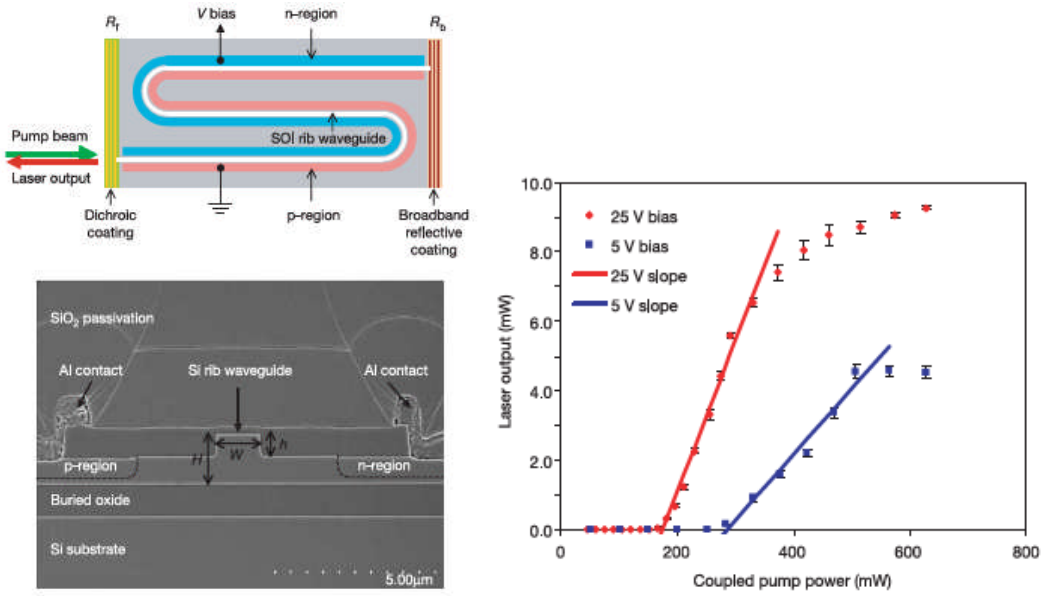

(a) (b)

Figure 1.2: (a) Schematic and SEM picture of the Si rib waveguide based CW pumped Raman laser. (b) The input vs. output power curve of the device clearly displays threshold behaviour. Figure reproduced from [4][2].

1.3.2 Erbium doping

Erbium belongs to the series of rare earth elements of the periodic table. It has an electronic configuration of $[Xe]4f^{12}6s^2$. Erbium can exist in two oxidation states as an ion by losing either two or three electrons to form Er^{2+} or Er^{3+}, respectively. The Er^{2+} ion is rare and the element mostly exists in the Er^{3+} state. Erbium has been of great interest to the photonics community due to its capability of emitting light in the near IR range. Especially, the radiative transition from the first excited state ($^4I_{13/2}$) to the ground state in Er^{3+} ion emits light at 1.5 µm. Er^{3+} has absorption bands at 1480 nm and 980 nm. This corresponds to transitions from the ground state to the $^4I_{13/2}$ and $^4I_{11/2}$, respectively. The transitions from the ground state to $^4I_{9/2}$ and $^4S_{3/2}$ correspond to absorption at 800 nm and 520 nm, respectively. The energy level diagram of Er^{3+} is given in Figure 1.3(a). Erbium can be introduced in silicon by ion implantation or by molecular beam epitaxy (MBE) [7].

Erbium has been investigated as a dopant in bulk silicon to increase its emission at 1.5 μm [8-12]. So far, there is only little progress in developing Si light sources based on erbium doping because the approach faces number of challenges which are described below.

1.3.2.1 Challenges in erbium doped silicon

1. Energy back transfer

The first problem is the energy back transfer from Er^{3+} ions back to silicon, which reduces the emission intensity [13]. This energy transfer is due to the creation of a defect state due to erbium implantation. This defect state lies within the bandgap of silicon and couples with the Er^{3+} levels, causing the energy back transfer. The problem of energy back transfer can be solved if bandgap of silicon is increased so that the defect state and Er^{3+} level do not couple resonantly [14].

2. Solubility problem

The second problem with erbium doped silicon is the low solubility of erbium in the silicon host. The ionic bond mismatch and the sp^3 bonding of the host silicon are two causes for the low solubility that can be achieved by equilibrium methods. Using ion implantation, the maximum doping density can be increased but that too is limited to 3×10^{17} cm^{-3} [15]. Increasing the doping concentration further forms erbium aggregates, which facilitate the formation of optically inactive clusters and silicides [16]. The erbium concentration in silicon can be increased by co-doping it with impurities like oxygen [17,18]. Co-doping erbium with oxygen has the extra advantage of enhancing the luminescence and improving the emission at higher temperatures.

3. Temperature quenching problem

Erbium emission is obtained only at cryogenic temperatures because non-radiative recombination dominates at higher temperatures. The erbium emission intensity is suppressed by four orders of magnitude on increasing the temperature from cryogenic to room temperature, an effect that can be reduced by co-doping the erbium with oxygen. Using this route, erbium doped Si LED, with 0.1 % external quantum efficiency at room temperature has been demonstrated[10], Figure 1.3(b).

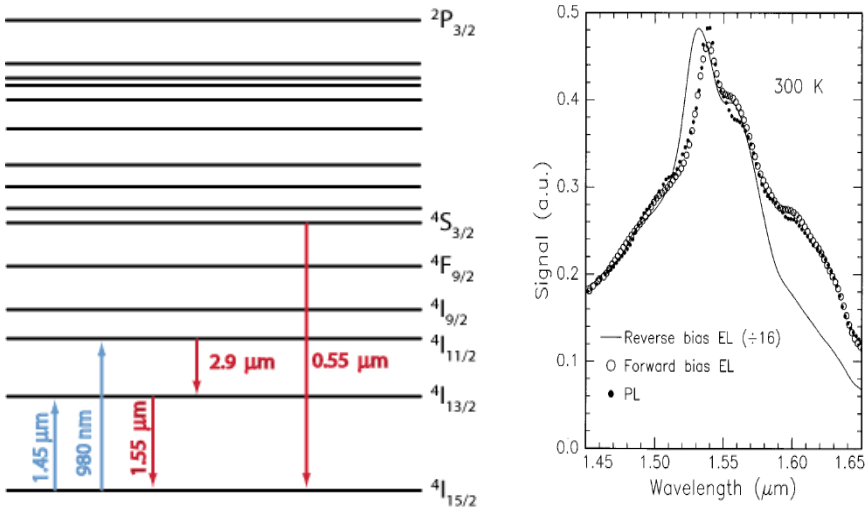

(a) (b)

Figure 1.3: (a) Energy level diagram of Er^{3+}. (b) EL signal from erbium doped silicon at room temperature under forward and reverse bias conditions. Figure reproduced from [10][3].

1.3.3 Enhancement of silicon light emission by quantum confinement

The momentum conservation rule can be relaxed if the carriers are quantum confined. This follows the Heisenberg uncertainty principle, which states that "if the position of a particle is confined, its momentum becomes uncertain". Thus, if the electrons are localized, their momentum becomes uncertain, which can be helpful to solve the problem of momentum mismatch due to indirect bandgap of silicon. In other words, if the carriers are confined in a very small real space, their momentum space will be broad. This helps to conserve the momentum and overlap of the wave functions of electrons and holes. Thus, the probability of radiative recombination will be enhanced. Utilizing quantum confinement, two different approaches have been used in past. These approaches are listed below.

i. Silicon nanocrystals or quantum dots

ii. Defect luminescence

1.3.3.1 Silicon nanocrystals

One approach where quantum confinement is utilized for silicon light emission enhancement is using silicon nanocrystals (Si-NC) embedded in the silica matrix

[19,20]. The emission spectrum of Si-NC is broad (600-1000 nm) and depends on its size, which can be controlled during the manufacturing process. The broad emission can be due to an aggregate of emission events at different wavelengths by different sized crystals or the emission from each Si-NC can be broad itself [21,22]. The exact mechanism of emission from Si-NCs is not known but the emission is believed to be due to following two mechanisms:

1. The recombination of electrons and holes, which are quantum confined in the nanocrystal [23]. The electron lies in the conduction band and hole in the valence band. Due to quantum confinement, their wave functions overlap. Their recombination emits photons of energy equal to the bandgap energy.
2. The recombination of carriers at some defect site located at the interface of the nanocrystal and silica [24]. These defects sites create carrier confinement and help in their radiative recombination by creating energy levels that lie within the bandgap. The double silicon-oxygen bond is believed to be the defect center, which confines the carriers and is responsible for the emission [25]. Some defect sites can also act as non-radiative recombination centers and require passivation to avoid those.

The two mechanisms listed above are shown schematically in Figure 1.4.

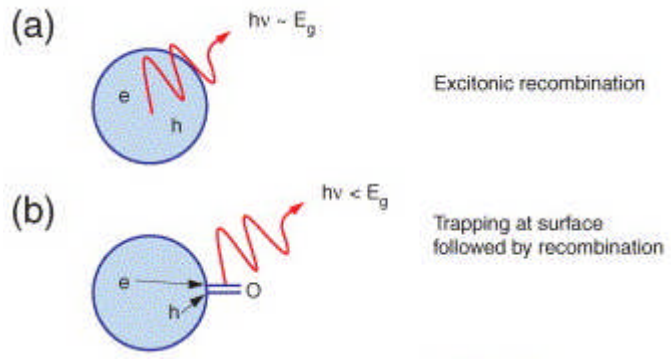

Figure 1.4: Two recombination mechanisms responsible for the light emission in Si-NC. (a) Recombination of confined electron and hole emitting a photon of the bandgap energy. (b) Radiative recombination of carriers at the surface defect centres. Figure reproduced from [26][1].

Optical gain has been observed in Si-NC in earlier reports by different groups [19,27-29]. An optical gain of 25-30 cm^{-1} was reported in [19]. After the discovery of optical gain in Si-NC, a lot of effort was invested in developing practical light sources based on this effect. An LED, with a power efficiency of 0.17 % based on multilayer Si-NC embedded in silica was demonstrated by using the bipolar current injection [20]. Yet the effort to convert optical gain into lasing by placing the gain medium inside the cavity has not been successful so far [30]. Some groups have even reported lack of net gain in Si-NCs [31].

Erbium doping of Si-NC embedded in a silica matrix has been used [32] to increase the emission intensity and shift the emission wavelength to 1.5 μm. In this case, the energy of the photon emitted by the excitonic recombination at the Si-NC is transferred efficiently to the erbium ion, which lies at the close proximity. Using erbium doped Si-NC waveguides, an amplifier has been reported [33] with an optical gain of 7 dB/cm [33].

1.3.3.2 Defect luminescence

Another approach to increase the Si emission by exploiting the quantum confinement phenomenon is by creating point defects in the Si lattice. The defects created in Si lattice are very small in size, where carriers can be quantum confined. Thus, these point defects are very narrow in real space, hence very broad in the momentum space, as shown in Figure 1.5. The defects form a midgap state that gives rise to the third level, and that turns the recombination of electrons and holes into a three level system. The carriers get trapped in this defect state, where they recombine radiatively without the assistance of phonons. This enhances the emission efficiency of silicon. The mechanism of enhancing the radiative recombination by creating midgap defect states in silicon to provide conservation of momentum is demonstrated in Figure 1.5.

Different groups have demonstrated an enhancement of Si light emission by introducing different types of defects [35-38]. A brief overview of different types of emission bands or lines created by introduction of impurities or defects in silicon is given next.

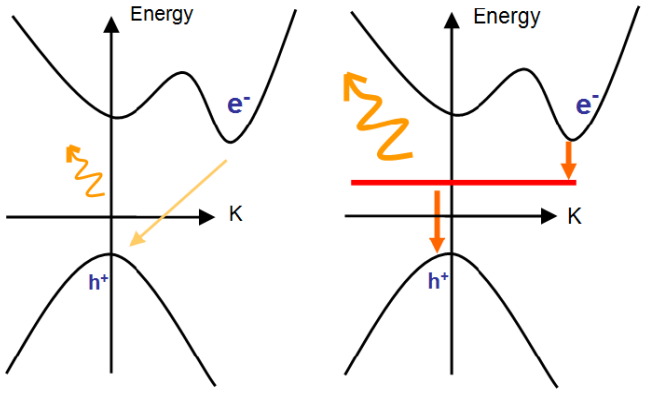

(a) (b)

Figure 1.5: (a) Indirect bandgap of silicon. The small "photon" arrow indicates a low probability of photon emission due to the momentum mismatch of carriers. (b) The larger arrow indicates an increase in the probability of photon emission by the creation of a midgap defect state that provides momentum conservation [34][4].

1.3.3.2.1 D-lines created by dislocation loops

Dislocation loops are 1-dimensional defects in the crystal lattice. The introduction of dislocation loops disturbs the translational symmetry of the crystal. This gives rise to the energy levels within the bandgap, which facilitates the recombination of carriers by quantum confinement and gives rise to emission bands. Dislocation loops can be introduced by applying stress on the crystal or by ion implantation. In [35], the emission bands at sub-bandgap wavelengths were reported at low temperature via the introduction of dislocation loops in silicon, as shown in Figure 1.6(a). Later, W. L. Ng *et al.* [36] introduced dislocations via ion implantation and thermal processing to demonstrate a silicon light emitting diode. Using this approach, electroluminescence was also demonstrated at room temperature. The spatial confinement of the radiative carriers due to the introduction of dislocation loops localizes them and reduces the probability of recombining non-radiatively elsewhere in the crystal. This helps to suppress the thermal quenching of emission. The output power of the device was 19.8 µW at 100 mA input current, producing an external quantum efficiency of 10^{-4}. The main emission peak from this device is at the Si band-edge (around 1160 nm) with the

full width half maximum (FWHM) of 80 nm. No emission band or line was observed at any other wavelength, indicating that the spatial confinement of carriers is at the Si-bulk region. The EL from the device with forward bias at different temperatures is shown in Figure 1.6(b).

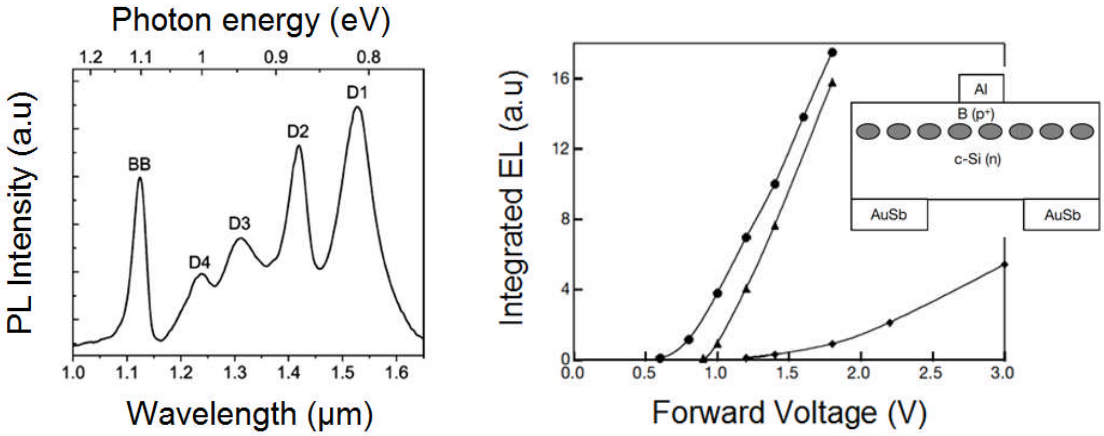

(a) (b)

Figure 1.6: (a) Set of D-lines (D1-D4) formed by introducing dislocation loops [35]. The BB line is due to band-edge emission. (b) The EL of dislocation loops based silicon LED at forward bias for different temperatures. 80 K (diamonds), 180 K (triangles), room temperature (diamonds) [36][5].

Advantages/drawbacks

The main advantage of the dislocation loop device is that it operates at room temperature and is electrically driven. On the other hand, the emission wavelength is at the silicon band-edge, which means that on-chip routing cannot be used, as the silicon material is still absorbing. Furthermore, the emission linewidth is large (80 nm). The size of the device is also big, which would preclude the large scale integration density of the photonic components, compromising on the advantage of using the single material platform.

The device can be improved by coupling the emission with a cavity, to get the sharp emission peak, corresponding to the resonance of the cavity. The resonance wavelengths can also be shifted to near IR range by using Si alloys, e.g. silicon carbide.

1.3.3.2.2. Narrow defect emission lines

The silicon emission has been enhanced by creating narrow emission lines in silicon by introducing different impurities in the silicon lattice [37-39]. Most promising among these are G-line at 1278 nm [37] and W-line at 1218 nm [38]. A brief discussion on work done on these two lines is given below.

1.3.3.2.2.1. G-line based silicon light source

Narrow emission lines have been created by exploiting the carbon and oxygen impurities present in silicon. The complex of interstitial carbon and interstitial oxygen ($C_i - O_i$) creates the C-line with an emission wavelength of 1.56 µm. Similarly, the complex of interstitial carbon and substitutional carbon ($C_i - C_s$) gives rise to the G-line, emitting at 1.3 µm [40]. The G-line can be created in silicon by electron irradiation [40], carbon implantation or by exposure to CF_4 plasma [41]. I have given more detail on G-line emission in Chapter 6.

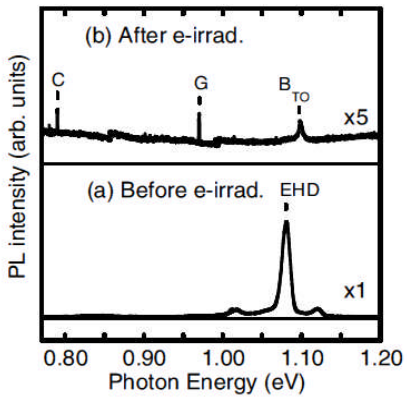

Figure 1.7: C-line and G-line formation by electron irradiation. Figure reproduced from [40][6].

Making use of the G-line, optical gain and stimulated emission have already been demonstrated in nano-patterned silicon [37]. There, the G-line was observed after the patterning of PhC structures on Si. We assume that the G-line was created during the etching of nanostructures by using carbon containing gases. The same line was not observed in the unpatterned sample. Figure 1.8(a) shows the G-line emission from patterned silicon with its stimulated emission behaviour in 1.8(b). Linewidth narrowing was also observed after the threshold, which is a signature of the stimulated emission

[42]. In this device, an optical gain of 260 cm^{-1} was measured, much higher than with Si-NCs (30 cm^{-1}).

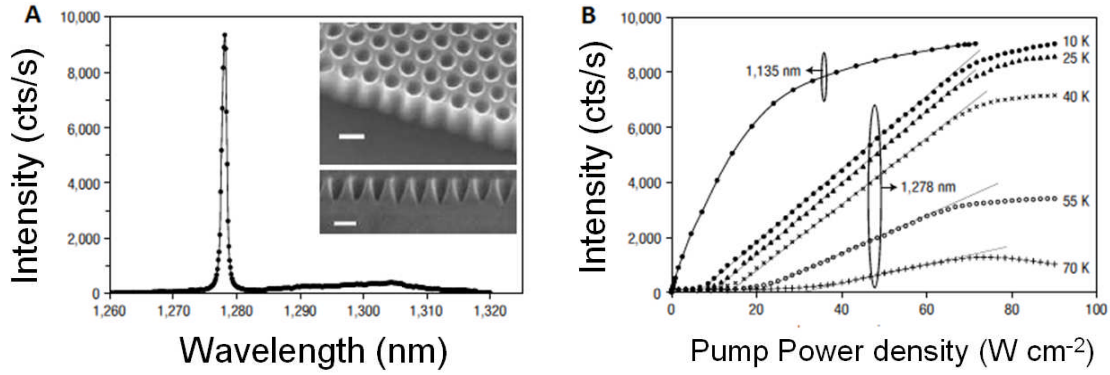

Figure 1.8: (A) The creation of an emission line at 1278nm by nano-patterning of silicon. The nano-patterned structures are shown in the inset. (B) Transition from spontaneous to stimulated emission by increasing the input power for the 1278 nm line. The same transition is not observed for silicon band-edge emission. Figure reproduced from [37][7].

Drawback

The demonstration of stimulated emission and optical gain by using the emission line arising from the introduction of carbon complexes is quite impressive. One major drawback, which makes this approach less practical is that it works only at cryogenic temperatures. Furthermore, the device is optically pumped, while for practical applications, electrical pumping is preferred. Thus, although this approach shows promise in terms of demonstrating gain and stimulated emission, it has not been very successful overall and the search for a sub-bandgap Si light source operating at room temperature is still on.

Similar to the G-line, another emission line, called the W-line has been demonstrated at 1218 nm. The W-line is created by silicon ion implantation to create silicon interstitials. Bao *et al.* [38] have demonstrated electrically pumped W-line emission from silicon with emission power in the nW range at low temperature. Unfortunately, the W-line is only observed at low temperature.

1.3.3.2.3 Hydrogen related defects

Hydrogen is largely used for the passivation of defects in silicon [43]. Also, during the reactive ion etching of silicon, hydrogen gas is often present in the chamber. In the 1980s and 1990s, the effect of hydrogen plasma on silicon was extensively studied [44-57]. It was found out that in addition to its passivating effect, hydrogen plasma also introduces defects into the silicon itself [44-57]. These defects are detrimental to the electronic properties of silicon. Hence, the main motivation for these studies was to understand and characterize these defects, so that they can be avoided. Many techniques were used, including transmission electron microscopy studies [50-53], Raman studies [57] and deep-level transient spectroscopy studies (DLTS) [58]. In addition to these techniques, photoluminescence analysis was also carried out in hydrogen plasma treated Czochralski silicon (Cz-Si) at low temperature [45-48, 54-56]. Broad sub-bandgap PL bands were observed, as shown in Figure 1.9(a).

The exact nature of the defects, the origin of the PL bands and the role of hydrogen in the emission process are not clearly understood. Many conflicting reports are found in the literature [45-47]. For example, in [47], the in-diffusion of hydrogen into silicon is considered to be responsible for creating the platelets, which are stabilized by hydrogen by creating H-Si bonds. The in-diffusion of hydrogen is considered to be responsible for creating these platelets and not the plasma damage. This report is contradicted by [45,46], where it has been shown that the in-diffusion of hydrogen alone does not induce the PL bands and plasma damage is necessary for the observed emission. Furthermore, the authors in [45,46] claim that the recombination of carriers occurs at intrinsic microdefects rather than at the hydrogen stabilized platelets as claimed in [46]. Most reports agree that the hydrogen plasma exposure introduces the platelets in (111) and (100) orientation with an average diameter of 10 nm within 100 nm depth [50-53] with the most convincing model explaining the origin of sub-bandgap PL band reported in [53]. The origin of PL bands is related to the radiative recombination of carriers that are trapped at these platelets.

According to the model explained in [53], there is a strong compressive strain field surrounding the platelets in the perpendicular direction, causing the lattice field to reduce in this direction. This compressive strain causes reduction in the bandgap by pushing the valence band up and pulling the conduction band down. This means that,

there would be notches in the valence and conduction band-edges at the interface of the platelets, creating a quantum well, where electrons and holes would be trapped, facilitating their radiative recombination. This reduction in the bandgap causes the emission at higher (sub-bandgap) wavelengths. A schematic for this model is given in Figure 1.9(b).

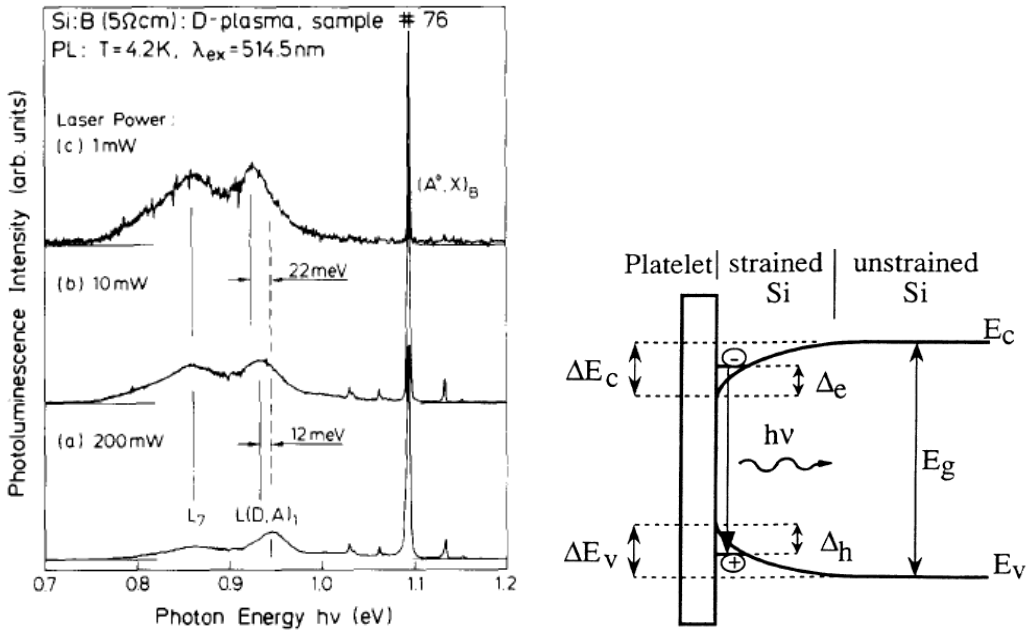

Figure 1.9: (a) Broad sub-bandgap PL bands formed by hydrogen plasma treatment of Cz-Si [46][8]. The peak at 1.1 eV is the band-edge emission. (b) A model explaining the origin of broad PL bands. A strain field around the platelets introduced by plasma treatment causes confinement of the carriers, facilitating their radiative recombination [53].

Many possibilities for the broadness of the PL bands have been reported in this model. It is known from the literature [59] by the studies of electronic levels that the localized levels are usually broadened. Furthermore, there are platelets of many different sizes, having different values of strain field, giving rise to emission at different wavelengths. The overlap of emission from different types of defects formed by hydrogen plasma treatment can also be responsible for the broadness of the PL bands. Hydrogen plasma also passivates the non-radiative defect sites. This makes the recombination of carriers at the platelets efficient, as other channels of recombination are blocked. Two main PL bands centered at 0.85 eV and 0.95 eV as shown in Figure

1.9(a) have been related to the recombination of the carriers at the potential wells surrounding the platelets in the (111) and (100) directions, respectively [53].

A different model has been reported in [60], where three possible mechanisms of carrier recombination has been proposed at the midgap states created by point defects introduced by the plasma treatment or ion implantation. Since the wavelength of the emission band is sub-bandgap, the emission can be due to recombination of carriers at the midgap states created due to incorporation of defects. There can be the following three mechanisms of recombination of carriers at the defect states, which are shown graphically in Figure 1.10.

(i) Recombination of trapped hole and free electron

(ii) Recombination of trapped electron and free hole

(iii) Recombination of trapped hole and trapped electron

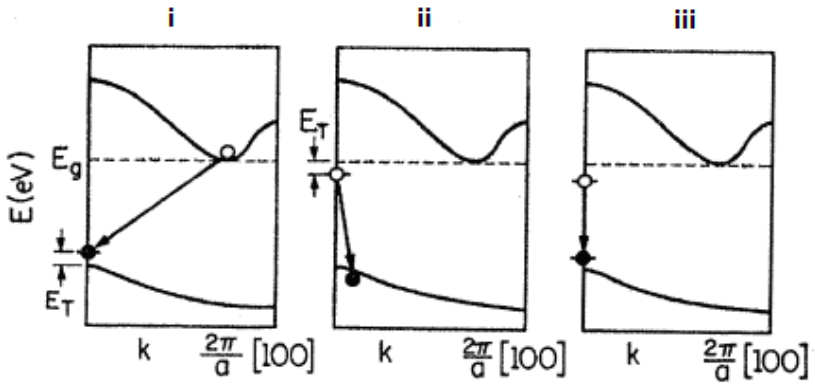

Figure 1.10: Three different mechanisms of carrier recombination at defect states in silicon. i) Recombination of free electron-trapped hole, ii) Recombination of free hole-trapped electron, iii) Recombination of trapped hole and trapped electron. Picture taken from [60].

For the recombination of carriers, their wavefunctions must overlap. The wavefunction of the trapped carrier can be expressed by an expansion in Bloch functions corresponding to different crystal momenta, as given below [60].

$$\psi_t(\vec{r}) = \Sigma g_k u(\vec{k}, \vec{r}) e^{i\vec{k}.\vec{r}} \qquad \text{Equation 1.1}$$

In this equation, $\vec{r}$ is the position vector of the carriers, which can be either free or trapped, $\vec{k}$ is the crystal momentum corresponding to the energy state of the free carrier

in the band, which is nearest the ground state energy level of the trapped carrier, $u(\vec{k},\vec{r})$ is the central cell function or in other words a periodic function of the lattice and g_k are weighting coefficients, which depend on the values of $\vec{k}$.

In the mechanism (i) where there is a free electron in the conduction band and a trapped hole in the defect state, the transition can be either direct or indirect, depending on whether there are deep or shallow defects. If there are shallow defects, then the defect state will be close to the valence band and the carrier will be trapped close to the valence band maximum. In this case, there is high probability of an indirect transition, so the emission efficiency would be low. The direct transition can be possible in the case where there are deep defects. For deep defects, there will be more values of $\vec{k}$ but the values of $\vec{k}$ at the conduction band minimum would still be low. This would still keep the probability of direct transition low. According to one estimate [61,62] the direct transition can be possible for deep defects if the defect state is located at 1/10 of the bandgap energy.

The mechanism (ii) involves the recombination of a free hole in the valence band and a trapped electron in the defect state, which is close to the conduction band. The wavefunction of the trapped electron will still be represented by Equation 1.1 but in this case there will be large number of $\vec{k}$ -values including the $\vec{k}$ -values at the valence band maximum. This extension in the $\vec{k}$ -space will provide the required momentum conservation. The recombination will then be direct and not require the assistance of a phonon, so the efficiency will be higher but there would be thermal broadening.

In mechanism (iii) both electrons and holes are trapped in the same defect state. Their wavefunction will be represented by Equation 1.1, which would contain same $\vec{k}$ -value terms for both electron and holes. Thus momentum conservation will be established and the recombination will be direct without the involvement of phonon. Furthermore, there will be no thermal broadening of the emission line.

There has been lot of debate and conflicting reports on the mechanism of the carrier recombination and the exact role played by hydrogen; yet it is well established that the hydrogen can induce defects in silicon that creates broad sub-bandgap PL bands. These broad PL bands can be utilized to develop a silicon based light source.

1.4 Comparison

A comparison of different approaches explained in this chapter is given in the Table 1.1.

Table 1.1: Comparison of different techniques used to enhance silicon emission.

Approach/Device	**Mechanism**	**Operating wavelength**	**Operating temperature**	**Pumping**	**Feature**	**Shortcoming**
Raman laser [4]	Stimulated Raman scattering	1600 nm, tunable	Room temperature	Optical	Lasing	Optical pumping, large size
Si nanocrystals [19, 20]	Quantum confinement	Visible	Room temperature	Optical, electrical	Gain	Not sub-bandgap emission
Quantum well [63]	Quantum confinement	Band-edge	Room temperature	Electrical	Stimulated emission	Band-edge emission, large size
Erbium doping [10]	Erbium ion doping/quantum confinement	1540 nm	Low temperature/room temperature	Optical, electrical		Very low emission/ broad area device
Dislocation loops [36]	Impurity (boron) doping/ modification of silicon band structure/ carrier confinement	Band-edge	Room temperature	Electrical		Band-edge emission, broad area device
W-line [38]	Si implantation/ carrier confinement	1218 nm	Low temperature	Electrical		Low temperature operation
G-line, A-centres [37]	Carbon implantation/ carrier confinement	1280 nm	Low temperature	Optical	Gain, stimulated emission	Optical pumping, low temperature operation
H defects [46, 54]	Hydrogen plasma treatment or ion implantation, quantum confinement/creation of midgap defect states/carrier confinement	Broadband 1300 nm 1500 nm	Low temperature reported in literature so far	Optical reported in literature so far		Optical pumping, low temperature operation
Requirements	Suitable approach but should have small (nano) size	1500 nm plus tunable	Room temperature	Electrical	Stimulated emission, gain, lasing	

An approach to introduce hydrogen related defects into silicon is interesting due to two reasons. First, it gives rise to sub-bandgap PL bands centered around 1300 and 1500 nm range, and thus covers the whole telecommunication window. Secondly, this approach has not been investigated from the point of view of emission enhancement. An investigation of the nature of defects, the emission mechanism, possibility of increasing emission further by material processing and pushing the operation towards room temperature could be worth exploring.

1.5 Approach in the present project

The approach taken in my PhD project is to enhance the silicon emission by the combination of material processing and device engineering. First, the light emission from silicon material will be enhanced by taking three different routes. These are: a) incorporation of hydrogen defects, b) carbon implantation and c) erbium doping. The enhanced emission from silicon material will then be further enhanced via the Purcell effect [64]. Although many techniques have been used to enhance the Si emission in the past, only one report on enhancing the silicon emission via the Purcell effect has been published [65]. In this reference, the silicon band-edge emission was enhanced by utilizing the Purcell effect. The present project is focused on enhancing the sub-bandgap emission.

1.5.1 Purcell effect

The Purcell effect was first reported by E.M Purcell in 1946 for RF frequencies [64], but the theory can be extended to the entire electromagnetic spectrum. The Purcell effect is based on Fermi's Golden Rule, which states that the probability of a radiative transition depends on the matrix element (essentially the Hamiltonian of the system) and the density of states in the receiving state. Therefore, the emission from an emitter is dependent on its environment and its emission can be controlled or modified by changing the environment accordingly. This control can be achieved by enclosing the emitter in a cavity to suppress or enhance the spontaneous emission by changing the local density of states. If there is a spectral (on-resonance) and spatial overlap of the emitter with the cavity mode, the spontaneous emission is enhanced. The factor by which this spontaneous emission is enhanced is called the Purcell factor. The Purcell

factor for a single emitter having a dipole moment '$\vec{d}$' is given by the following equation [66, 67]:

$$F_p = \frac{3Q_{\text{eff}}\left(\frac{\lambda_c}{n}\right)^3}{4\pi^2 V} \cdot \left|\frac{\vec{d}.\vec{f}(\vec{r}_e)}{\vec{d}}\right|^2 \cdot \frac{\Delta\omega_c^{\,2}}{4(\omega_e-\omega_c)^2+\Delta\omega_c^{\,2}}$$

Equation 1.2

Here, Q_{eff} is the effective quality factor. It takes into account the quality factor of the cavity Q_c and the finite linewidth of the emitter Q_e [67]. It can be expressed as $1/Q_{eff} = 1/Q_c + 1/Q_e$. V is the mode volume of the cavity. The second and third term give the degree of spatial and spectral overlap of the emitter with the cavity mode, respectively. Ideally, the second and third terms should be equal to unity to achieve a high Purcell factor, but in reality, it is difficult to achieve perfect spatial and spectral overlap and thus they have values smaller than unity. Assuming these terms to be unity, however, the Purcell factor can be expressed more simply via the following equation [64]:

$$F_p = \frac{3Q_{\text{eff}}\left(\frac{\lambda_c}{n}\right)^3}{4\pi^2 V}$$

Equation 1.3

From this equation, it is concluded that in order to have a high enhancement of the emission from the emitter, the emitter should be coupled to a cavity with a high Q-factor and a low mode volume. Photonic crystal cavities are suitable candidates for this purpose as they have very low mode volume (of the order of cubic wavelength) and very high Q-factors (100k) [68]. I present a brief discussion on photonic crystal, photonic crystal cavity and the control of spontaneous emission by photonic crystal in the next sections.

1.5.2 Photonic crystal

Photonic crystals are periodic dielectric wavelength-scale structures. They consist of alternative low and high refractive index regions in one, two or three dimensions, as shown in Figure 1.11. Similarly as the periodic potential in semiconductor crystals affects the motion of electrons, the photonic crystal affects the motion of photons by forbidding some range of wavelengths, while allowing others to pass. The wavelengths that are allowed to pass are called Bloch modes that form bands in the dispersion

diagram. The band of wavelengths where there is no allowed propagation is called the bandgap.

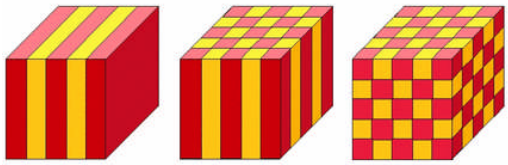

Figure 1.11: One, two and three dimensional photonic crystals. The red and yellow colours indicate different refractive index regions [69].

1.5.3 Spontaneous emission control by 2D photonic crystals

To make an efficient light source, it is necessary to have control over the spontaneous emission. The spontaneous emission that is not extracted out of the light emitting diode, or which is not coupled to the lasing modes in the case of a laser acts as a noise and is detrimental to the performance of the light source. To increase the performance of the light source, the undesired spontaneous emission should be suppressed. On the other hand, the efficiency of the light emitting diode can be increased by enhancing the extracted spontaneous emission. Both of these, i.e., inhibition and enhancement of spontaneous emission can be achieved by using a photonic crystal. The spontaneous emission in a PhC is controlled by the combination of the in-plane bandgap and the out-of-plane total internal reflection. Due to the in-plane bandgap, certain wavelengths are not allowed to pass, reducing the in-plane spontaneous emission. This blocked energy is redistributed in the vertical direction [70]. Time resolved photoluminescence shows the increase of lifetime when the emission wavelengths are in the bandgap of PhC compared to their lifetime in a system where there is no bandgap. Since the emission lifetime and spontaneous emission have inverse relation, the in-plane spontaneous emission rate decreases.

1.5.4 Emission enhancement by photonic crystal cavity

The spontaneous emission can be enhanced by creating a cavity in the PhC. This is done by designing a mode within the light line. The mode is confined by the total internal reflection in the vertical direction and by the photonic bandgap effect in-plane.

When the emission is on resonance with the cavity mode, it is enhanced by the Purcell effect, explained in Section 1.5.1. In other words, when the k-vectors of the emission dipole matches with the k-vector of the cavity mode, they are coupled resonantly and the emission enhances, scaling with Q/V of the cavity, according to Equation 1.2. Since high Q/V values are required to gain a maximum advantage of the Purcell effect, it is necessary to design a cavity with very high quality factors and low mode volume. One such cavity is an L3 cavity, where three holes are missing in the Γ-K direction to form a cavity. The holes adjacent to the cavity are displaced slightly to increase the Q-factor [68]. I have given more details on the design of this cavity in Chapter 2. Using this cavity design, Q-factors of 100,000 and mode volumes of the order of a cubic wavelength have been achieved in silicon, making it an attractive candidate for emission enhancement. The schematic design of this cavity is shown in Figure 1.12(a).

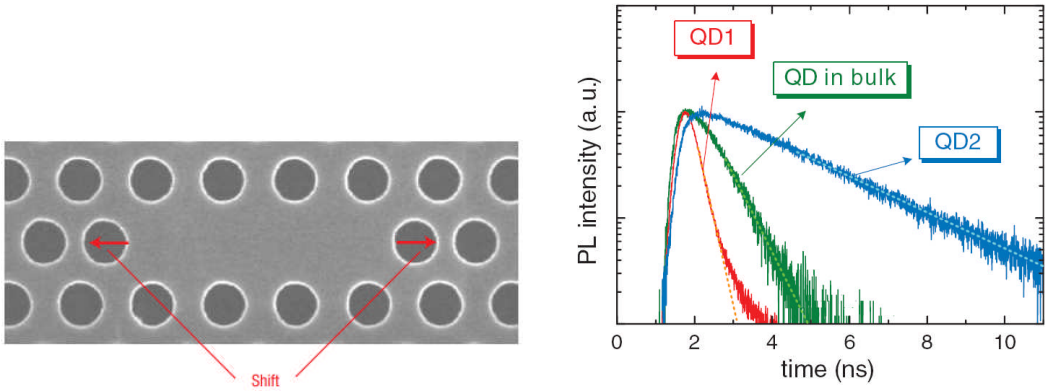

(a) (b)

Figure 1.12: (a) Scheme to achieve very high Q-values. The holes adjacent to cavity are shifted laterally [68]**.** (b) Increase of lifetime by the photonic bandgap effect (blue curve), and decrease by the Purcell effect (red curve) [71][10].

The Purcell factor, which quantifies the emission enhancement due to the Purcell effect, can be measured directly by time resolved PL measurements [72,73]. Figure 1.12(b) shows an example of a time resolved PL measurement of an L3 cavity with embedded quantum dots as the internal light source. It is clear from the figure that when the emission of the emitter is on resonance with the cavity, the carrier lifetime decreases compared to bulk, causing enhancement in the emission. In contrast, at off-resonant

condition, the lifetime increases compared to the bulk, resulting in the decrease of spontaneous emission rate.

The Purcell effect has been used successfully to increase the light emission in different systems, which also helps to reduce the lasing threshold [74,75].

1.6 Aims of the project

The aim of the project is to enhance silicon emission by using different routes of material processing to generate active light emitters, which is then further enhanced on resonance with a photonic crystal cavity.

The aims of the project are listed below.

1. The following routes for material processing to increase silicon light emission will be investigated:
   i. Incorporation of hydrogen related defects by plasma treatment and ion implantation.
   ii. Creating a narrow linewidth G-line by carbon implantation.
   iii. Using emission from erbium ions by doping in silicon or by depositing a layer of erbium compound on top of it.
2. Understanding the nature of the defects created by hydrogen plasma treatment and ion implantation.
3. Investigate the possibility of emission enhancement via the Purcell effect by coupling the emission achieved by the above three routes with a PhC nanocavity.
4. Demonstrate a practical Si light source with the following features:
   i. Room temperature operation
   ii. Electrical pumping
   iii. Small size
   iv. Sub-bandgap emission (preferably in telecommunication window, 1300-1600 nm)
   v. Tunability
   vi. Narrow emission line (laser like)
   vii. Output power that could be used for practical applications. Power level in the range of picowatts to nanowatts for sensing applications and at least microwatts are required for on-chip communications.

The final goal can be summarized in the following schematic picture (Fig. 1.13).

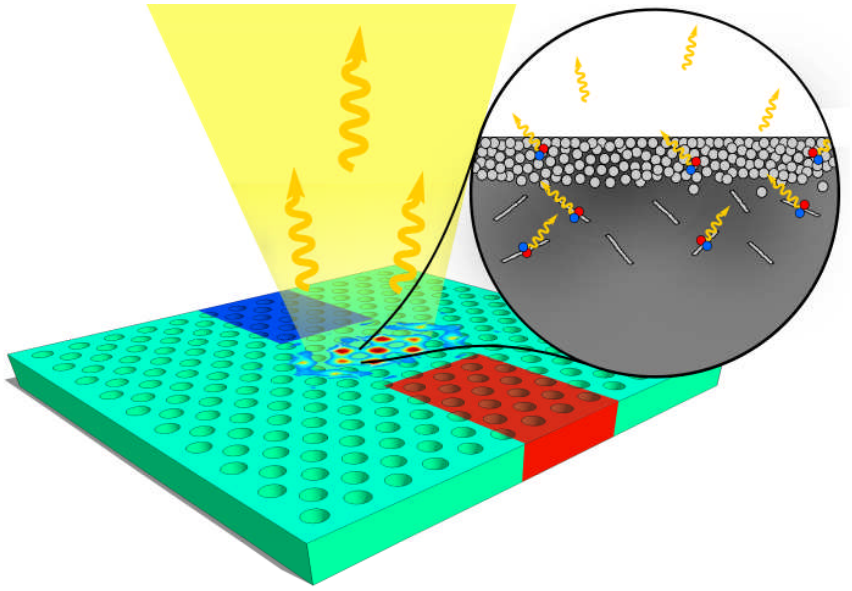

Figure 1.13: An all-silicon PhC nano LED. The emission from the Si material is enhanced by material processing (incorporation of defects) and device engineering (Purcell effect). A *pn* junction is implemented across the cavity; the red and blue pads indicate p and n doped regions. The zoomed-in bubble shows the defects in Si, where carriers (blue and red dots) are trapped and recombine radiatively to emit photons (yellow arrows). Art work: Courtesy of Dr Christopher Reardon, University of St Andrews.

1.7 Conclusions

Silicon is a poor emitter of light due to its indirect bandgap and hence cannot be used to make an efficient light source. Different approaches have been used in the past to enhance the silicon emission. Most notable among these are using stimulated Raman scattering to demonstrate silicon Raman laser, doping of erbium and quantum confinement of carriers. All these approaches are a step forward in the development of a silicon light source but unfortunately they do not combine all the desired features. These features are listed as: electrical pumping, room temperature operation, small size, sub-bandgap emission (preferably in telecommunication window, 1300-1600 nm), narrow

emission line (laser like), tunability and spectral purity. Raman laser lacks electrical pumping and has a large footprint, emission levels of erbium doped silicon light sources are very low due to low solubility of erbium in silicon and reduction of emission at higher temperatures, silicon nanocrystals has broad emission in the visible range, while narrow emission lines due to impurities in silicon like G-line, C-line and W-lines work only at low temperatures. Thus, although all these techniques show some promise, the requirement of electrically pumped sub-bandgap silicon nanolight source that operates at room temperature still remains. After evaluating different schemes of enhancing silicon emission, I conclude that incorporation of hydrogen defects in the silicon lattice, which creates sub-bandgap PL bands, is worth further investigation as this approach has not been investigated in detail from the point of view of emission enhancement. There is a possibility to enhance the emission from silicon material by incorporation of hydrogen defects. Furthermore, the possibility of enhancing sub-bandgap silicon emission via Purcell effect has not been investigated before, which will be the subject of research in this thesis. In addition to using luminescence bands created by hydrogen related defects in silicon, I will also investigate the possibility of enhancing erbium and G-line emission by the Purcell effect.

References

[1] L. Pavesi, “Routes towards silicon based lasers,” Materials today 8, 18–25 (2005).

[1]Reprinted with permission. Copyright (2005) Elsevier.

[2] O. Boyraz, and B. Jalali, “Demonstration of a silicon Raman laser,” Opt. Express 12, 5269-5273 (2004).

[3] H. Rong, A. Liu, R. Jones, O. Cohen, D. Hak, R. Nicolaescu, A. Fang, and Mario Paniccia, “An all-silicon Raman laser,” Nature 433, 292-294 (2005).

[4] H. Rong, R. Jones, A. Liu, O. Cohen, D. Hak, and A. Fang, “A continuous-wave Raman silicon laser,” Nature 433, 725-728 (2005).

[2]Reprinted by permission from Macmillan Publishers Ltd: [Nature] (doi:10.1038/nature03346), copyright (2005).

[5] H. Rong, S. Xu, Ying-Hao Kuo, V. Sih, O. Cohen, O. Raday, and M. Paniccia, “Low- threshold continuous- wave Raman silicon laser,” Nat. Photonics 1, 232 - 237 (2007).

[6] H. Rong, A. Liu, R. Nicolaescu, M. Paniccia, O. Cohen, and D. Hak, “Raman gain and nonlinear optical absorption measurement in a low loss silicon waveguide,” Appl. Phys. Lett. 85, 2196–2198 (2004).

[7] H. Efeoglu, J. H Evans, T. E Jackman, B. Hamilton, D. C Houghton, J. M Langer, A. R. Peaker, D. Perovic, I. Poole, N. Ravel, P. Hemment, and C. W. Chan, “Recombination processes in erbium-doped MBE silicon,” Semicond. Sci. Technol. 8, 236 (1993).

[8] J. Michel, J. L. Benton, R. F. Ferrante, D. C. Jacobson, D. J. Eaglesham, E. A. Fitzgerald, Y.-H. Xie, J. M. Poate, and L. C. Kimerling , “Impurity enhancement of the 1.54 micron Er^{3+} luminescence in silicon,” J. Appl. Phys. 70, 2672 (1991).

[9] S. Coffa, G. Franzò, F. Priolo, A. Polman, and R. Serna, “Temperature dependence and quenching processes of the intra-4f luminescence of Er in crystalline Si,” Phys. Rev. B 49, 16313 (1994).

[10] G. Franzò, S. Coffa, F. Priolo, and C. Spinella, “Mechanism and performance of forward and reverse bias electroluminescence at 1.54 μm from Er-doped Si diodes,” J. Appl. Phys. 81, 2784 (1997).

[3]Reprinted with permission. Copyright [1997], American Institute of Physics.

[11] H. Ennen, J. Schneider, G. Pomrenke, and A. Axmann, "1.54-μm luminescence of erbium implanted III-V semiconductors and silicon", Appl. Phys. Lett. 43, 943 (1983).

[12] A. J. Kenyon, "Erbium in silicon," Semicond. Sci. Tech . 20, R65 - R84 (2005).

[13] F. Priolo, G. Franzò, S. Coffa, and A. Carnera, "Excitation and nonradiative deexcitation processes of Er^{3+} in crystalline Si," Phys. Rev. B 57, 4443 (1998).

[14] M. Fujii, M. Yoshida, Y. Kanzawa, S. Hayashi, and K. Yamamoto, "1.54 μm photoluminescence of Er^{3+} doped into SiO_2 films containing Si nanocrystals: Evidence for energy transfer from Si nanocrystals to Er^{3+}," Appl. Phys. Lett. 71, 1198 (1997).

[15] A. Polman, "Erbium implanted thin film photonic materials," J. Appl. Phys. 82, 1 (1997).

[16] D. J. Eaglesham, J. Michel, E. A. Fitzgerald, D. C. Jacobson, J. M. Poate, J. L. Benton, A. Polman, Y.-H. Xie, and L. C. Kimerling, "Microstructure of erbium‐implanted Si," Appl. Phys. Lett. 58, 2797 (1993).

[17] J. D. Carey, R. C. Barklie, J. F. Donegan, F. Priolo, G. Franzò, and S. Coffa, "An EPR study of Er-impurity Complexes in Si," J. Lumin. 80, 297 (1998).

[18] F. Priolo, G. Franzò, S. Coffa, A. Polman, S. Libertino, R. Barklie, and D. Carey, "The erbium‐impurity interaction and its effects on the 1.54 μm luminescence of Er^{3+} in crystalline silicon," J. Appl. Phys. 78, 3874 (1995).

[19] L. Pavesi, L. D. Negro, C. Mazzoleni, G. Franzò, and F. Priolo, "Optical gain in silicon nanocrystals," Nature 408, 440 (2000).

[20] A. Marconi, A. Anopchenko, M. Wang, G. Pucker, P. Bellutti, and L. Pavesi, "High power efficiency in Si-nc/SiO_2 multilayer light emitting devices by bipolar direct tunneling," Appl. Phys. Lett. 94, 221110 (2009).

[21] J. Valenta, R. Juhasz, and J. Linnros, "Photoluminescence spectroscopy of single silicon quantum dots," Appl. Phys. Lett. 80, 1070 (2002).

[22] M. Zacharias, J. Heitmann, R. Scholz, U. Kahler, M. Schmidt, and J. Bläsing, "Size-controlled highly luminescent silicon nanocrystals: A SiO/SiO_2 superlattice approach," Appl. Phys. Lett. 80, 661 (2002).

[23] J. Heitmann, F. Müller, L. Yi, and M. Zacharias, "Excitons in Si nanocrystals: Confinement and migration effects," Phys. Rev. B 69, 195309 (2004).

[24] L. Khriachtchev, M. Räsänen, S. Novikov, O. Kilpelä, and J. Sinkkonen, "Raman scattering from very thin Si layers of Si/SiO_2 superlattices: Experimental evidence of

structural modification in the 0.8–3.5 nm thickness region," J. Appl. Phys. 86, 5601 (1999).

[25] Y. J. Chabal, K. Raghavachari, X. Zhang, and E. Garfunkel, "Silanone (Si=O) on Si (100): intermediate for initial silicon oxidation," Phys. Rev. B 66, 161315(R) (2002).

[26] P. M. Fauchet, "Light emission from silicon quantum dots," Materials today 8, 18–25 (2005).

[27] L. Dal Negro, M. Cazzanelli, L. Pavesi, S. Ossicini, D. Pacifici, G. Franzò, F. Priolo, and F. Iacona, "Dynamics of stimulated emission in silicon nanocrystals," Appl. Phys. Lett. 82, 4636 (2003).

[28] L. Khriachtchev, M. Räsänen, S. Novikov, and J. Sinkkonen, "Optical gain in Si/SiO_2 lattice: Experimental evidence with nanosecond pulses," Appl. Phys. Lett. 79, 1249 (2001).

[29] K. Luterová, K. Dohnalová, V. Švrček, I. Pelant, J.-P. Likforman, O. Crégut, P. Gilliot, and B. Hönerlage, "Optical gain in porous silicon grains embedded in sol-gel derived SiO_2 matrix under femtosecond excitation," Appl. Phys. Lett. 84, 3280 (2004).

[30] K. Dohnalová, I. Pelant, P. Gilliot, O. Crégut, and B. Hönerlage, "Si nanocrystals in a distributed feedback laser cavity," Appl. Phys. Lett. 88, 251105 (2006).

[31] R. G. Elliman, M. J. Lederer, N. Smith, and B. Luther-Davies, "The fabrication and properties of silicon-nanocrystal-based devices and structures produced by ion implantation – The search for gain," Nucl. Instrum. Methods Phys. Res. B 206, 427 (2003).

[32] G. Franzò, S. Boninelli, D. Pacifici, F. Priolo, F. Iacona, and C. Bongiorno, "Sensitizing properties of amorphous Si clusters on the 1.54-μm luminescence of Er in Si-rich SiO_2," Appl. Phys. Lett. 82, 3871 (2003).

[33] Hak-Seung Han, Se-Young Seo, Jung H. Shin, and N. Park, "Coefficient determination related to optical gain in erbium-doped silicon-rich silicon oxide waveguide amplifier," Appl. Phys. Lett. 81, 3720 (2002).

[34] A. Shakoor, R. Lo Savio, S. L. Portalupi, D. Gerace, L. C. Andreani, M. Galli, T. F. Krauss, and L. O'Faolain, "Enhancement of room temperature sub-bandgap light emission from silicon photonic crystal nanocavity by Purcell effect," Phys. B 407, 4027–4031 (2012).

[4]

[35] N. A. Drozdov, A. A. Patrin, and V. D. Tkachev, “Recombination radiation on dislocations in silicon,” Pisma Zh. Eksp. Teor. Fiz. 23, 651-653, Sov. Phys. JETP Lett. 23, 597-599 (1976).

[36] Wai Lek Ng, M. A. Lourenço, R. M. Gwilliam, S. Ledain, G. Shao, and K. P. Homewood, “An efficient room-temperature silicon-based light-emitting diode,” Nature 410, 192–194 (2001).

[5]Reprinted by permission from Macmillan Publishers Ltd: [Nature] (doi:10.1038/35065571), copyright (2001).

[37] S. G. Cloutier, P. A. Kossyrev, and J. Xu, “Optical and stimulated emission in periodic nanopatterned crystalline silicon,” Nat. Materials 4, 887 (2005).

[7]Reprinted by permission from Macmillan Publishers Ltd: [Nature] (doi:10.1038/nmat1530), copyright (2005).

[38] J. Bao, M. Tabbal, T. Kim, S. Charnvanichborikarn, J. S. Williams, M. J. Aziz, and F. Capasso, “Point defect engineered Si sub-bandgap light-emitting diode,” Opt. Express 15, 6727-6733 (2007).

[39] D. Leong, M. Harry, K. J. Reeson, and K. P. Homewood, “A silicon/iron-di-silicide light-emitting diode operating at a wavelength of 1.5μm,” Nature 387, 686-688 (1997).

[40] N-T. Satoko, T. Michio, H. Kazuyuki, O. Takeshi, and I. Hisayoshi, “Characterization of light element impurities in ultrathin silicon-on-insulator layers by luminescence activation using electron irradiation,” Jpn. J. Appl. Phys. 48, 031201 (2009).

[6]Reprinted with permission. Copyright [2009], Japan Society of Applied Physics.

[41] J. L. Benton, J. Michel, L. C. Kimerling, R. A. Gottscho, and B. E. Weir, “Carbon reactions in reactive ion etched silicon,” J. Electron. Mater. 20, 643-647 (1991).

[42] C. H. Henry, “Theory of linewidth of semiconductor lasers,” IEEE J. Quantum Electron. 18, 259–264 (1982).

[43] I. Martín, M. Vetter, A. Orpella, C. Voz, J. Puigdollers, R. Alcubilla, A. V. Kharchenko, and P. Roca i Cabarrocas, “Improvement of crystalline silicon surface passivation by hydrogen plasma treatment,” Appl. Phys. Lett. 84, 1474 (2004).

[44] A. Henry, O. O. Awadelkarim, J. L. Lindström, and G. S. Oehrlein, “Effects of deuterium plasma treatments on the electrical properties of boron-doped silicon,” Mater. Sci. Eng: B 4, 147-151 (1989).

[45] M. Singh, J. Weber, and M. Konuma, “Evidence for intrinsic point defect generation during hydrogen-plasma treatment of silicon,” Physica B 170, 218–222 (1991).

[46] J. Weber, “Defect generation during plasma treatment of semiconductors,” Physica B 170, 201-217 (1991).

[8]Reprinted with permission. Copyright (1991) Elsevier.

[47] N. Johnsonn, F. A. Ponce, R. Street, and R. Nemanich, “Defects in single-crystal silicon induced by hydrogenation,” Phys. Rev. B 35, 4166-4169 (1987).

[48] G. Davies, “The optical properties of luminescence centres in silicon,” Phys. Rep. 176, 83 (1989).

[49] G. S. Oehrlein, “Dry etching damage of silicon: A review,” Mater. Sci. Eng: B 4, 441-450 (1989).

[50] M. Gao, and X. F. Duan, “A transmission electron microscopy study of micro-structural defects in proton implanted silicon,” J. Appl. Phys. 80, 4767-4769 (1996).

[51] K.-H. Hwang, J.-W. Park, E. Yoon, K.-W. Whang, and J. Y. Lee, “Amorphous {100} platelet formation in (100) Si induced by hydrogen plasma treatment,” J. Appl. Phys. 81, 74 (1997).

[52] S. J. Jeng, G. S. Oehrlein, and G. J. Scilla, “Hydrogen plasma induced defects in silicon,” Appl. Phys. Lett. 53, 1735 (1988).

[53] H. Weman, B. Monemar, G. S. Oehrlein, and S. J. Jeng, “Strain-induced quantum confinement of carriers due to extended defects in silicon,” Phys. Rev. B 42, 3109-3113 (1990).

[54] A. Henry, B. Monemar, J. Lindstrom, T. D. Bestwick, and G. S. Oehrlein, “Photoluminescence characterization of plasma exposed silicon surfaces,” J. Appl. Phys. 70, 5597-5603 (1991).

[55] H. Weman, J. L. Lindström, G. S. Oehrlein, and B. G. Svensson, “Reactive-ion- and plasma-etching-induced extended defects in silicon studied with photoluminescence,” J. Appl. Phys. 67, 1013 (1990).

[56] L. T. Canham, M. R. Dyball, W. Y. Leong, M. R. Houlton, A. G. Cullis, and P. Smith, “Radiative recombination channels due to hydrogen in crystalline silicon,” Mater. Sci. Eng: B 4, 41-45 (1989).

[57] W. Düngen, R. Job, Y. Ma, Y. L. Huang, T. Mueller, W. R. Fahrner, L. O. Keller, J. T. Horstmann, and H. Fiedler, "Thermal evolution of hydrogen related defects in hydrogen implanted Czochralski silicon investigated by Raman spectroscopy and atomic force microscopy," J. Appl. Phys. 100, 034911 (2006).

[58] M. O. Watanabe, M. Taguchi, K. Kanzaki, and Y. Zohta, "DLTS Study of RIE-Induced Deep Levels in Si Using p + n Diode Arrays," Jpn, J. Appl. Phys. 22, 281-286 (1983).

[59] I. Kukushkin, V. Timofeev, K. V Klitzing, and K. Ploog, in Festkorperprobleme (Advances in Solid State Physics), edited by P. Grosse (Pergamon/Vieweg, Braunschweig, FRG), vol. 28, p. 21 (1988).

[60] R. J. Spry, W. D. Compton, "Recombination luminescence in irradiated silicon," Phys. Rev. 175, 3 (1968).

[61] Ya. E. Pokrovskii, K.I Svistunova, Soviet Phys-Solid state 6, 13 (1964).

[62] Ya.E. Pokrovskii, "In radiative recombination in semiconductors," edited by C.B Guillaume (Dunod Cie., Paris), pp.129-136 (1964).

[63] S. Saito, Y. Suwa, H. Arimoto, N. Sakuma, D. Hisamoto, H. Uchiyama, J. Yamamoto, T. Sakamizu, T. Mine, S. Kimura, T. Sugawara, and M. Aoki, "Stimulated emission of near-infrared radiation by current injection into silicon (100) quantum well," Appl. Phys. Lett. 95, 241101 (2009).

[64] E. M. Purcell, "Spontaneous emission probabilities at radio frequencies," Phys. Rev. 69, 681 (1946).

[65] S. Iwamoto, and Y. Arakawa, "Observation of enhanced photoluminescence from silicon photonic crystal nanocavity at room temperature," Appl. Phys. Lett. 91, 211104 (2007).

[66] J.-M. Lourtioz, H. Benisty, V. Berger, "Photonic crystals: towards nanoscale photonic devices," Springer-Verlag , 2008-06 , ISBN: 3540783466.

[67] J.-M. Gérard, "Solid-state cavity-quantum electrodynamics with self-assembled quantum dots," Top. Appl. Phys. 90, 269 (2003).

[68] T. Akahane, T. Asano, B.-S. Song, and S. Noda, "High-Q photonic nanocavity in a two-dimensional photonic crystal," Nature 425, 944 (2003).

[9]Reprinted by permission from Macmillan Publishers Ltd: [Nature] (doi:10.1038/nature02063), copyright (2003).

[69] J. D. Joannopoulos, S. G. Johnson, J. N. Winn, and R. D. Meade, “Photonic crystals: molding the flow of light.” Princeton University Press; 2nd revised edition, ISBN-10: 0691124566, Feb (2008).

[70] M. Fujita, S. Takahashi, Y. Tanaka, T. Asano, and S. Noda, “Simultaneous inhibition and redistribution of spontaneous light emission in photonic crystals,” Science 308, 5726, 1296-1298 (2005).

[71] Wen-Hao Chang, Wen-Yen Chen, Hsiang-Szu Chang, Tung-Po Hsieh, Jen-Inn Chyi, and Tzu-Min Hsu, “Efficient single-photon sources based on low-density quantum dots in photonic crystal nanocavities,” Phys. Rev. Lett. 96, 117401 (2006).

[10]Reprinted with permission. Copyright [2009], American Physical Society.

[72] D. Englund, D. Fattal, E. Waks, G. Solomon, B. Zhang, T. Nakaoka, Y. Arakawa, Y. Yamamoto, and J. Vučković, “Controlling the spontaneous emission rate of single quantum dots in a two dimensional photonic crystal,” Phys. Rev. Lett. 95, 013904 (2005).

[73] A. Kress, F. Hofbauer, N. Reinelt, M. Kaniber, H. J. Krenner, R. Meyer, G. Böhm, and J. J. Finley, “Manipulation of the spontaneous emission dynamics of quantum dots in two dimensional photonic crystals,” Phys. Rev. B 71, 241304 (2005).

[74] S. Strauf, K. Hennessy, M. T. Rakher, Y.-S. Choi, A. Badolato, L. C. Andreani, E. L. Hu, P. M. Petroff, and D. Bouwmeester, “Self-tuned quantum dot gain in photonic crystal lasers,” Phys. Rev. Lett. 96, 127404 (2006).

[75] M. Nomura, S. Iwamoto, K. Watanabe, N. Kumagai, Y. Nakata, S. Ishida, and Y. Arakawa, “Room temperature continuous-wave lasing in photonic crystal nanocavity,” Opt. Express 14, 6308–6315 (2006).

Chapter 2

Design, fabrication and characterization of photonic crystal cavities

In Chapter 1, I discussed the enhancement of light emission by coupling it with a cavity on resonance. I also discussed using photonic crystal (PhC) cavities for this purpose in Section 1.5.4, with a brief overview of the L3 PhC cavity, which combines a high Q-factor with a small mode volume. In this chapter, I provide details of the design, fabrication and characterization methods of the PhC cavities.

2.1 Design

Many different designs of PhC cavities have been reported in the literature. Some of the most common designs include heterostructure PhC cavities [1], H0 and H1 cavities [2,3], dispersion adjusted cavities [4] and Ln cavities [5]. In Ln cavities, some holes in the PhC are removed in the Γ-K direction to form a cavity, where n stands for the number of holes removed. The most common Ln cavities are L3, L5 and L7, with 3, 5 and 7 missing holes respectively. A schematic of these triangular lattice Ln cavities is given in Figure 2.1.

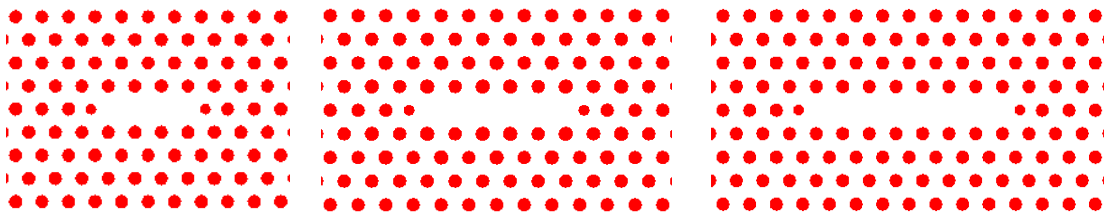

Figure 2.1: Schematic of L3, L5 and L7 cavities.

The resonance wavelength of these cavities can be controlled by adjusting the lattice period, a, and the fill factor r/a, where r is the radius of the PhC holes. The commercial software RSOFT, based on 2D finite difference time domain (FDTD) was used to support the design of the PhC cavities and to verify the resonance wavelength,

determine the ideal Q-factors and the mode profile. The mode profile of the L3 cavity is given below (Fig. 2.2).

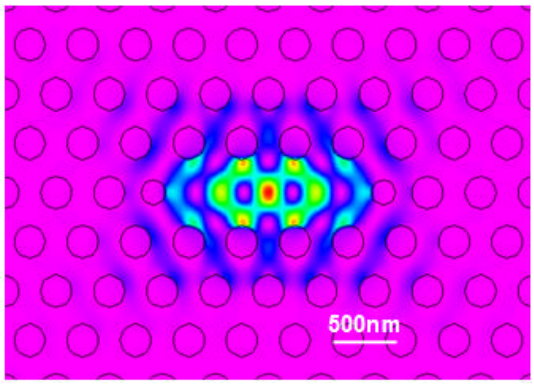

Figure 2.2: Mode profile $|E|^2$ of an L3 PhC cavity, calculated by FDTD using commercial software RSOFT.

The aim is to build Ln PhC cavities that have their fundamental resonance at wavelengths in the 1300-1600 nm range, which is achieved by tuning the lattice period and r/a values. A map of the corresponding design parameters for operation in the 1300 nm and 1500 nm windows is shown in Figures 2.3(a) and 2.3(b) and (c), respectively.

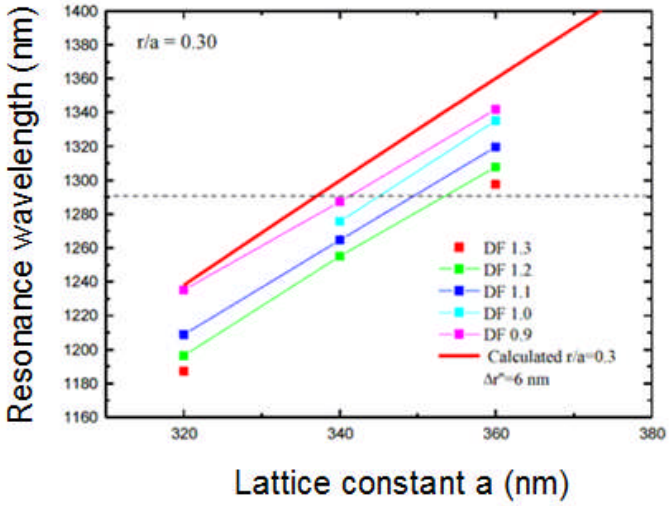

Figure 2.3: (a) Calculated and experimentally measured resonance wavelengths for different lattice periods of L3 cavity with fill factor of 0.3 at 12K. The target wavelength is 1280 nm. The "DF" stands for the dose factor of the electron beam used for the fabrication (explained in Section 2.2). Higher DF corresponds to PhC with larger hole diameters.

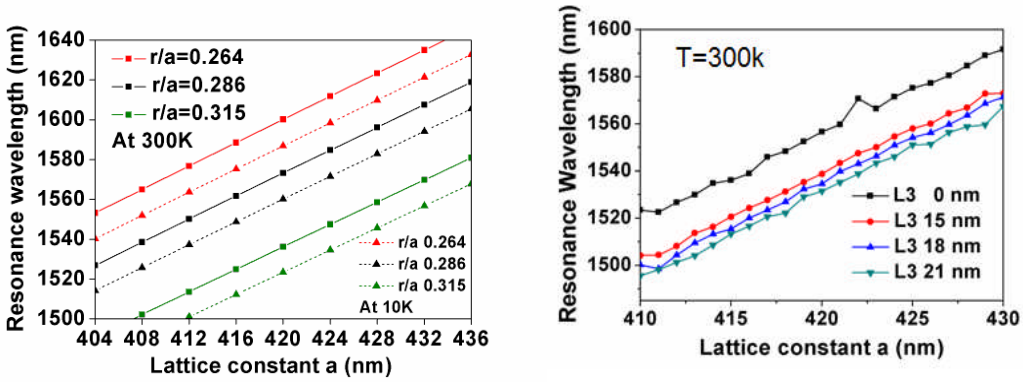

(b) (c)

Figure 2.3: (b) Theoretical and measured (c) resonance wavelengths for different lattice periods and fill factors to target resonance wavelength around 1500 nm. In (c), 0-21 nm stands for the far-field optimization parameter (explained in the following paragraph).

For example, a period of 420 nm with an r/a value of 0.28 gives the fundamental mode at 1550 nm in the experiment. A period of 360 nm with an r/a value of 0.3 gives a fundamental mode resonance at 1300 nm. There is a slight difference in the designed and experimentally measured parameters, as after the fabrication, the hole diameters can be offset from the target value by 10-20 nm. A few nm variations in the thickness of the top silicon layer of SOI can also change the resonance wavelengths and Q-factors of the cavity dramatically. The 3σ variation of the thickness reported by the manufacturer of SOI is 20 nm but the chances of errors cannot be ruled out. In addition to this, there can also be a possibility of an error factor in the model as well. Overall, the difference between the theoretical and experimentally measured values is around 10 nm, which was pre-adjusted during the fabrication to hit the target resonance wavelengths. The fabrication results were consistent among different samples.

In order to achieve high Q-factors, small modifications were introduced in the cavity design. These modifications include reducing the diameter of the holes adjacent to the cavity and slightly shifting those outwards, following [5,6]. Due to the shifting of the holes, the field is confined more gently at the cavity mirrors, instead of a sudden termination. This phenomenon is called gentle confinement and helps to increase the Q-factor of the PhC cavity. The increase of Q-factors by gentle confinement mechanism can be understood by expressing the electric field profile inside the cavity as a product

of fundamental sinusoidal wave and the envelope function, which is determined by the cavity design. In Fourier domain, the field profile would then be obtained by convolution of the fundamental sinusoidal wave and the envelope function. The Fourier transform of the sinusoidal wave gives delta functions at $k = \pm 2\pi / \lambda$, while the shape of the overall function would be controlled by the envelope function. Considering the case of the unmodified L3 PhC cavity, shown in Figure 2.4(a), there would be a sudden termination of the field at the edges of the cavity. Hence, the envelope function can be considered as a square wave in real space, which gives the sinc function in the Fourier domain, as shown in Figure 2.4(b,c).

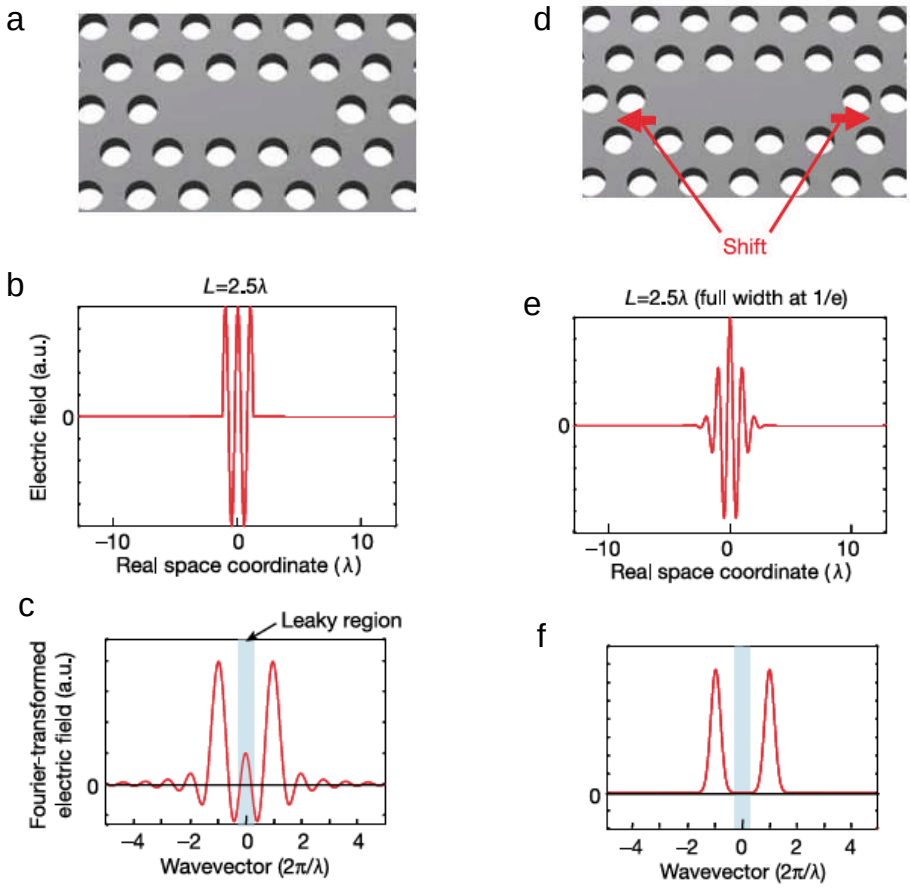

Figure 2.4 Basic design of an L3 PhC cavity (a) with its electric field in the real space coordinates (b) and Fourier domain (c). The modified L3 PhC cavity (d) with Gaussian electric field profile (e) and its Fourier transform (f). Reproduced from [5][1].

The convolution of this envelope function with the delta functions of the fundamental sinusoidal wave will bring some of the high spatial frequency components within the leaky region, as indicated in Figure 3.4(c) by blue shaded region. Thus, the losses would increase, which decreases the Q-factors. This analysis shows that the envelope function at the edges of the cavity should not terminate sharply but gently to avoid high spatial frequency components coming within the leaky region. By moving two holes adjacent to the cavity outwards, the envelope function would have gentle spatial variation at the cavity edges. Hence, the envelope function can be considered as a Gaussian function, whose convolution with the delta functions in the Fourier domain would bring less high spatial frequency components within the leaky region as shown in Figure 2.4(d-f). Thus, the losses would reduce and Q-factors of the cavity would increase.

The electric field profiles of the fundamental mode of the unmodified and modified L3 PhC cavity are shown in Figures 2.5(a,c) with their corresponding Fourier transforms in Figures 2.5(b,d), respectively.

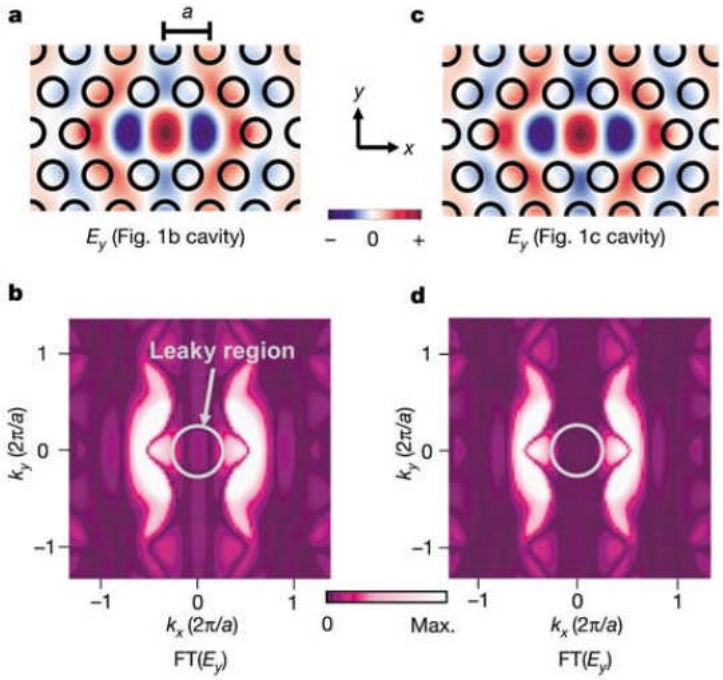

Figure 2.5: (a) The electric field profile (E_y) of the fundamental mode of L3 PhC cavity with its Fourier transform (b). The leaky region (white circle) contains some components of the field. The mode profile of modified L3 PhC cavity (c) and its Fourier transform (d). Due to lateral shift of two holes adjacent to the cavity, the losses are reduced and hence Q-factor is increased. Reproduced from [5][1].

The leaky region is shown by a white circle. By comparing the Fourier domain pictures of both cavity designs, it is clear that there are fewer components within the leaky region in the modified cavity.

In this project, the basic design of the L3 PhC cavity was changed by modifying the position and size of the holes adjacent to the cavity to obtain higher Q/V ratio. Following [5,6], the holes adjacent to the cavity were reduced by $\Delta r/a=0.06$ and the holes were shifted outwards by $\Delta x/a=0.15$, as this gives the highest Q/V value according to Figure 2.6.

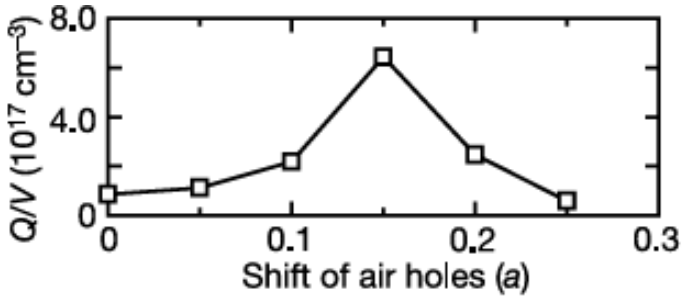

Figure 2.6: Q/V of the cavity for different lateral shifts of the holes adjacent to the cavity. The biggest Q/V value is obtained with a shift of 0.15a. Reproduced from [5][1].

In addition, a second modification was implemented to increase the amount of light emitted vertically. This modification is called far-field optimization [7,8]. Far-field optimization is carried out by increasing or decreasing some of the holes surrounding the PhC cavity by a small amount, which forms a second order grating. The second order grating has the effect of folding back some of the k-vectors lying outside the vertical light emission cone back into the light cone, thereby increasing the percentage of light that can escape in the vertical direction as shown in Figure 2.7(c).

The far-field optimization reduces the Q-factor of the cavity and hence the enhancement of light by the Purcell effect. Thus, there is a trade-off between increasing the amount of light being collected vertically and the enhancement of light achieved by the Purcell effect. A good compromise between the two was found, where the Q-factor drops only by a small amount while the vertical light emission is increased by almost an order of magnitude; see point 6 in Figure 2.7(b) [8].

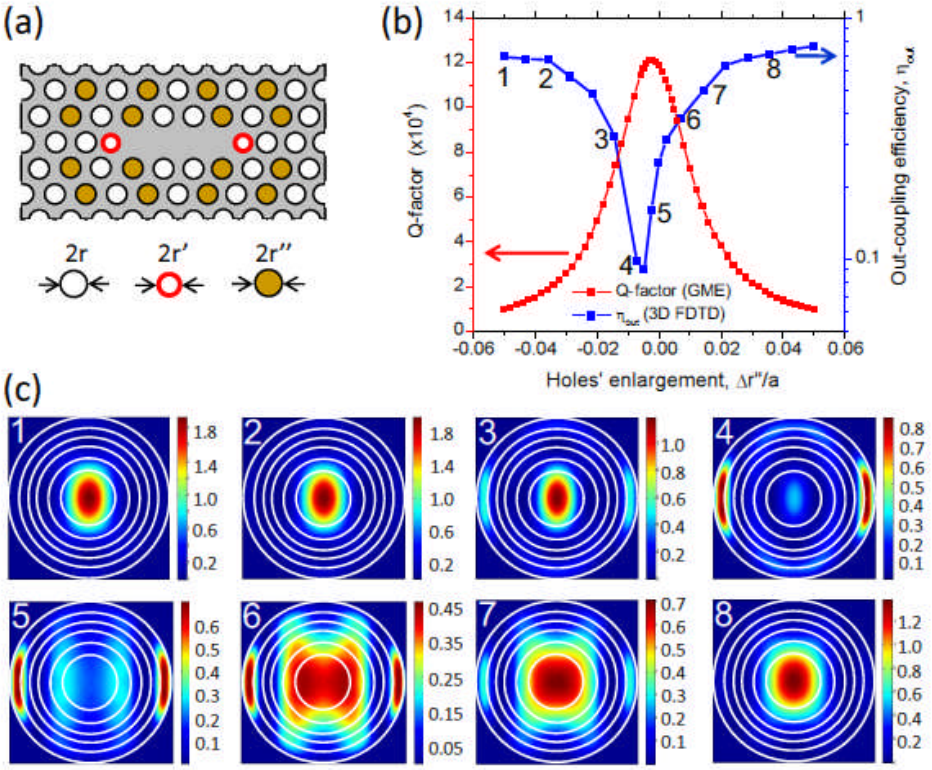

Figure 2.7: (a) Schematic of the L3 PhC cavity with modified holes to increase the Q-factor (red holes) and the far-field optimization (brown holes). (b) Trade-off between increase of vertical out-coupling efficiency and reduction of Q-factor. (c) Electric field intensity profile ($|E|^2$) giving far-field patterns for different values of hole enlargement. The numbers correspond to the numbering in (b), which corresponds to the different values of hole enlargement. The vertical emission intensity is increased with bigger change in the hole diameter but the Q-values decrease. The best compromise occurs at the crossing of the out-coupling efficiency and the Q-factor curve, i.e. point 6. Reproduced from [8][2].

In practice, the linewidth of the emitter also limits the Purcell factor. Thus, if the emission from the emitter is broad, low Q-factor cavities would give the same result, allowing the possibility of gaining better vertical collection of light. Depending on the requirements of our experiments, different values of far-field optimization were used. In most of the experiments in this project and presented in the following chapters, I used a modified L3 PhC cavity with parameters given in Table 2.1.

Table 2.1: Design parameters of PhC cavity

Parameters	**Value**
Lattice Period, a	420 nm
Fill factor, r/a	0.265, 0.28
Reduction of hole size adjacent to the cavity, $\Delta r'$	0.06a
Lateral displacement of the holes adjacent to the cavity, Δx	0.15a, 0.16a
Increase of hole radius for far-field optimization, $\Delta r''$	6 nm

2.2 Fabrication

As the features of PhC cavities are sub-micron, electron-beam or deep UV lithography is required for defining the PhC structures. Deep UV lithography has the advantage of parallel processing and thus is more useful for commercial production, whereas versatility is the fundamental advantage of e-beam lithography. In this project, e-beam lithography was used to fabricate the PhC cavities. The schematic of the fabrication steps involved in the fabrication of PhC cavities is shown in Figure 2.8 and explained below.

Step 1: Deposition of resist

For the fabrication of PhC cavities, we use the silicon on insulator (SOI) platform, manufactured by the Smart Cut^{TM} method and purchased from Soitec. The wafer has a 220 nm top silicon layer with a 2 µm silica layer below. The sample was first cleaned with acetone and isopropanol (IPA) with gentle ultrasonic agitation to remove any contamination. After cleaning, a layer of e-beam resist (ZEP520A, undiluted) was deposited on top of the SOI wafer by spin coating at 3200 rpm for one minute. This gives around a 400 nm thick layer. The sample was then baked at 180 ^{o}C for 10 min to evaporate the solvents in the resist layer. This helps to cure the resist. The ZEP520A resist is UV light sensitive and needs to be protected from direct exposure.

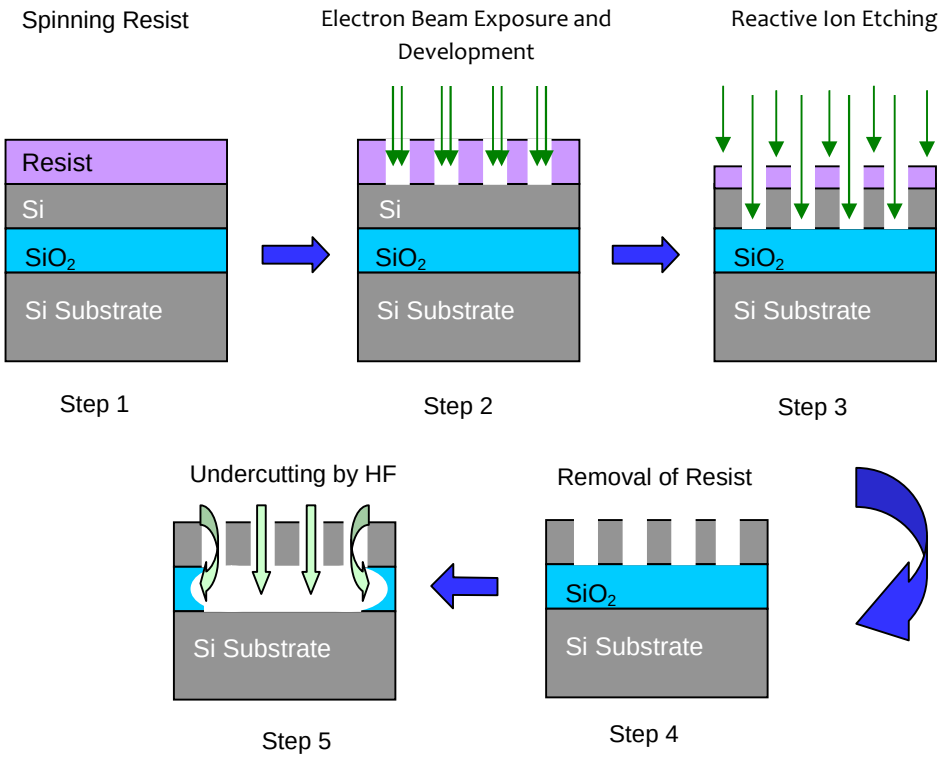

Figure 2.8: Schematic of steps required for the fabrication of air-bridge PhC nanocavity.

Step 2: E-beam exposure and development

The PhC structures with required design parameters were transferred into the lithography package "ELPHY". The pattern was then written into the resist using a hybrid LEO1530 SEM/ RAITH ELPHY PLUS electron-beam nanolithography system. An acceleration voltage of 30 kV and a base dose of 55 μC/cm^2 were used. Depending on the type of resist, positive or negative, the e-beam exposure either breaks the long polymer chains of the exposed area (positive resist) or interlinks it (negative resist). Using a developer, either the exposed area (in the case of positive resist) or the unexposed area (in the case of negative resist) is dissolved. Xylene was used as a developer for ZEP520A resist, which is a positive resist and hence the areas exposed by the e-beam were dissolved to form a mask. The development was done for 45 seconds at 23 ^{o}C with constant stirring. The result of e-beam exposure and development is shown schematically in step 2 of Figure 2.8. If the base or clearing dose is low, the

resist from the exposed area will not be dissolved properly. Thus, first dose tests were carried out to find the optimum dose, which was then used for the final samples.

An important feature to consider during the e-beam exposure is the backscattering of electrons from deep within the substrate material. As depicted in Figure 2.9(a), in addition to the direct exposure, some areas of the resist are also exposed by back-scattered electrons. Due to this second exposure, fabrication errors are expected unless it is ensured that all areas of the resist are exposed with the same dose. An adjustment is made in the design dose of the pattern to cater for the electron backscattering effect. This adjustment is called “proximity error correction”. In this method, different areas of the resist are exposed by a different primary dose. The areas in the centre are usually exposed with lower primary dose compared to the corner, as shown in Figure 2.9(b), because they receive backscattered electrons from all neighbouring sites, while the areas in the corners do not.

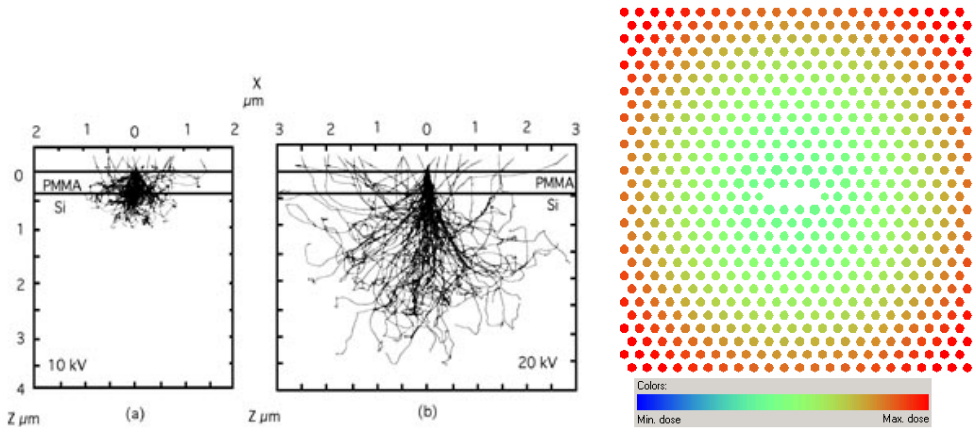

(a) (b)

Figure 2.9: (a) Exposure of the resist by back-scattered electrons [9][3]. (b) Proximity error correction. The areas away from the middle of the structure are exposed with a higher primary dose.

In addition to proximity error correction, an adjustment in the holes diameter was also carried out, in which the radius of the holes was reduced by 20 nm in the design. This adjustment was carried out to cater for holes enlargement during the e-beam exposure and development/etching process that we observed empirically. This 20 nm

pre-bias helps to achieve the target geometrical parameters of the structures after fabrication.

Step 3: Reactive ion etching (RIE)-transfer of patterns into SOI

After the development process in step 2, a mask consisting of the required patterns is created. The required structures were transferred into the top silicon layer of SOI by etching the areas not covered by the resist. The etching was carried out using CHF_3/SF_6 gas chemistry in the reactive ion etching setup. The RIE system consists of two parallel electrodes, placed in a high vacuum chamber. The top electrode is grounded, while RF is applied to the bottom electrode. An RF frequency of 13.56 MHz is used. The sample to be etched is placed on the bottom electrode. The gases are injected into the chamber, which are ionized by the RF field and start the plasma. Due to the electric field, the ions and electrons are accelerated between the electrodes. Since electrons are lighter than ions, they reach the electrodes quicker than the heavier ions and negative charge accumulates on the both electrodes. As the top electrode is grounded this charge is fed away from the system, giving rise to a negative DC bias of typically a few 100 V at the bottom electrode, which in turn attracts the positively charged ions that are then pulled to the bottom electrode with higher energy, where the sample to be etched is placed. The impinging ions etch the material by a combination of physical and chemical effects; fluorine as the active ingredient of etch gas chemically reacts with silicon to form gaseous silicon tetrafluoride. It also physically etches silicon by sputtering. The chemical etching is usually isotropic, while physical etching helps to make the etching process more anisotropic, helping to obtain vertically etched surfaces. In addition to it, a third effect involved in the RIE processes that also contributes to the verticality is the formation of a passivation layer at the surface. A careful balance between chemical and physical etching helps to have the best etching results. A schematic of the RIE mechanism is given in Figure 2.10.

In addition to the gas chemistry, the etching process depends on a few other factors. These include the gas flow rates, the chamber pressure, the level of DC bias and the correct etching time to stop the etching at the interface of top silicon layer and embedded silica

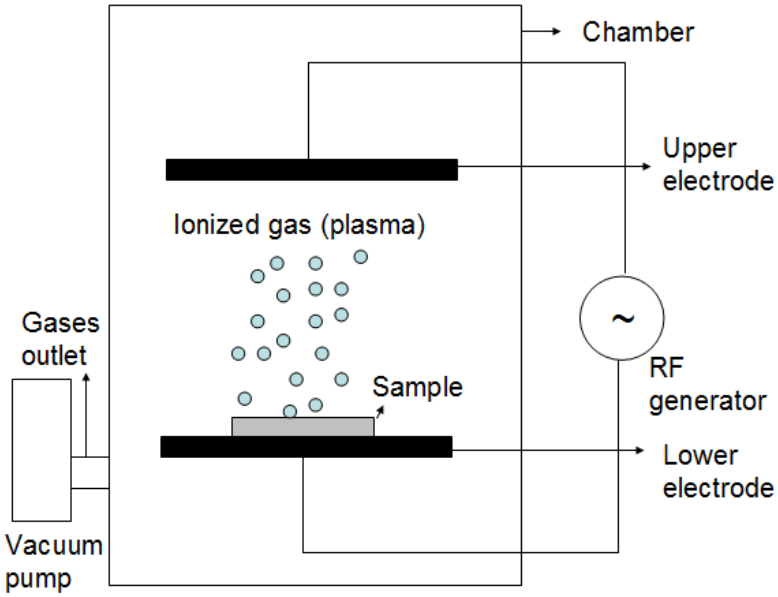

Figure 2.10: Schematic of reactive ion etching mechanism.

For etching of the PhC structures, a chamber pressure of 0.05 mbar and a plasma power of 20 watts, giving -310 V DC bias, were used for 2 minutes. This process etches PhC holes into the top silicon layer of SOI. In addition to etching silicon, the resist mask is also etched with almost the same etching rate and hence we used a resist layer with twice the thickness of the top silicon layer. We believe that the low selectivity helps realise smooth side walls by minimizing the transfer of roughness from the resist to the silicon.

Step 4: Removal of resist

After the etching process, the remaining resist was removed by a "resist remover" (a chemical specifically designed for this purpose). For ZEP520A resist, a microposit^{R} 1165 remover by Shipley is usually used. The sample was placed in 1165, with gentle ultrasonic agitation, followed by an acetone and IPA cleaning. If the resist is not properly removed by this method, the sample can also be kept in a piranha solution, which is a mixture of H_2SO_4 and H_2O_2 (3:1 ratio) for 5 minutes or until the resist is removed completely. The Piranha cleaning is stopped by a rinse in deionized (DI) water followed by acetone and IPA cleaning.

Step 5: Undercutting

After the transfer of PhC structures into the silicon layer and removal of the resist, the silica layer beneath the PhC was etched away by using hydrofluoric acid (HF). A solution of diluted HF acid (HF:DI water 1:5) was used for 20 minutes, which etches around 1.5 µm of silica by the following chemical reaction:

$$SiO_2 + 6HF \longrightarrow H_2SiF_6 + 2H_2O$$

The etching is terminated by rinsing in DI water. This creates a freestanding PhC membrane, as depicted in Figure 2.8, step 5. SEM pictures of typical fabricated PhC L3 cavities are shown below (Fig. 2.11).

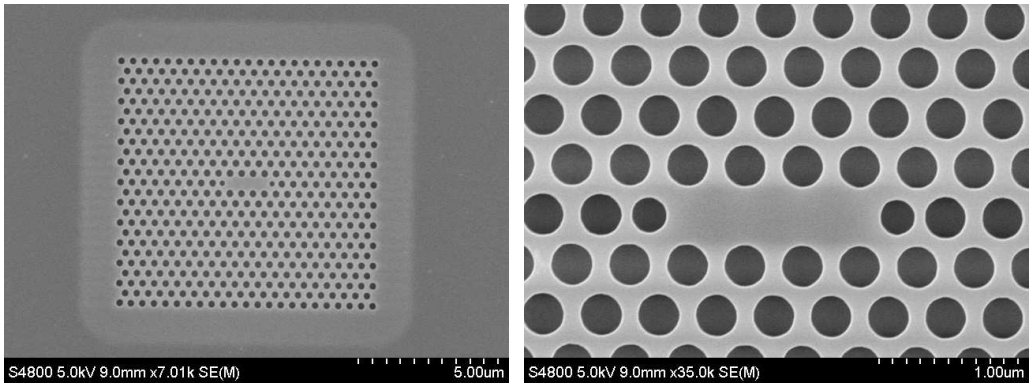

Figure 2.11: SEM images of the fabricated modified L3 PhC cavity. The shaded region around the PhC clearly indicates the undercut. The right hand side image is the zoomed-in SEM image of the left one around the cavity area.

2.3 Characterization

There are three main properties of the PhC cavities we want to measure: the quality factor *Q*, the resonance wavelength and the luminescence from the cavity. For measuring the Q-factors and the resonance wavelength, the resonance scattering (RS) method [10] was used. The photoluminescence and electroluminescence were measured by a µPL setup. The resonance wavelength of the cavity can also be determined from the luminescence spectra of the cavity.

The details of the resonance scattering (RS) and µPL setup are given in the next sections.

2.3.1 Resonance scattering method/setup to measure Q-values of the PhC cavity

The cavity Q-factors were measured by the resonant scattering of the incident light at room temperature. The resonant scattering technique for measuring the Q-factors of the cavities was developed by our collaborators at the University of Pavia, Italy. The schematic of the RS setup used for these measurements is shown in Figure 2.12.

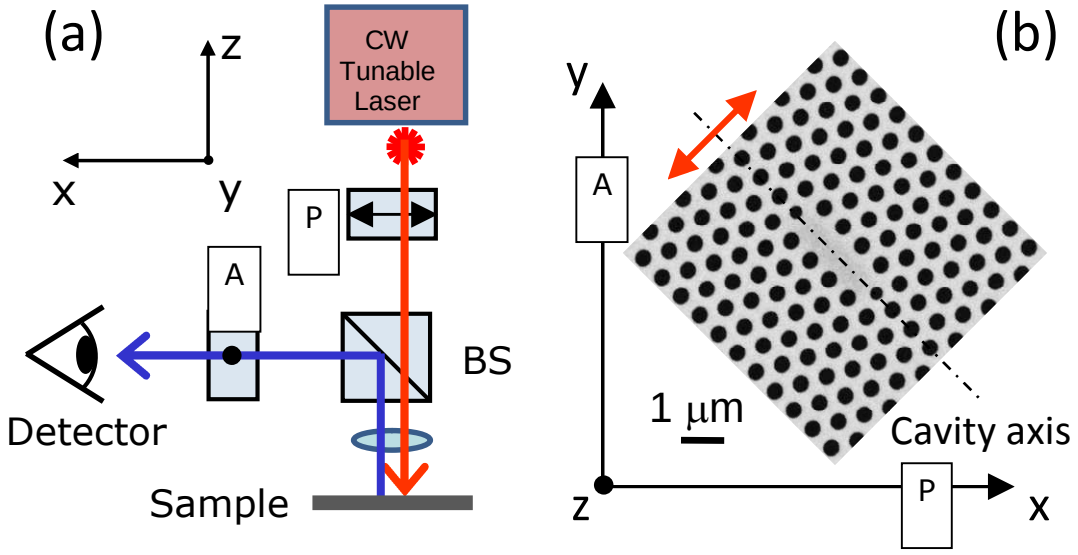

Figure 2.12: (a) Schematic of the RS setup used to measure the Q-factor and resonance position of the PhC cavity. (b) Orientation of the sample with respect to polarizer and analyzer [10][4].

The setup consists of a CW tunable laser, an x-polarized dichroic polarizer (P), a beam splitter, a high numerical aperture objective (NA=0.8), an analyzer (A) and a detector. The detector is an InGaAs photodiode with adjustable gain. A lock-in amplifier can also be used to improve the signal to noise ratio. For this purpose, an optical chopper wheel was used to modulate the input light, with its modulation frequency being the reference for the lock-in amplifier.

The light from a tunable CW laser was x-polarized by a dichroic polarizer and incident on the PhC cavity sample. The sample was placed at an angle of 45^{o} with respect to polarization of both the polarizer and an analyzer, as shown in Figure 2.12.

The light was focussed on the sample by an objective. The light scattered from the sample was collected by a beam splitter and fed to the detector after passing through an analyzer.

When the incident x-polarized light is off resonance with the xy polarized cavity, the light scattered from the cavity maintains its polarization. The scattered light is collected by the beam splitter and analyzed at the analyzer. Since the analyzer passes only the y-component of the field, the collected light is blocked at the analyzer and the detector does not detect any light – only background noise. On the other hand, when the incident x-polarized light is on resonance with the cavity, which is oriented in xy-direction, it will couple in and out of the cavity and acquire a y-component. The collected light will then pass through the analyzer and a signal will be recorded by the detector at the resonance wavelength of the cavity.

When the sample is placed at 0^o or 90^o with respect to the polarizer or the analyzer, no signal is detected for any case ideally, however, disorders in the structures can change this slightly [11]. For the signal to be detected, two conditions must be satisfied. Firstly, the incident light should have a field component along the polarization of the cavity mode, indicated by the red arrow in Figure 2.12(b), to have interaction with the cavity. Secondly, the collected scattered light should have a field component along the analyzer, y-direction. Therefore, to have maximum signal, the sample is placed with the cavity axis at 45^o.

The Q-factor of the cavity can then be calculated by fitting the resonance signal obtained with the Lorentzian or Fano line shape, depending on the ratio between the on-resonance and off-resonance transition amplitudes in the scattering process. If the resonant and off-resonance scattering amplitudes are comparable, the line shape is an asymmetric Fano type. On the other hand, if the resonantly scattered component is larger or smaller than the direct scattered component, then it gives rise to the symmetric Lorentzian line shape. The origin of symmetric or asymmetric line shapes can be explained by the Fano quantum interference effect [12], which describes the interaction between the two channels during the scattering phenomena. This effect is noticed when the incident light is scattered by two different phenomena, one directly toward the continuum of extended states and the other resonantly through a discrete energy level [12]. The asymmetry arises due to interference of these two different routes of

scattering. An example of RS signal used for the measurement of the Q-factors is given in Figure 2.13.

This approach to measure the Q-factors is in principle limited only by the linewidth of the laser source. Our setup has a laser source with a linewidth of 2.2 pm, which allows us to measure Q-factors up to 700,000.

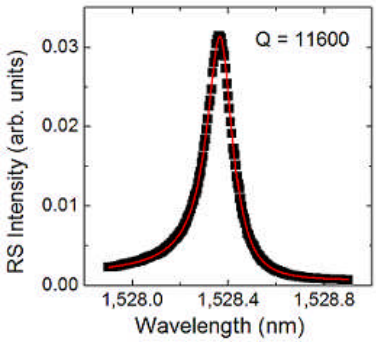

Figure 2.13: Resonant scattering signal from a far-field optimized PhC L3 cavity.

2.3.2 Photoluminescence setup

The photoluminescence and electroluminescence of PhC cavities were measured using a µPL setup at the University of Pavia, Italy. The schematic of the setup is shown in Figure 2.14.

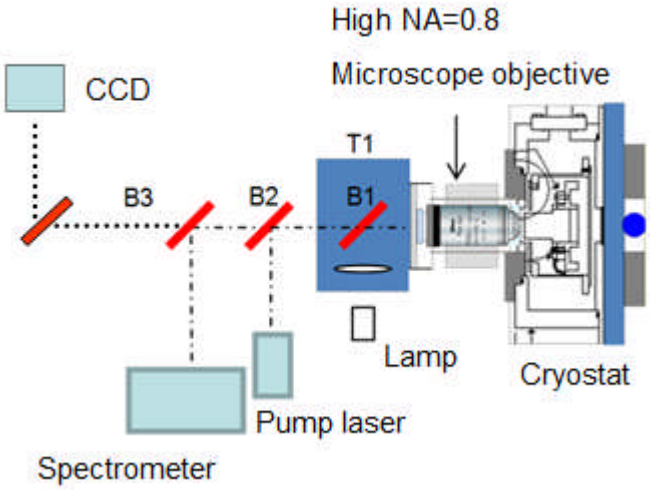

Figure 2.14: Schematic of µPL setup used to measure the PL of SOI and PhC cavity.

The setup consists of 3 beam splitters (indicated by B1, B2 and B3), a high numerical aperture objective (NA=0.8), halogen lamp, CW laser at 640 nm, CCD camera, grating spectrometer equipped with liquid nitrogen cooled InGaAs detector, the liquid helium cryostat (Janis ST500) and the piezo controlled nano-positioners.

The sample is placed on the piezo-electrically controlled nano-positioner inside the cryostat. A CW laser at 640 nm is used as the pump laser, whose output was tightly focused to 1 μm^2 on the cavity by using a high numerical aperture (NA=0.8) objective. The incident light generates photo-carriers that recombine radiatively, generating light in the cavity. The emitted light is collected vertically by the same objective and fed into the grating spectrometer equipped with an InGaAs detector to provide the spectrum of the light collected from the sample. An example of the PL spectrum obtained from the PhC cavity, showing six emission peaks, corresponding to the fundamental and higher order modes of the cavity is shown in Figure 2.15. To align the sample with the laser spot, the image of the sample is taken at the CCD camera by using the halogen lamp and the objective. As the setup is equipped with the cryostat, low temperature measurements can also be carried out using this setup. The cryostat chamber can also be used to introduce different gases to change the refractive index of the surrounding medium in order to investigate the effect of refractive index change on the emission line, which is a technique I describe in Chapter 5.

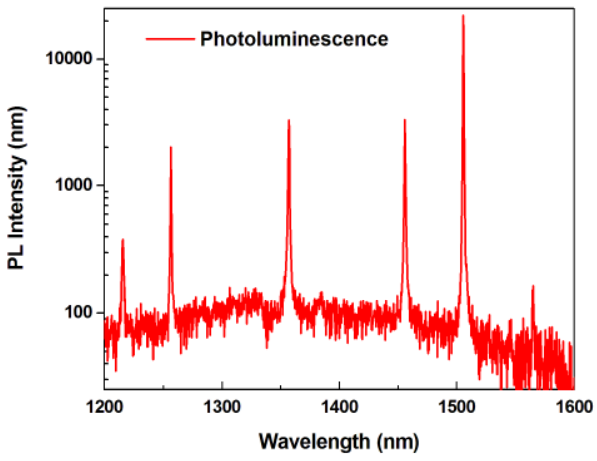

Figure 2.15: PL spectra of L3 PhC cavity taken by the µPL setup, showing emission lines corresponding to fundamental and higher order modes of the cavity.

2.4 Conclusions

The photonic crystal L3 cavities, having fundamental resonance wavelengths at 1500 nm and 1300 nm are successfully designed and fabricated by e-beam lithography. The passive Q-factors of these cavities are measured to be 100k. The cavities are optimized to extract maximum light in the vertical direction, with some compromise in the Q-factors. The characterization methods to measure the resonance wavelengths, Q-factors and luminescence of the cavities by resonant scattering and micro-PL setup are discussed. Thus, the work in this chapter has provided me all the necessary tools to carry out the experiments on the enhancement of light emission from silicon PhC nano cavities.

References

[1] B.-S. Song, S. Noda, T. Asano, and Y. Akahane, “Ultra-high-Q photonic double-heterostructure nanocavity,” Nat. Materials 4, 207-210 (2005).

[2] T. Tanabe, A. Shinya, E. Kuramochi, S. Kondo, H. Taniyama, and M. Notomi, “Single point defect photonic crystal nanocavity with ultrahigh quality factor achieved by using hexapole mode,” Appl. Phys. Lett. 91, 021110 (2007).

[3] G.-H. Kim, Y.-H. Lee, A. Shinya, and M. Notomi, “Coupling of small, low-loss hexapole mode with photonic crystal slab waveguide mode,” Opt. Express 12, 6624-6631 (2004).

[4] K. Welna, S. L. Portalupi, M. Galli, L. O'Faolain, T. F. Krauss, "Novel dispersion-adapted photonic crystal cavity with improved disorder stability," IEEE J. Quant. Electron. 48, 1177-1183 (2012).

[5] Y. Akahane, T. Asano, B.-Shik Song, and S. Noda, “High-Q photonic nanocavity in a two-dimensional photonic crystal,” Nature 425, 944-947 (2003).

[1]Reprinted by permission from Macmillan Publishers Ltd: [Nature] (doi:10.1038/nature02063), copyright (2003).

[6] L. C. Andreani, D. Gerace, and M. Agio, “Gap maps, diffraction losses, and exciton–polaritons in photonic crystal slabs,” Photon. Nanostruct. Fundam. Appl. 2, 103–110 (2004).

[7] N.-V.-Q. Tran, S. Combrié, and A. De Rossi, “Directive emission from high-Q photonic crystal cavities through band folding,” Phys. Rev. B 79, 041101 (2009).

[8] S. L. Portalupi, M. Galli, C. Reardon, T. F. Krauss, L. O’Faolain, L. C. Andreani, and D. Gerace, “Planar photonic crystal cavities with far-field optimization for high coupling efficiency and quality factor,” Opt. Express 18, 16064-16073 (2010).

[2]Reprinted with permission. Copyright [2010], Optical society of America

[9] D. F. Kyser, and N. S. Viswanathan, "Monte Carlo simulation of spatially distributed beams in electron-beam lithography," J. Vac. Sci. Technol. 12, 1305-1308 (1975).

[3]Reprinted with permission. Copyright [1975], American Institute of Physics.

[10] M. Galli, S. L. Portalupi, M. Belotti, L. C. Andreani, L. O’Faolain, and T. F. Krauss, “Light scattering and Fano resonances in high-Q photonic crystal nanocavities” Appl. Phys. Lett. 94 , 071101 (2009).

[4]Reprinted with permission. Copyright [2009], American Institute of Physics.

[11] S. L. Portalupi, M. Galli, M. Belotti, L. C. Andreani, T. F. Krauss, and L. O'Faolain, "Deliberate versus intrinsic disorder in photonic crystal nanocavities investigated by resonant light scattering," Phys. Rev. B 84, 045423 (2011).

[12] U. Fano, "Effects of configuration interaction on intensities and phase shifts," Phys. Rev. 124, 1866 (1961).

Chapter 3

Enhancing silicon emission by incorporating hydrogen defects and Purcell effect

In Chapter 1, I gave a review of different techniques used to enhance emission from silicon, with their advantages and shortcomings. One such route is to create defects in the silicon lattice to create defect luminescence. Among the many different methods to induce defect luminescence, one method is to introduce hydrogen related defects in silicon by hydrogen plasma treatment or ion implantation, discussed in Section 1.3.3.2.3. The same section also discusses the model of carrier recombination at the hydrogen defects to increase the radiative emission.

In the present chapter, I present the experimental results on the enhancement of emission from a silicon photonic crystal (PhC) nanocavity. The hydrogen defects are incorporated by two different methods, hydrogen plasma treatment and ion implantation, and their results are compared. The limit of emission enhancement by this method is investigated. The effect of different annealing conditions on the defects and the corresponding effect on the emission level are reported. Transmission electron microscopy (TEM) was carried out by collaborators at Catania, Italy, to understand the nature of different types of defects created and their relation with the emission established. At the end, by incorporating optically active defects into silicon PhC L3 nanocavity, I demonstrate an optically pumped silicon nanolight source at room temperature with narrowband emission anywhere in the 1300-1600 nm wavelength range.

3.1 Hydrogen defects in silicon on insulator

The silicon on insulator (SOI) wafer we used consists of a thin top silicon layer of 220 nm thickness that is separated from the bottom silicon substrate by a 2 μm silica layer. The process by which SOI wafers are manufactured is called the Smart Cut^{TM} process. The steps involved in the Smart Cut^{TM} process are discussed below and shown schematically in Figure 3.1.

The Smart Cut™ process starts with a silicon wafer, which is oxidized to create a silica layer. The oxidized wafer is implanted with hydrogen from the top. This creates a defect layer in the silicon slab at a depth of few hundred nanometers. The slab is then flip-chip bonded onto the silicon carrier wafer. The whole structure is then annealed, which creates bubbles at the implanted defect layer. The top silicon layer splits by high temperature annealing at the site of the defect layer. The holder is then cut to form the substrate. The surface is usually very rough, which is chemically polished to turn it into smooth top surface. The separated silicon layer can be re-used for step 1.

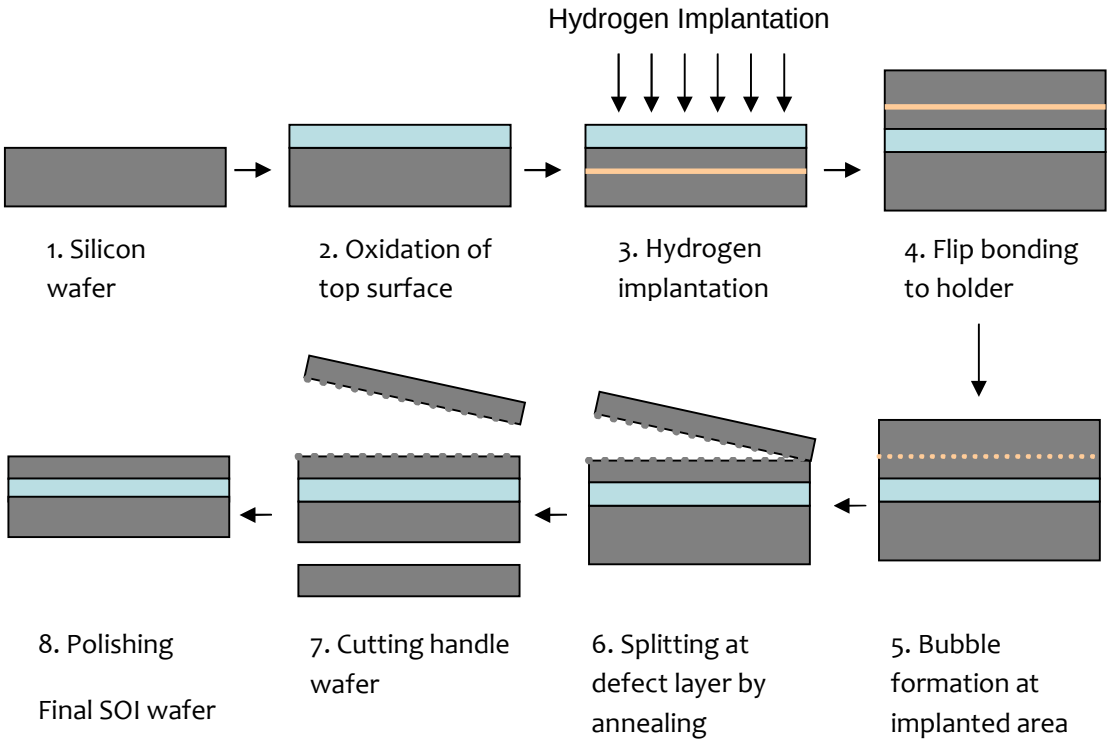

Figure 3.1: Process flow of Smart Cut™ process used to manufacture SOI. The third step involves hydrogen implantation, which creates optically active defects.

The implantation of hydrogen in step 3 creates defects in silicon. Although the Smart Cut™ process involves high temperature annealing (at 1100 ^{o}C), which removes most of these defects, some of them remain and can generate photoluminescence (PL).

3.2 Photoluminescence of SOI vs. Czochralski silicon (Cz-Si)

The presence of optically active defects in SOI is evident immediately when a PL spectrum from SOI is compared with that of Cz-Si. The PL of SOI and Cz-Si was taken by the experimental setup described in Chapter 2. The room temperature PL spectra of SOI and Cz-Si are shown in Figure 3.2.

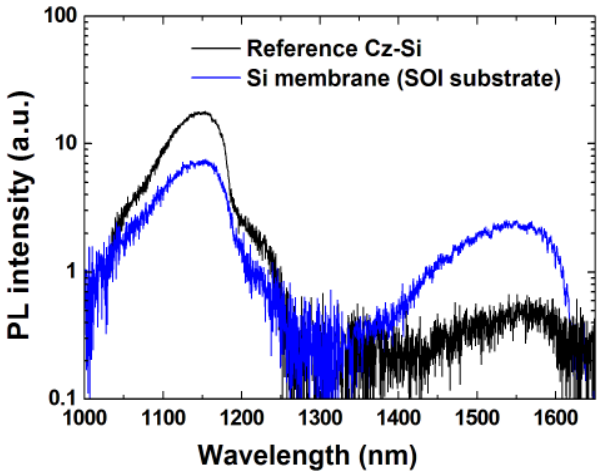

Figure 3.2: Comparison of room temperature PL spectra of SOI and Cz-Si [1][1].

As clearly shown in Figure 3.2, the sub-bandgap PL intensity (1300-1600 nm) of SOI is higher compared to that of Cz-Si. This is due to the presence of leftover defects, created in the top silicon layer during manufacturing process of SOI, as described above. These defects create midgap defect states in silicon that help to enhance the probability of radiative recombination by providing momentum conservation, as explained in Section 1.3.3.2.

3.3 Purcell enhancement

The emission from the optically active defects in SOI can be enhanced on resonance with a high Q/V cavity by the Purcell effect, discussed in Section 1.5.1. We used a modified L3 photonic crystal cavity, whose design has already been discussed in detail in Section 2.1. A cavity with a fundamental resonance at 1550 nm was used, as the emission band due to hydrogen defects in SOI is centred at 1550 nm. The band is very

broad, however, so a cavity operating anywhere in the 1300-1600 nm wavelength range could be used.

The room temperature photoluminescence spectrum of the PhC cavity was recorded by the setup described in Section 2.3.2. The PL spectra of the L3 PhC cavity are shown in Figure 3.3, with theoretically calculated modes in the top panel. The spectrum shows seven narrow emission lines. These lines correspond to the modes of the cavity, with the fundamental at 1550 nm, while the rest of them are the higher order modes. The modes were calculated by guided mode expansion method (GME) [2] (calculation of modes by GME method: courtesy of Dr Dario Gerace, University of Pavia). There is a nice match between the theoretically calculated modes and the experimentally measured emission lines.

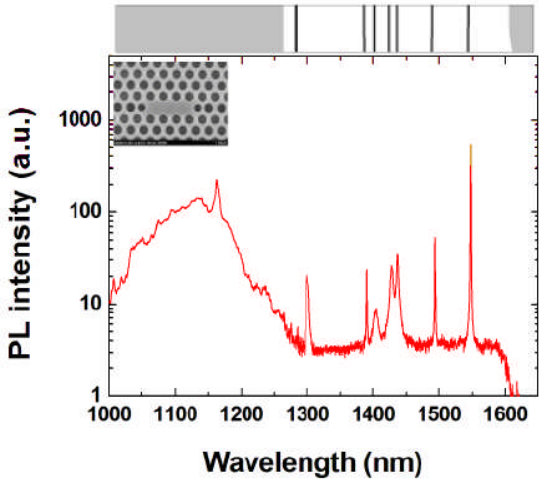

Figure 3.3: PL spectra of L3 PhC cavity, showing seven narrow emission lines, corresponding to modes of the cavity. The theoretically calculated modes are shown on the top panel and match very well with the experimental result. The inset shows the SEM picture of measured L3 PhC cavity [1] [1].

3.3.1 Estimation of the Purcell factor

As discussed in Section 1.5, the Purcell factor gives the factor by which the emission of an emitter is enhanced by the Purcell effect and scales with Q/V of the cavity. The Purcell factor can be extracted from the time resolved PL measurements. Unfortunately, our time resolved PL measurements were limited by the laser switch-off time, further details given in Section 3.5.1.5. Therefore, it was not possible to extract the value of

Purcell factor from the time resolved PL measurements. We took an alternative route, which roughly estimates the Purcell factor in our emitter-cavity coupled system. Our method of estimation of Purcell factor is explained below.

There are only two effects that determine the amount of light measured out from a PhC cavity or any other kind of optical cavity:

1. Light redistribution, called cavity enhancement, which is simply re-direction of light emission in the cavity mode and suppression of light emission elsewhere (just like a macroscopic Fabry-Perot does).
2. Purcell enhancement, which increases light emission through a reduction of the radiative lifetime.

In order to estimate the Purcell factor from the experimentally measured PL enhancement, it is necessary to separate the lifetime and light redistribution (extraction effects). By separating the lifetime and light extraction effects, the Purcell factor can be calculated by Equation 3.1 provided that the internal quantum efficiency at the cavity emission peak and the background is not changed. In our emitter-cavity coupled system, the internal quantum efficiency at the peak and at the background is not changed, as it is demonstrated by the fact that the tuning of the cavity at a different wavelength across the background always gives the same cavity peak intensity. This is only possible if the internal quantum efficiency of the emitters (defects) is the same in the two cases. Thus, following equation can be used for a rough estimation of the Purcell factor,

$$F_p = \frac{\gamma}{\eta_{cavity} / \eta_{membrane}} \qquad \text{Equation 3.1}$$

where γ is the experimentally measured total PL enhancement factor, while η_{cavity} and $\eta_{membrane}$ are the light collection efficiencies from an unpatterned silicon membrane and on-resonance cavity, respectively. The ratio $\eta_{cavity}/\ \eta_{membrane}$ is the light extraction enhancement without the effect of cavity (off-resonance).

The value of γ is measured experimentally from the comparison of PL spectrum of the PhC cavity and the unpatterned silicon membrane, as shown in Figure 3.4.

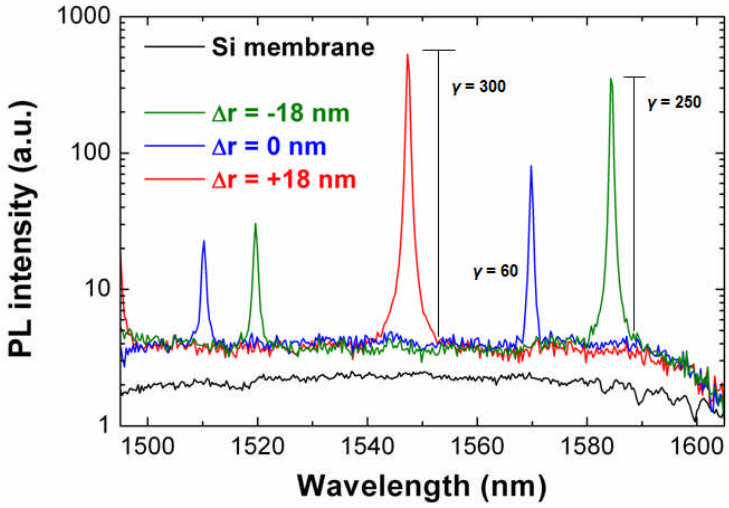

Figure 3.4: PL enhancement factor, γ, between the fundamental cavity mode and the silicon membrane for three different far-field optimization parameters [1] [1].

The measured values of γ for three different far-field optimization parameters, Δr = -18 nm, 0 nm and +18 nm are 250, 60 and 300, respectively.

The value of $\eta_{membrane}$ is calculated by geometrical considerations as described below with the help of Figure 3.5, which leads to the following equation:

$$\eta_{membrane} = \frac{\Omega}{2\pi} = \int_0^{2\pi}\int_0^{\theta} \sin\theta' d\theta' d\phi = 1 - \cos\left[\sin^{-1}\left(\frac{NA}{n}\right)\right] = 0.036 \qquad \text{Equation 3.2}$$

Where n is the effective refractive index of the silicon slab, taken as 3, and NA=0.8 is the numerical aperture of the collection objective.

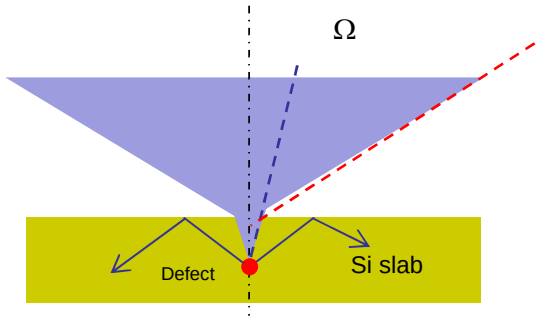

Figure 3.5 Geometrical considerations for calculating light collection efficiency from unpatterned silicon membrane [1] [1].

The value of η_{cavity} was calculated numerically by FDTD. The calculated values were 0.8, 0.2 and 0.9 for Δr = -18 nm, 0 nm and +18 nm, respectively. Using Equation 3.1, the value of the Purcell factor was calculated to be in the range 10-12 and this value is consistent for all the three cases, as shown in the Table 3.1, indicating that the model of calculating the Purcell factor is correct.

Table 3.1: Summary of calculated values of the Purcell factor.

Δr	Extraction enhancement, $\eta_{cavity}/\eta_{membrane}$	Total PL enhancement, γ	Purcell Factor, F_p
-18 nm	22.22	250	11.25
0 nm	5.55	60	10.81
+18 nm	25	300	12

The value of the Purcell factor we achieved (F_P≈10-12) is the highest ever reported from a silicon PhC nanocavity at room temperature.

To achieve such a high Purcell factor, the emission line of the emitter should be narrower than the cavity line. The active Q-factor of the PhC cavity measured by the resonance scattering (RS) method is around 10000 (details of the RS method and setup is given in Chapter 2). This implies that, the linewidth of the cavity resonance is 0.15 nm ($\Delta\lambda=\lambda/Q$). This high value of the Purcell factor indicates that the emission line coupled to the PhC cavity should have narrow linewidth (≈0.15 nm). This shows that, although the overall emission from SOI is broadband, the emission from each individual defect is very narrow. From this, it can be inferred that, the broadband emission is an aggregate of inhomogeneously broadened emission lines from individual defects, whose numbers are perhaps in the millions. This inhomogeneously broadened emission from individual defects can be compared to the inhomogeneously broadened emission from III-V quantum dots created by Stranski-Krastanov growth mode. Thus, the very narrow emission (<0.15 nm) from individual defects feeds the cavity and is responsible for the high Purcell factor of 10-12. This high value of Purcell factor increases the PL level by a factor of 300, making it comparable to the emission level at the silicon band-edge.

The Q-factor of the cavity extracted from the emission line is 3000, which is lower than the value measured by the RS method, i.e. 10000. This reduction in Q-factor is due to the increased free carrier absorption (FCA), induced by optical pumping above the silicon bandgap. The blue shift of the cavity peak we observe on increasing the optical pump power also proves this point [3].

3.4 Temperature stability

One very interesting feature of our approach is the temperature stability of the emission, which distinguishes this approach from many other silicon emission enhancement techniques that only work at low temperatures. As shown in Figure 3.6, at off-resonance (no Purcell effect) the PL intensity reduces to a low level very quickly as the temperature is increased from cryogenic to room temperature. On the other hand, on resonance with the cavity (presence of Purcell effect), the emission intensity is reduced only by 40%. This implies that the temperature stability of the emission is due to the Purcell effect.

The temperature stability due to the Purcell effect can be explained by the following equation of the radiative emission efficiency:

$$\eta_{rad} \propto \frac{\tau_{nonrad}}{\tau_{rad} + \tau_{nonrad}} \propto \frac{\tau_{nonrad}}{\frac{\tau_{rad,0}}{F_P} + \tau_{nonrad}} \qquad \text{Equation 3.3}$$

where η_{rad} is the radiative recombination efficiency, F_p is the Purcell factor, while τ_{rad}, $\tau_{rad,0}$ and τ_{nonrad} are the radiative recombination time, the native radiative recombination time (in the absence of Purcell effect) and non-radiative recombination time, respectively.

The non-radiative recombination processes are due to Auger and surface recombination effects. Their recombination times are temperature dependent, and decrease with the increase of temperature. Thus, at room temperature, the non-radiative recombination times become very short, of order of nanoseconds or below, and dominate over the radiative recombination. This causes the quenching of the emission at room temperature. If the emission from the defect is on resonance with the PhC cavity, the Purcell effect reduces the radiative lifetime, as is evident from Equation 3.3.

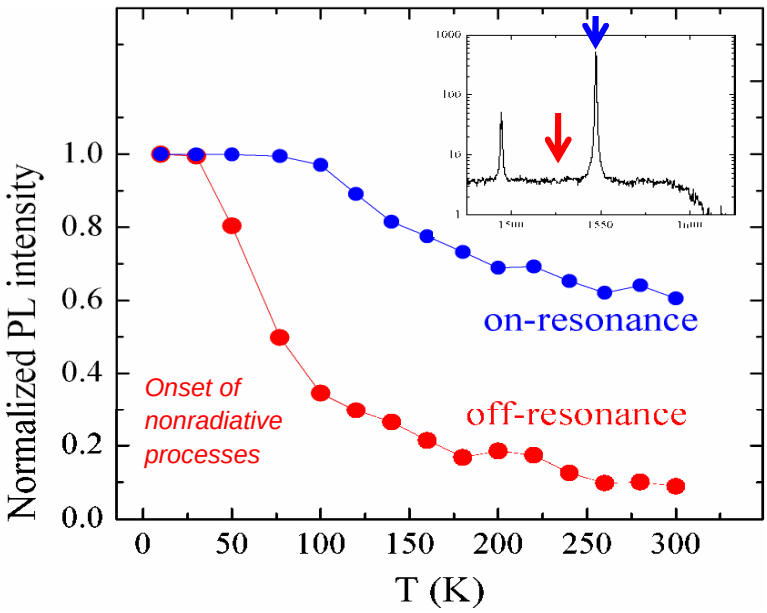

Figure 3.6: Temperature stability of the emission due to Purcell effect (on-resonance). In the absence of the Purcell effect (off-resonance), the emission quenches very quickly [1,3].

The larger the Purcell factor is, the greater the reduction in the radiative recombination time will be. The high Purcell factor reduces the radiative recombination time such that it becomes comparable to the non-radiative lifetime and hence maintains or only slightly reduces the emission when increasing the temperature from 10 K to room temperature.

The non-radiative carrier lifetime in the PhC structures is equal to 50-500 ps, as known from the literature [6,7]. Thus, keeping in view the temperature stability of the emission, the radiative lifetime on-resonance should be of the same order. From the estimated value of the Purcell factor (10-12), the native radiative lifetime ($\tau_{rad,0}$) would then be around 0.5-5 ns.

3.4.1 Arrhenius analysis - Another indication of the Purcell effect

A quantitative analysis of the temperature stability can be carried out by following [8]. The temperature dependent PL intensity can be given by the following equation:

$$I_{PL}(T) = PR\eta_{\text{int}}(T) \qquad \text{Equation 3.4(a)}$$

where P, R and η_{int} are the external photon detection probability, excitation rate and temperature dependent internal quantum efficiency, respectively.

The temperature dependent η_{int} can be expressed in terms of inter-band radiative and non-radiative recombination rates by the following equation:

$$\eta_{\text{int}}(T) = \frac{\Gamma_{rad}}{\Gamma_{rad} + \Gamma_{NR}(T)} \qquad \text{Equation 3.4(b)}$$

where Γ_{rad} is the radiative recombination rate while Γ_{NR} (T) is the non-radiative recombination rate, which is temperature dependent. Γ_{NR} (T) can be further expressed by the following expression:

$$\Gamma_{NR}(T) = \Gamma_{NR}^{0} \exp\left(\frac{-E_A}{K_B T}\right) \qquad \text{Equation 3.4(c)}$$

This equation represents the temperature dependent non-radiative decay rate of the carriers between two energy levels with energy difference E_A, following Boltzmann's statistics.

In the equation, E_A is the activation energy between two energy levels |1> and |2>, Γ^0_{NR} is the non-radiative decay rate to energy level higher than |2> and K_B is the Boltzmann constant. The physical meanings of all the terms used in Equations 3.4(a) to 3.4(c) are expressed schematically in Figure 3.7.

At the excitation rate R, the carriers at the energy level |1> can decay through two channels; either radiatively to state |0>, accompanied by an emission of photons, or non-radiatively to state |2>. They can further decay non-radiatively back to level |1>, as shown by Γ^*_{NR} (T) in Figure 3.7 or to higher level by the decay rate $\Gamma^0_{NR.}$ The Equations 3.4(a) to 3.4(c) come from the rate equations dealing with the steady state carrier density of the two energy states |1> and |2>. It is assumed that Γ^0_{NR} (T) >> Γ^*_{NR}(T) to ensure that the non-radiative decay dominates at higher temperature, which is the usual case for silicon.

Putting Equations 3.4(b) and (c) into Equation 3.4(a), the following equation is obtained.

$$\ln\left(\frac{I_{PL}(T^{0K})}{I_{PL}(T)} - 1\right) = \frac{-E_A}{K_B T} - \ln\left(\frac{\Gamma_{rad}}{\Gamma_{NR}^{0}}\right) \qquad \text{Equation 3.4(d)}$$

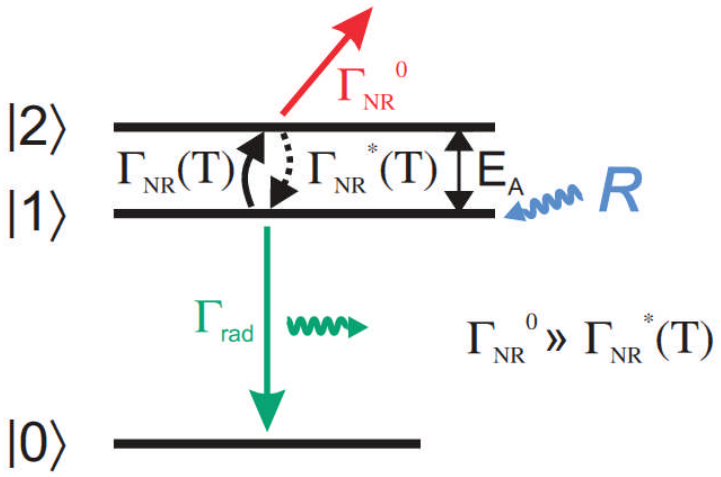

Figure 3.7: Energy level diagram expressing the physical meanings of the terms used in Equations 3.4(a-f) [8] [2].

$I_{PL}(T^{0K})$ is the PL intensity at 0 K. Normalizing its value to one, Equation 3.4(d) is reduced to the following equation:

$$\ln\left(\frac{1}{I_{PL}(T)}-1\right)=\frac{-E_A}{K_BT}-\ln\left(\frac{\Gamma_{rad}}{\Gamma_{NR}^0}\right) \qquad \text{Equation 3.4(f)}$$

Using Equation 3.4(f), an Arrhenius type plot can be plotted, where the values of $\ln\left(\frac{1}{I_{PL}(T)}-1\right)$ are plotted against inverse T on the abscissa. The values of $\ln\left(\frac{1}{I_{PL}(T)}-1\right)$ are plotted for both off-resonance and on-resonance with the PhC cavity. The plots are shown in Figure 3.8.

The activation energy, E_A, can be extracted from the slopes of the curves. The activation energies for both off-resonance and on-resonance PL were found to be almost the same: 22 and 23 meV. As activation energies for both cases are the same, the higher PL for the on-resonance case is due to the higher value of $\frac{\Gamma_{rad}}{\Gamma_{NR}^0}$, i.e., the radiative recombination rate at high temperatures is higher when the emitter is on-resonance with the cavity, compared to the off-resonance case.

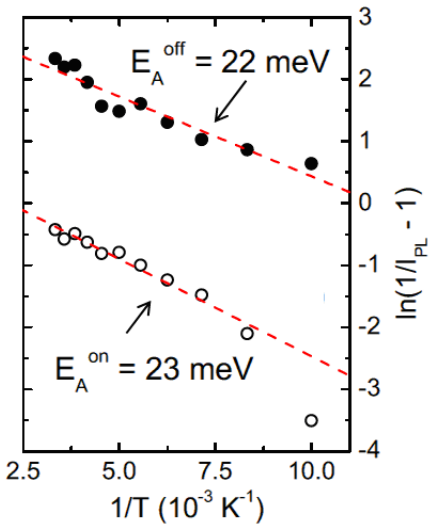

Figure 3.8: Arrhenius type plot of the PL intensity. The activation energy for both on- and off-resonance PL is the same indicating that the temperature stability arises from the Purcell effect [3] [3].

From this, it can be concluded that the higher PL level at room temperature is the result of increased internal quantum efficiency due to higher radiative recombination rate caused by the Purcell effect. Thus, the Arrhenius plot shows that it is the Purcell effect, which gives the temperature stability to the emission from the PhC cavity.

3.5 Enhancement of PL by incorporation of additional defects

By using only the leftover defects created during the manufacturing process of SOI, we have already achieved a cavity-enhanced emission line at 1500 nm, which has PL intensity greater than the band-edge emission from silicon. For practical applications, this emission level is still insufficient and there is a need to enhance the emission further. To further enhance the emission from SOI, we intentionally incorporated additional hydrogen related optically active defects. The following two methods were used for this purpose:

1. Hydrogen plasma treatment in a reactive ion etching system
2. Hydrogen implantation in an ion implanter

3.5.1 Enhancement of PL by hydrogen plasma treatment

As discussed in Section 1.3.3.2.3, the hydrogen plasma treatment of Cz-Si creates sub-bandgap luminescence bands measured at low temperature [9,10]. In this project, I carried out an investigation of using hydrogen plasma treatment to increase the emission from the top silicon layer of the SOI. In fact, I investigated different plasma compositions to study the effect of incorporating different ion species into the silicon and their effect on the PL and Q-factors of the PhC cavity. In addition, different plasma treatment parameters (plasma power, treatment durations) were investigated to find the limit of this technique for emission enhancement. I carried out the plasma treatment in our standard RIE machine, which was explained in Section 2.2.

In our experiments, three different gases were used: pure hydrogen, pure argon and a mixture of hydrogen and argon. The ionized hydrogen reacts with the silicon to form Si-H bonds at the surface, and to cause passivation of the surface. It also penetrates the silicon to create defects in the silicon lattice.

In the RIE system, four different parameters can be changed. These are the composition of the gases, RF power, treatment time and the pressure of the chamber. By changing the RF power, we can change the penetration depth of the ions, while by varying the plasma treatment duration, the number of defects created in silicon can be controlled. All plasma treatments were carried out at room temperature.

3.5.1.1 Effect of plasma treatment on the PL of SOI

The details of the effect of different plasma treatment parameters on the PL of SOI and PhC cavity are given below. The chamber pressure was kept constant at 0.1 mbar in all experiments.

(i) Plasma composition

Three different plasma compositions were used. This included pure hydrogen, pure argon and a mixture of hydrogen/argon. Argon ions were added into the plasma to increase the number of defects, as argon is heavier than hydrogen. The PL of SOI in the 1100-1600 nm wavelength range when treated with three different plasma compositions and its comparison with untreated SOI is given in Figure 3.9.

It is noted from Figure 3.9 that there is a pronounced and comparable PL enhancement when the SOI is treated with hydrogen and hydrogen/argon plasma. On

the other hand, there is only a negligible enhancement when only argon is used. This highlights the important role of hydrogen in the emission enhancement process. In fact, hydrogen plays three important roles. These are (i) creation of defects to form midgap defect states, (ii) decoration of defects and (iii) passivation of the surface to reduce non-radiative recombination sites. Since the PL enhancement is observed only when the plasma contains hydrogen, I limited the further investigation to hydrogen-containing plasmas.

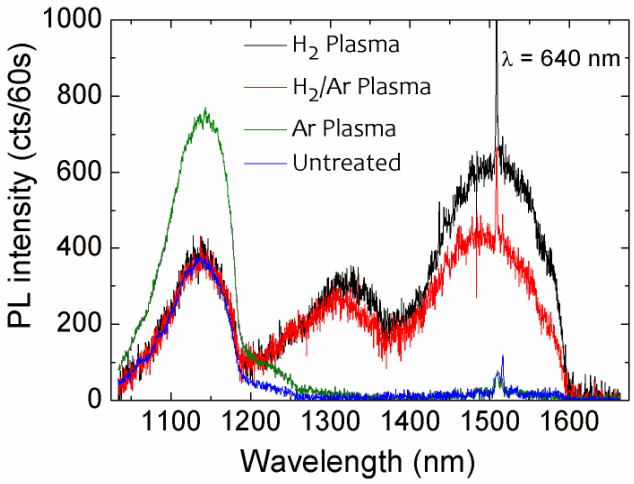

Figure 3.9: PL intensity of SOI when treated with hydrogen, hydrogen/argon and argon plasma. Two sub-bandgap PL bands are created when the plasma contains hydrogen. The band-edge emission by argon plasma treatment is higher because of the increased collection of scattered light. More light is scattered due to the slight sputtering of silicon by the argon plasma.

(ii) Effect of plasma power and treatment duration on the PL of SOI

To investigate the effect of plasma power on the PL of SOI, the plasma power was varied from 20 to 100 watts, while keeping the treatment duration and chamber pressure fixed at 30 minutes and 0.1 mbar, respectively. The PL intensity was integrated over the band centred at 1500 nm. I observed that increasing the hydrogen plasma power enhances the PL up to a certain power level (40 W), after which the PL saturates and a further increase in the plasma power reduces it. The same trend is observed when H_2/Ar plasma is used, but the saturation point occurs at lower power level. In other words, for

harder treatment (higher powers), the emission level stays almost the same when pure hydrogen plasma is used, but it decreases quickly when the plasma contains argon.

A similar trend is observed for different treatment durations. The samples were treated for different durations, while keeping the power fixed at 20 watts and the pressure at 0.1 mbar. The PL increases up to 45 minutes treatment duration for hydrogen plasma. On the other hand, the saturation point for hydrogen/argon plasma already appears after 15 minutes, after which the PL starts to decrease. This is shown in Figure 3.10, where integrated PL intensity over the PL band centred at 1500 nm for different plasma powers, Figure 3.10(a) and treatment durations, Figure 3.10(b) is given.

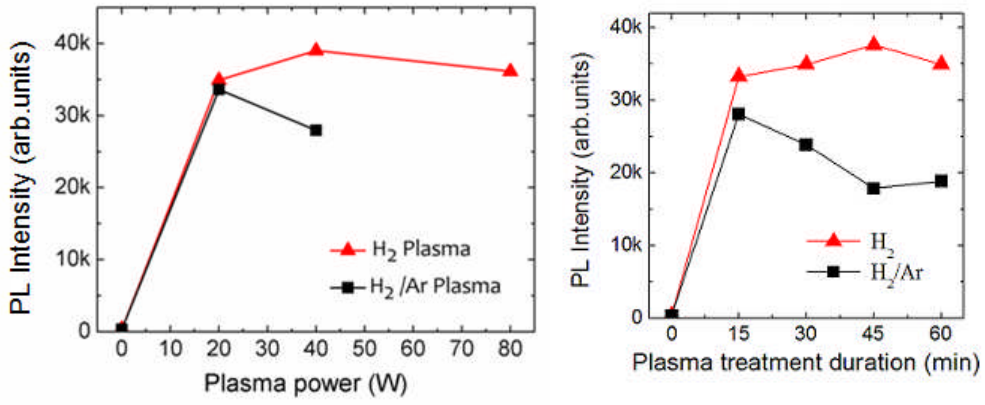

(a) (b)

Figure 3.10: Effect of plasma power and treatment durations on the PL of SOI.

3.5.1.2 Effect of plasma treatment on the PL of the PhC cavity

I carried out the investigation of the effect of plasma power and treatment durations on the PL level of the L3 PhC nanocavity emission line. The same values of plasma power and treatment durations as those for the SOI tests were used. The fundamental emission line of the cavity shows similar behaviour, i.e., an increase of the intensity until certain power levels and treatment durations and then a decrease again on further processing.

Also, in this case, the saturation point for hydrogen plasma comes later than that for hydrogen/argon plasma, as shown in Figure 3.11. It was not possible to treat the membraned PhC cavity by hydrogen/argon plasma for powers higher than 40 watts as these powers tended to collapse the membrane.

These tests show that maximum PL enhancement is achieved at moderate power levels (40 W) and treatment durations (30-45 minutes) and using pure hydrogen plasma is a better choice.

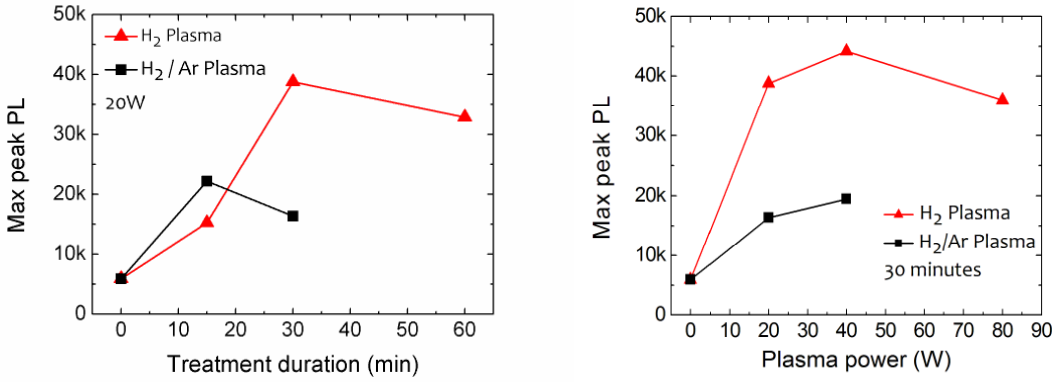

(a) (b)

Figure 3.11: Effect of plasma treatment duration and power on the PL of the fundamental emission line of the L3 PhC nanocavity. The points shown on the curve are the integrated PL over the emission line.

3.5.1.3 Effect of plasma treatment on the cavity Q-factors

To achieve a high PL enhancement due to the Purcell effect, it is necessary to maintain the high Q-factors of the cavity, as discussed in Section 1.5.1. Thus, although the hydrogen or hydrogen/argon plasma treatments provide the enhancement of emission from the silicon material, it is still necessary to investigate its effect on the Q-factors of the PhC nanocavity. For this purpose, the measurements of the Q-factors of the L3 PhC cavity, treated by hydrogen and hydrogen/argon plasma for different plasma powers and treatment durations were carried out by the RS method. Surprisingly, I found out that the Q-factor of the cavity tends to increase with hydrogen plasma treatment. On the other hand, the Q-factors decrease drastically when the plasma contains argon ions. In fact, for pure hydrogen also, the Q-factors increase up to a certain point, after which the surface starts to get rough for higher plasma powers and treatment durations, causing the decrease in Q-values. This is shown in Figure 3.12, where the Q-factors of the PhC cavities treated with different plasma powers and treatment durations and measured by RS method are given.

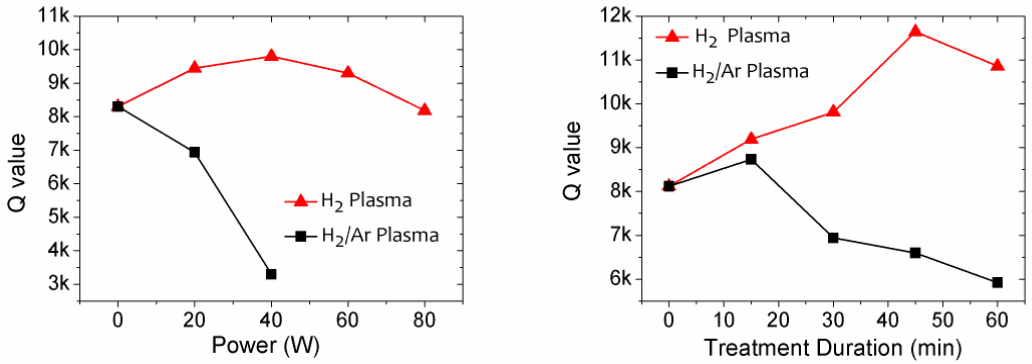

(a) (b)

Figure 3.12: Effect of different plasma powers (a) and treatment durations (b) of hydrogen and hydrogen/argon plasmas on the Q-factors of the L3 PhC cavity. The Q-factor increases with hydrogen plasma treatment while it decreases drastically in hydrogen/argon plasma.

I believe that the increase of the Q-factor is due to some "polishing" effect of the hydrogen plasma treatment. The reactive ion etching of the holes into the silicon slab tends to add roughness. The hydrogen plasma treatment then polishes these side walls, which reduces the scattering losses and in-turn increases the Q-factor of the cavity. On the other hand, the decrease of Q-factors when the plasma contains argon ions is due to the physical damage caused to the silicon. Argon sputters out some silicon material from the top of the holes, making the holes asymmetric, which causes the reduction of Q-factors [11]. The root mean square (*rms*) values of the surface roughness, measured by atomic force microscope (AFM) show that indeed the surface roughness of the etched silicon reduces after hydrogen plasma treatment. The *rms* values of surface roughness for different plasma treatments are summarized in Table 3.2. These values correspond to a scan area of 1x1 μm^2. These values of surface roughness were measured on the SOI surfaces, which underwent an identical plasma treatment as the PhC sample. Similar results are expected for the etched side walls of the PhC holes.

The AFM used for the measurement has an accuracy of 0.2 nm but keeping in view the noise levels in the lab, the accuracy is expected to be no better than 0.5 nm. Thus, the first digit after the decimal is significant only.

Table 3.2 RMS values of surface roughness of SOI treated with different plasma conditions.

Treatment	RMS value of surface roughness (nm)
Etched silicon	1.94993
H_2 Plasma treated, 20 watts, 40 minutes	0.885307
H_2 Plasma treated, 40 watts, 30 minutes	0.885997
H_2/Ar Plasma treated, 20 watts, 30 minutes	1.12062

From this table, it is clear that the roughness reduces following hydrogen plasma treatment. The surface roughness also reduces by H_2/Ar treatment. This shows that the drastic decrease of the Q-factors of the cavities by H_2/Ar plasma treatment is not due to surface roughness but due to asymmetry of the holes. In addition, a close examination of high resolution SEM pictures of the inside walls of the plasma treated PhC holes show the smoothening effect by hydrogen plasma treatment and asymmetry of the holes when treated by hydrogen/argon plasma. These SEM images are shown in Figure 3.13.

The results shown in Figures 3.9 to 3.12 have high level of repeatability. Similar results were obtained from number of identical samples fabricated in different batches during the project. Comparing Figures 3.9, 3.10 and 3.11, we observe that there is not a significant difference in the PL enhancement of SOI when treated with hydrogen or hydrogen/argon plasma. On the other hand, there is a pronounced difference in PL enhancement of cavity peak. This difference is due to the different effect on Q-factors of the cavity by hydrogen and hydrogen/argon plasma. The increase of Q-factors by hydrogen plasma treatment causes more PL enhancement due to the Purcell effect. On the other hand, the decrease of Q-factors by hydrogen/argon plasma reduces the PL enhancement. The sputtering out of the silicon material by heavy argon ions can also be responsible for increasing the non-radiative recombination sites, which also contributes in the reduction of PL enhancement.

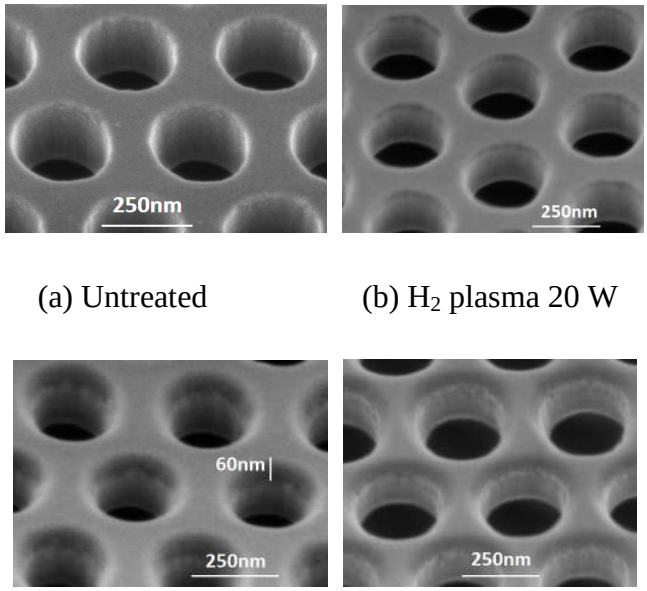

(a) Untreated (b) H_2 plasma 20 W

(c) H_2 plasma 100 W (d) H_2/Ar plasma 20 W

Figure 3.13: High resolution SEM pictures of PhC holes. Untreated (a), treated with hydrogen plasma (b, c) and hydrogen/argon plasma (d). The walls of the holes become smoother compared to the untreated case by hydrogen plasma treatment (b), while it becomes asymmetric by hydrogen/argon plasma treatment (d). The dark shades on top of the holes show the penetration depths of the ions.

The penetration depths of the ions by plasma treatment can also be observed in these SEM pictures, shown by the dark shades on top of the holes. The penetration depth for moderate power, 20 watts, is around 15 nm while the maximum penetration depth, achieved for 100 watts is ≈85 nm. This indicates that, the plasma treatment is only a surface effect and the optically active defects are introduced into the top few tens of nanometers only. For this reason, when plasma treatment is carried out after the fabrication of PhC, the PL enhancement is much higher compared to the case when the plasma treatment is done before the fabrication of PhC. This is because a higher surface area is exposed to the plasma when treatment is done after the fabrication of PhC, introducing more optically active defects into silicon. The difference of PL enhancement when the plasma treatment is done before or after the fabrication of the PhC cavity is shown in Figure 3.14.

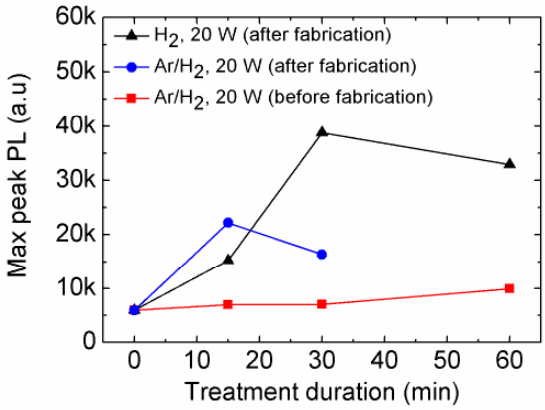

Figure 3.14: Difference of PL enhancements when the plasma treatment is carried out before or after the fabrication of PhC. The PL enhancement is much higher when the treatment is performed after the fabrication of the cavity due to the larger surface exposed to the plasma.

From these experiments, I found out that to obtain maximum PL enhancement, the incorporation of physical defects into silicon is not sufficient and the decoration of these defects by hydrogen is also necessary. Combining all the effects, the most optimized recipe for PL enhancement is to use pure hydrogen at a plasma power of 40 watts, treatment duration of 30 minutes, a chamber pressure of 0.1 mbar and to carry out the treatment after the fabrication of PhC. When applying this optimized treatment to PhC nanocavities, we get up to two orders of magnitude enhancement in the cavity emission peak at room temperature, as shown in Figure 3.15.

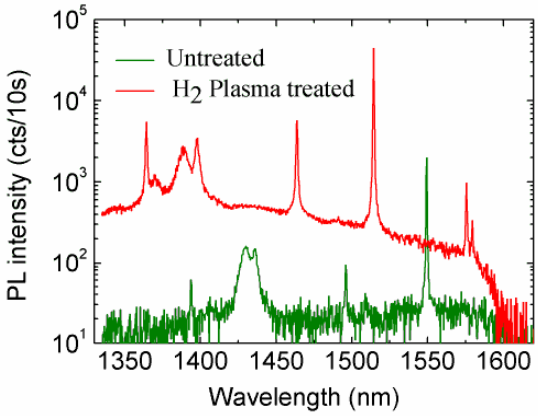

Figure 3.15: Enhancement of PL by up to two orders of magnitude by hydrogen plasma treatment.

3.5.1.4 Recombination mechanism creating broad PL bands

Three different possible mechanisms of carrier recombination at the hydrogen related defects to create luminescence bands are described in detail in Section 1.3.3.2.3. From our experimental results, I believe that the mechanism (iii) is valid in our system. According to this model, both the electron and hole are trapped at the same defect state. Their wave function will have the same k-values and hence momentum conservation would be established. The carriers will undergo direct recombination without assistance of a phonon and there will be no thermal broadening of the emission line. As we do not observe thermal broadening of the emission line, this recombination model is the best explanation of the recombination mechanism that gives rise to the PL bands. At room temperature, although the overall band is broad yet the emission line from individual defects is very narrow as otherwise high value of Purcell factor (10-12) by high Q-cavity would not have been observed, as also discussed in Section 3.3.1. Thus, individual emission lines from the defects stay narrow at room temperature indicating that there is no thermal broadening. Furthermore, the shape of the PL spectra at liquid helium temperature (10 K) remains unchanged. If there was a thermal broadening effect, then narrowing of the band should have been observed at low temperatures, which is not the case, as shown in Figure 3.16.

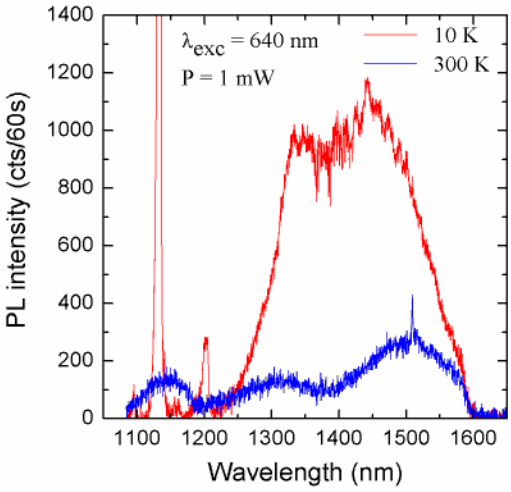

Figure 3.16: The PL level of the emission bands increases by a factor of 5 at low temperature due to reduction in non-radiative recombination, but the shape of the bands remains unchanged.

This indicates that, the overall emission band is an aggregate of many narrow emissions at different wavelengths, with each emission line being thermally stable. At low temperatures, the overall PL level of the band increases by a factor of 5 due to a reduction in non-radiative recombination channels such as Auger and surface recombination.

3.5.1.5 Lifetime measurements of defect emission - Estimation of Purcell factor

In Section 3.3.1, the Purcell factor of the defect luminescence coupled with an L3 PhC nanocavity was estimated to be 10-12 from the emission enhancement factor and by following the geometrical considerations. The more accurate method to measure the Purcell factor is by measuring the reduction of the lifetime of the emission, when on-resonance with the cavity. For this purpose, low temperature time resolved µPL experiments at 10 K were carried out at Pavia by using the setup shown in Figure 3.17.

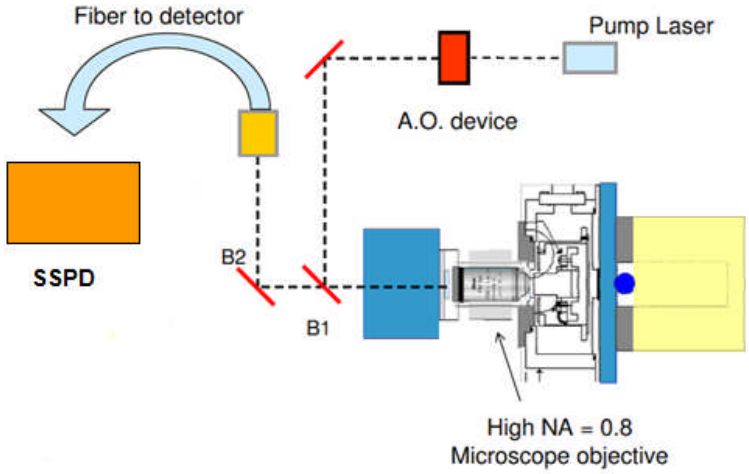

Figure 3.17 Setup to carry out time resolved µPL measurements.

A CW pump laser operating at 640 nm was used whose electrical input signal was modulated by the signal generator having square shaped pulse. The laser switch-off time was 1 ns with repetition rate of 50 ns. The output of the laser can also be modulated by an acousto-optic modulator (A. O. device) or a chopper wheel if low modulation frequency is sufficient. The incident pulsed light was focused on the cavity by an objective and the light emitted from the cavity was collected by the same objective using two beam splitters (B1 and B2). The collected light below 1500 nm wavelength was filtered out and the rest was fed to a liquid He cooled super conducting single

photon detector (SSPD). The correlation between the incident pulse and the detector was established by an electronic board, which counts the number of photons generated after switch-off of the pulse.

The results of the time resolved PL measurements of hydrogen plasma treated SOI, PhC and PhC cavity are shown in Figure 3.18.

From these measurements, it is found out that the PL decay of hydrogen plasma treated SOI and PhC in the 1500-1600 nm wavelength range is composed of three components. This shows that the collected emission from SOI and PhC is due to many transitions having different lifetimes. To extract the lifetime values, the data were fitted with a triple exponential function given as follows, with each exponential corresponding to a single transition,

$$Ae^{\frac{-t}{\tau_1}} + Be^{\frac{-t}{\tau_1}} + Ce^{\frac{-t}{\tau_1}}$$

where A, B and C are fitting coefficients and τ_1, τ_2 and τ_3 correspond to the lifetime values of the three components in the decay curve, corresponding to different transitions.

In the case of SOI, the exponential decay curve consists of 3 parts with lifetimes of 1, 8 and 250 ns, respectively. The fastest component however is limited by the laser switch-off time, which is indicated by the blue squares in Figures 3.18 (b,f). Similarly, the PL decay of hydrogen related defects in PhC (without any cavity) is composed of three components but with comparatively longer lifetime as compared to that in SOI. All of these components also have an exponential decay with lifetime of 6, 100 and 1100 ns, respectively, which is longer than the lifetimes of PL from SOI. The longer lifetime of PL from hydrogen plasma induced defects in PhC is due to the suppression of the emission of photons due to the photonic stop-band of PhC. In the case of the on-resonance emission, the lifetime is very short, limited by the laser switch-off time, which is 1 ns. The off-resonance PL was filtered out using the monochromator, so that only on-resonance cavity PL is collected.

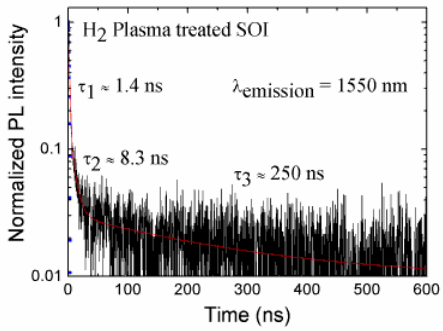

(a)

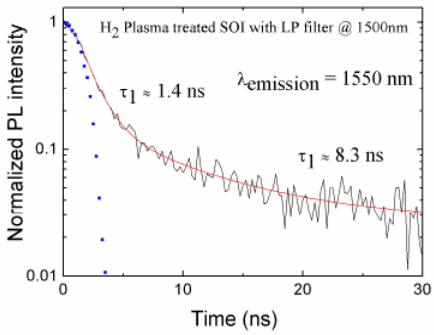

(b)

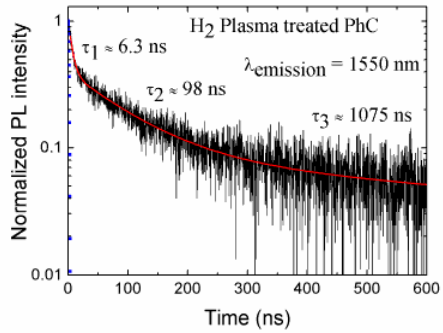

(c)

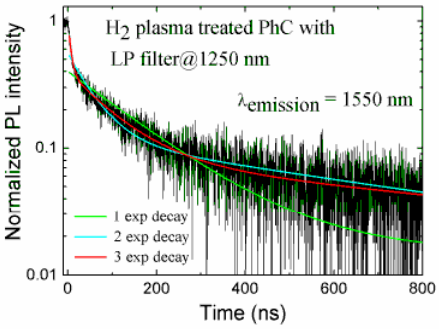

(d)

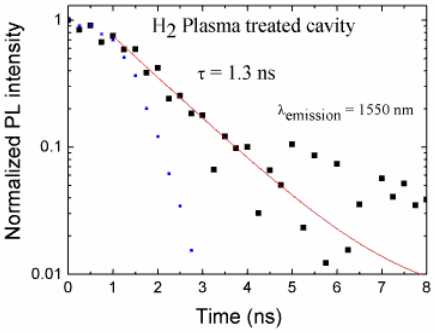

(e)

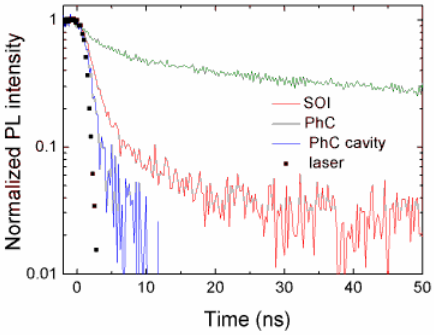

(f)

Figure 3.18: Lifetime measurements of hydrogen plasma induced defect luminescence from SOI (a, b), PhC (c, d) and L3 PhC cavity (e). The comparison of lifetimes for all three cases is given in (f). The lifetime measurement of the cavity is limited by the laser switch-off time, which is 1 ns. Thus, this value can be taken as the upper limit of the lifetime of the defect emission coupled on-resonance with the PhC cavity.

As unfortunately the lifetime measurements were limited by our laser switch-off time, it is not possible to extract the Purcell factor from the lifetime measurements shown in Figure 3.18(f). But from the comparison, there is a clear indication for the presence of the Purcell effect and it is possible to report the upper limit of the lifetime as 1 ns. This is also consistent with the model of defects that trap both electrons and holes.

3.5.2 Enhancement of PL by hydrogen implantation

With the power used for hydrogen plasma treatment (40 watts, -420V DC bias), the ions have the energy to penetrate only 20 nm into the silicon. Thus, optically active defects are created only in the top 10 % of the total volume. Increasing the plasma power further to have greater penetration depth is detrimental for the PL enhancement due to increase in physical damage to the surface, as discussed in Sections 3.5.1.2 and 3.5.1.3. Furthermore, since the PhC nanocavity mode is confined in the center of the slab, the mode overlap with the defect layer is not optimal. To improve the performance of the device by increasing the emission intensity, an increase in the active volume by incorporating much deeper defects is required. Another approach that can be used to incorporate hydrogen related defects into silicon is by hydrogen ion implantation by using an ion implanter. In the ion implanter, the implantation energy (in keV) and the dose (number of ions per cm^2) can be varied to change the penetration depth and the amount of incorporated defects, respectively.

The SOI was implanted with a range of doses (10^{11} to $8x10^{15}$ H/cm^2), keeping the implantation energy fixed at 8 keV (courtesy of Dr Giorgia Franzò, Universiy of Catania). The PL of the implanted samples was taken with the same µPL setup at room temperature. We found out that, without annealing, the PL of the hydrogen implanted SOI is very low compared to the hydrogen plasma treatment for all the doses, as shown in Figure 3.19.

Annealing the hydrogen implanted SOI at 300-350 ^oC in forming gas (10:90 H_2:N_2) activates the incorporated ions and a strong PL band centered at 1300 nm is observed. Further increase in the annealing temperature reduces the PL level due to out-diffusion of hydrogen, as shown in Figure 3.20. Thus, annealing in forming gas is necessary to activate the implanted defects and to observe the enhancement of PL. Furthermore, the PL enhancement is observed only for doses higher than $1e^{15}$ H/cm^2. Lower doses do not induce a sufficient number of defects for observable PL enhancement. Not only for

hydrogen implants, but also for hydrogen plasma treatment, the emission is enhanced by a factor of 5 by forming gas annealing.

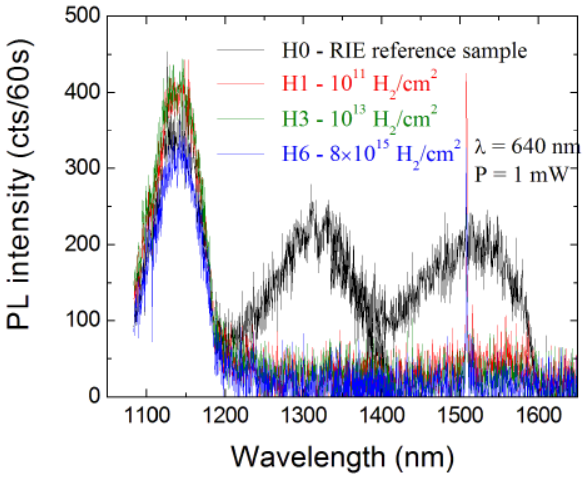

Figure 3.19: PL at room temperature from hydrogen implanted SOI using different implantation doses. The PL is much lower compared to the hydrogen plasma case for the same excitation power (1 mW) when annealing is not done. The spike at 1500 nm is due to the pump laser.

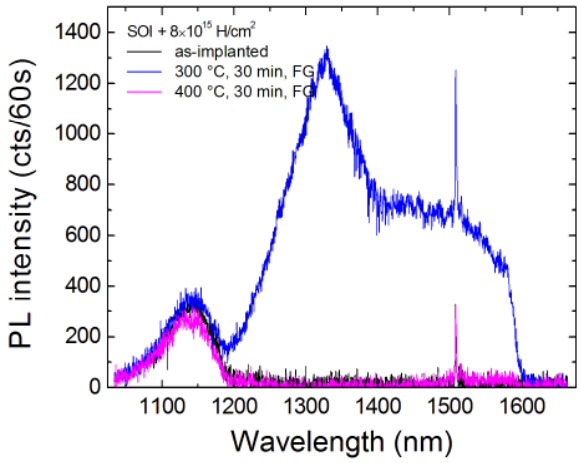

Figure 3.20: Activation of hydrogen implants by forming gas (10:90 H_2:N_2) annealing to increase the PL of SOI.

The enhancement of emission due to forming gas annealing can be attributed to the diffusion of hydrogen and the combination of better passivation and decoration of hydrogen defects. Perhaps, all the defects created by the hydrogen plasma treatment might not have been filled by hydrogen to create Si-H bonds. Annealing in forming gas helps to fill those defects, causing an increase in the emission intensity. Alternatively, the passivation or saturation of dangling bonds can also be the reason for the observed increase in PL. The comparison between emission bands created by hydrogen ion implantation and plasma treatment followed by forming gas annealing is given in Figure 3.21. The hydrogen ion implantation creates one dominant PL band centred at 1300 nm, while hydrogen plasma treatment creates two bands centred at 1300 and 1500 nm. This shows that both treatments induce different types of defects, which give rise to PL bands with different shapes and spectral position.

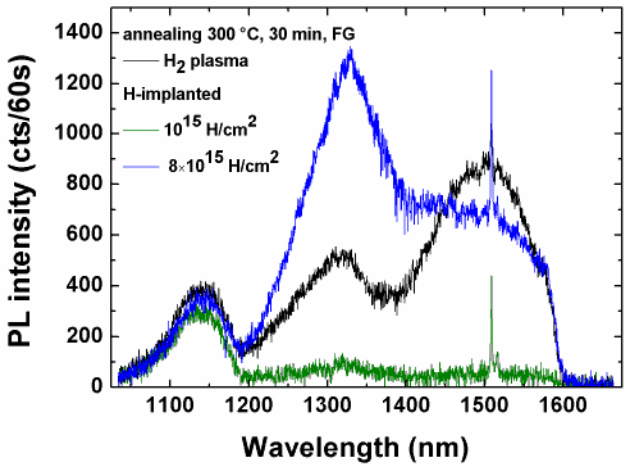

Figure 3.21: Comparison of PL bands created by hydrogen ion implantation and plasma treatment followed by forming gas annealing. The two treatments create bands with different shapes and spectral position. Furthermore, PL enhancement is only observed for doses higher than $1e^{15}$ H/cm^2.

3.6 Nature of defects

To understand the nature of defects, created by hydrogen ion implantation and plasma treatment, transmission electron microscopy (TEM) studies were carried out. To establish the relation between different types of defects and the PL bands, annealing

experiments were performed to study the thermal evolution of defects and their influence on the intensity of PL bands.

3.6.1 Transmission electron microscopy studies

Planar view (PV) and cross section (CS) transmission electron microscopy studies were carried out (TEM images credit to Dr Simona Boninelli, University of Catania). A JEOL JEM 2010 instrument was used at 200 kV. A defocused off-Bragg cross sectional (CS) view of the plasma treated SOI is given in Figure 3.22.

Three different types of defects can be seen in the TEM image of the plasma treated SOI. These defects are situated at different depths from the top surface. Within the first 10 nm, there are nano-bubble-like defects. The size of these defects is only a few nanometers. Their exact nature is unknown, but most likely; they consist of agglomerates of vacancies. These nano-bubbles are indicated by the blue arrow in Figure 3.22.

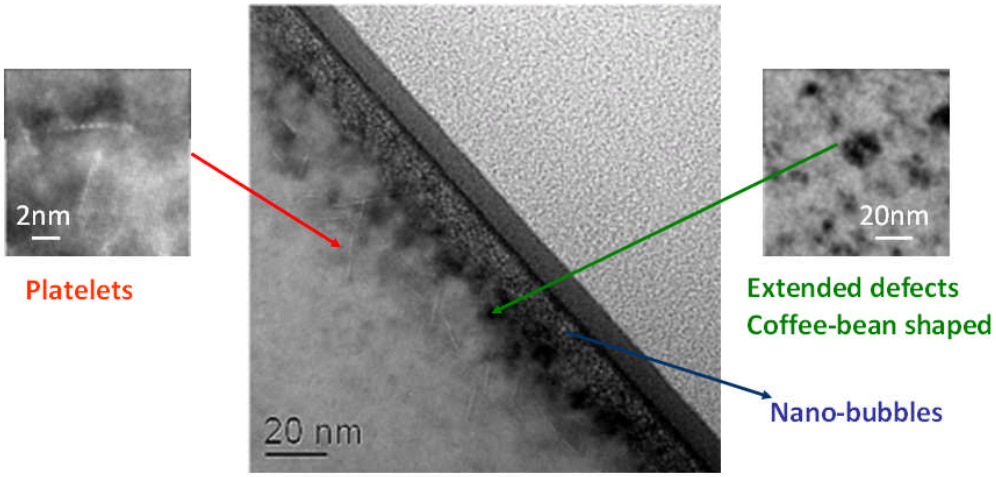

Figure 3.22: Cross section off-Bragg TEM image of hydrogen plasma treated SOI. Three types of defects located at different depths are visible. These defects are nano-bubbles, platelets and coffee-bean shaped dislocation loops.

Below this 10 nm layer, platelets are visible, which are indicated by the red arrow. Plateletes can be understood as line defects or flat disks with a mean diameter of 10-15 nm. They are oriented either in the (100) (parallel to the surface) or the (111) plane. The magnified image of these platelets is shown on the left. The same platelet-type defects due to hydrogen plasma treatment of Cz-Si have already been reported in earlier reports

[12-14]. In addition to these two types of defects, some extended defects are observed, which are located between the area containing nano-bubbles and platelets. These defects appear as dark traces or spots and have a coffee-bean shape. A magnified image of these extended defects that we identified as dislocation loops is shown on the right with the green arrow.

Next, we investigated hydrogen implanted SOI in a similar way. Here, the defects mostly consist of platelets that are located much deeper. The platelets are concentrated in the 65 nm wide area at a depth of 80 nm below the surface, which reflects the nature of the ion implantation process. The hydrogen implantation was carried out at 8 keV energy with a dose of $8e^{15}$ H/cm^2. The implantation was followed by forming gas annealing at 350^oC for 30 minutes to activate the defects. The defects created by hydrogen ion implantation are shown in Figure 3.23.

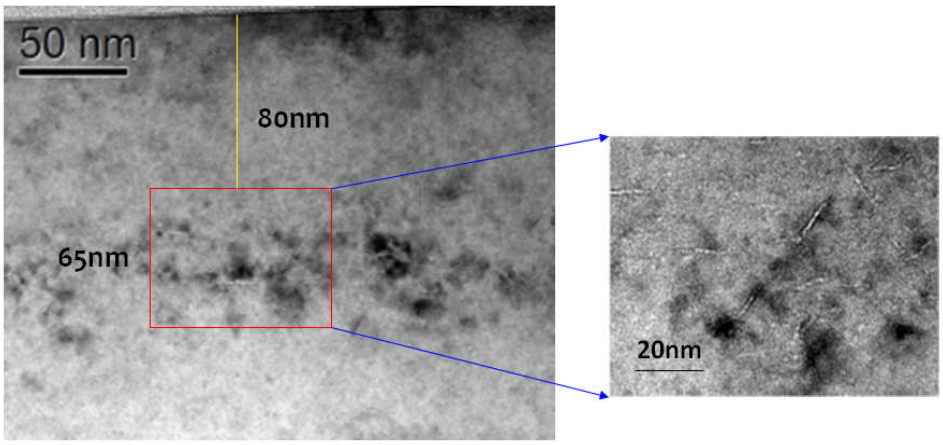

Figure 3.23: Platelets in SOI created by hydrogen ion implantation at a depth of 80 nm.

This TEM analysis indicates that hydrogen plasma treatment creates three different types of defects (nano-bubbles, platelets and dislocation loops), while hydrogen ion implantation creates mostly the platelets only. Relating the PL spectra of hydrogen plasma treated and ion implanted SOI with the defects observed in the TEM analysis, the nature of the defects responsible for generating different luminescence bands can be identified.

The PL spectra of hydrogen implanted SOI have a different profile compared to that of plasma treated samples. In the implantation case, there is only one dominant

emission band centered at 1300 nm. For the plasma treatment, we identify two bands centered at 1300 nm and 1500 nm. As shown by TEM analysis in Figures 3.22 and 3.23 only platelets are created by implantation while two other types of defects (nano-bubbles and dislocation loops) are also present for the plasma treatment. This indicates that the 1300 nm band arises due to platelets, while the 1500 nm band is either due to nano-bubbles or dislocation loops, as indicated in Figure 3.24. The dislocation loops are well known in the literature [15,16] and their emission linewidth is usually smaller than the PL bands observed in our experiments. Thus, the 1500 nm PL band is most probably not due to the coffee-bean shaped dislocation loops.

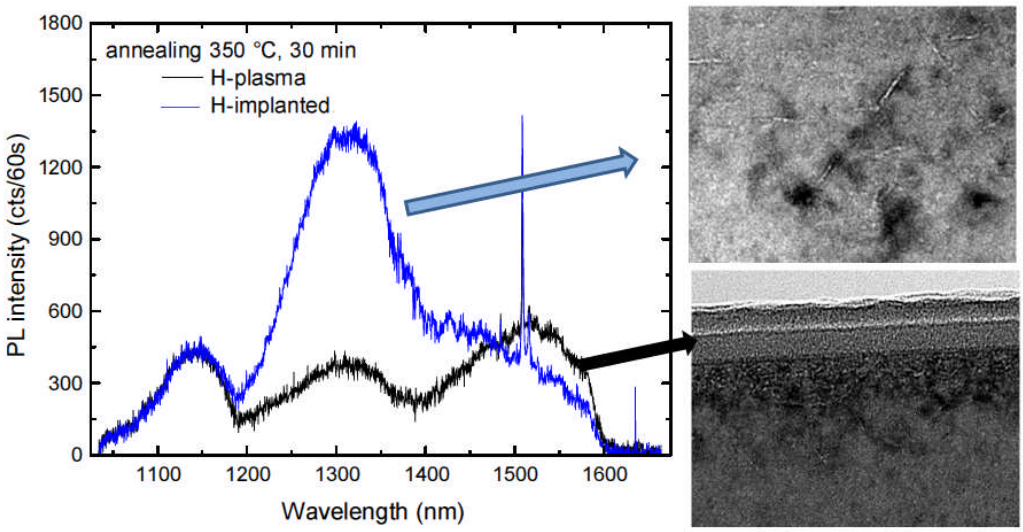

Figure 3.24: Relation of PL bands from hydrogen implanted (blue) and hydrogen plasma treated (black curve) with types of defects.

3.6.2 Thermal evolution of defects

The nature of defects responsible for creating different PL bands was further confirmed by the study of thermal evolution of defects and its effect on the PL spectra.

The hydrogen plasma treated SOI was annealed in forming gas at 350 ^{o}C and higher temperatures (400 ^{o}C and 500 ^{o}C) and its effect on the defects and PL spectra was investigated. It was found out that all the defects survive the annealing temperature of 350 ^{o}C. At higher temperatures, however, the platelets disappear completely. On the other hand, although the amount of nano-bubbles also reduces some nano-bubbles

survive the annealing at higher temperatures, as shown in Figure 3.25. The PL spectra of the annealed samples show the increase in the PL level up to an annealing temperature of 350 ^{o}C, after which the PL level drops. Above 400 ^{o}C, the temperature at which the platelets disappear, the PL band centered at 1300 nm is totally quenched.

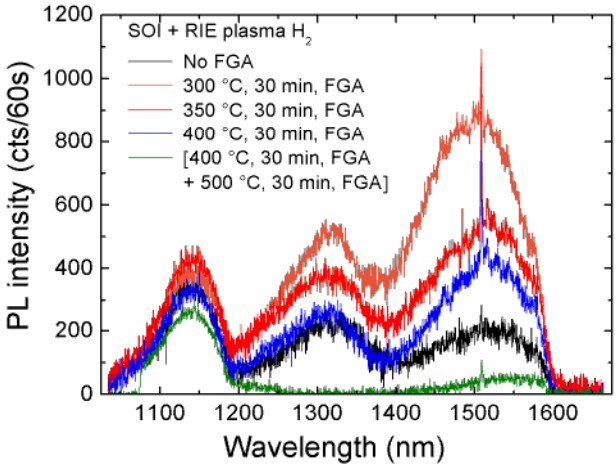

(a)

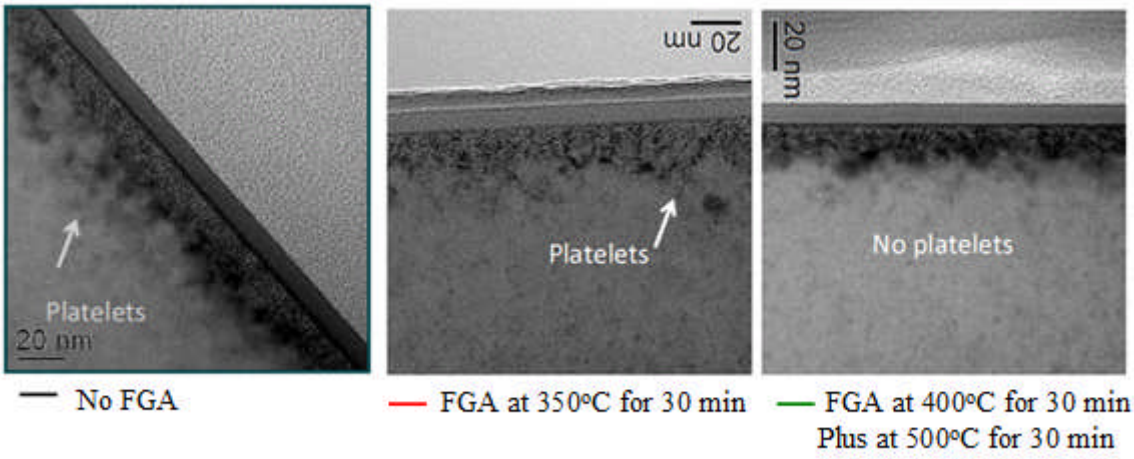

(b)

Figure 3.25: (a) Effect of forming gas annealing on the PL level. The maximum PL level is achieved by annealing at 300 ^{o}C. At higher temperatures, the PL starts to decrease again. The 1300 nm band is completely quenched while some level of 1500 nm band is maintained by annealing at 400^{o}C for 30 minutes plus 500 ^{o}C for 30 minutes. (b) The corresponding TEM images.

On the other hand, the PL level of 1500 nm band drops significantly as well but some level of luminescence is still maintained. This further shows that the PL band at 1500 nm is related to nano-bubbles, while 1300 nm band arises due to platelets.

In the case of hydrogen implanted SOI, annealing above 400 ^{o}C also completely quenches the 1300 nm PL band. Since there were no nano-bubbles created by hydrogen implantations, the 1500 nm band is completely absent, as shown in Figure 3.26.

From these observations, it can be concluded that the 1500 nm band is due to radiative recombination at nano-bubbles, while the 1300nm band arises from the radiative recombination at platelets.

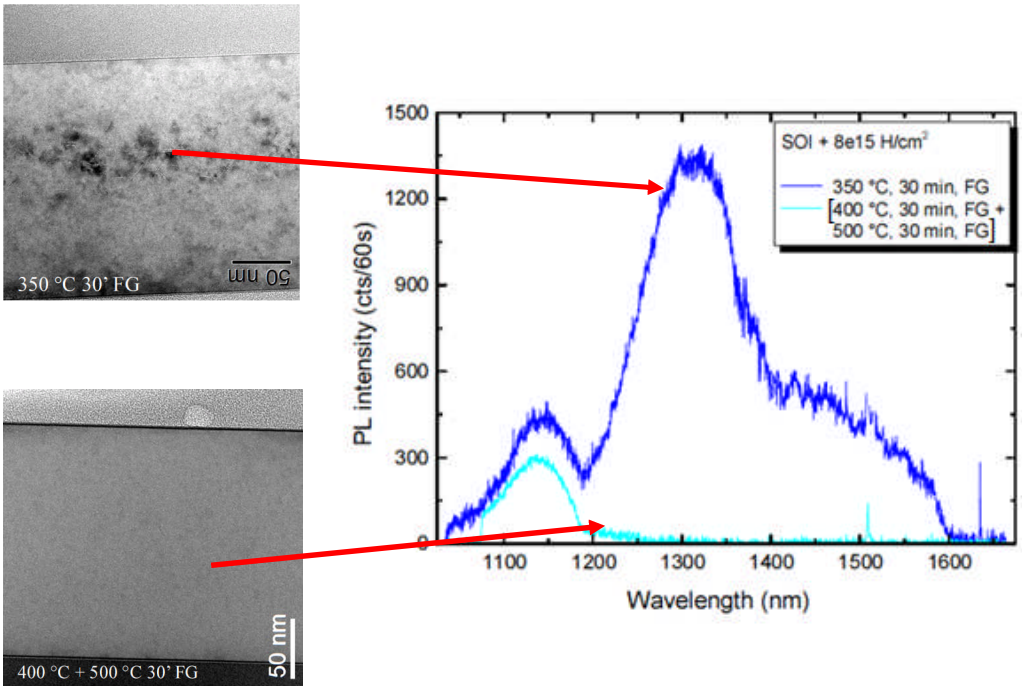

Figure 3.26: TEM images showing the effect of forming gas annealing on the defects and its effect on the PL intensity of hydrogen implanted SOI. The PL is completely quenched on annealing above 400 ^{o}C due to removal of all platelets.

3.6.3 TEM microscopy of treated PhC

Taking a planar view TEM image of hydrogen plasma treated PhC shows that the defect concentration increases at the side walls of the holes, as shown in Figure 3.27(a). Furthermore, the same level of defects is created along all the directions of PhC holes,

which extend to the bottom of the PhC as depicted in Figure 3.27(b). Thus, the plasma treatment is an isotropic process, which allows the formation of defects also close to the vertical surface of the holes. On the other hand, the defects are not created isotropically in the H-implanted PhC, as shown in Figure 3.27(c).

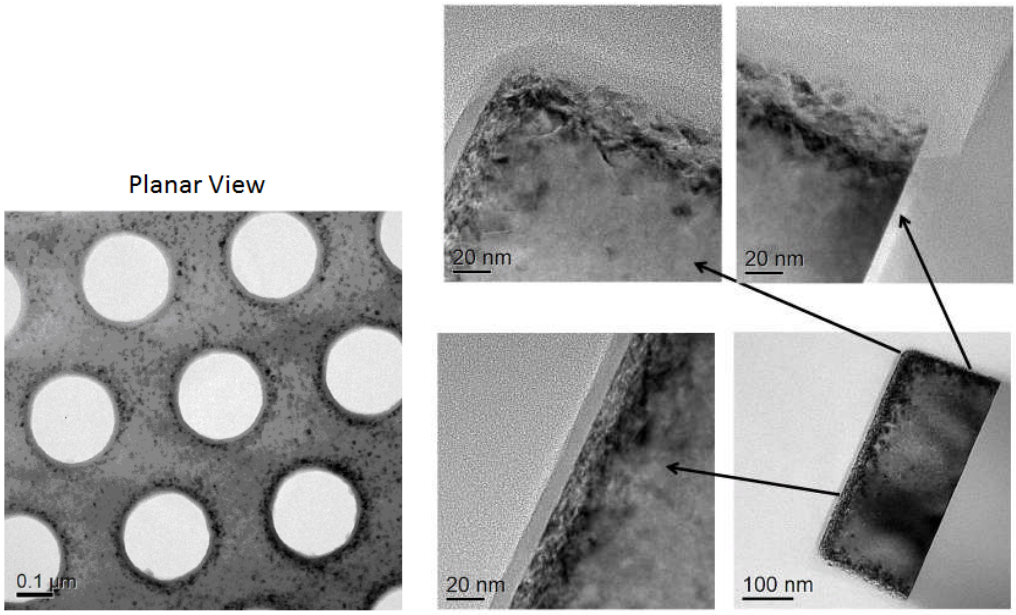

(a) (b)

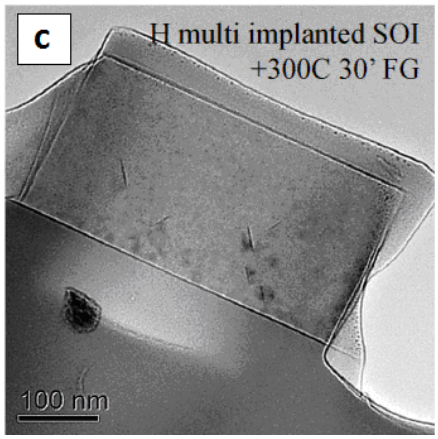

(c)

Figure 3.27: (a) Planar view TEM image showing that the defect concentration increases along the side walls of the PhC by hydrogen plasma treatment. (b) The damage by hydrogen plasma treatment is same along all directions of PhC holes and extends to the bottom of the PhC. (c) TEM image of hydrogen implanted PhC.

3.7 Multiple depth H-implantation

As shown in Figure 3.23, the defect layer is concentrated only in the 65 nm wide area at the depth of 80 nm from the top surface. Thus, even with hydrogen implantation the whole volume of the top silicon layer of SOI is not utilized. The emission level could be further increased if the defects were introduced in the whole volume of the top silicon layer. For this purpose, hydrogen implantation was carried out in 3 steps with different implantation energies. The implantation energies of 8 keV, 10 keV and 15 keV were used, which covers the whole 220 nm slab, as shown in the simulation of depth vs. hydrogen ion concentration in Figure 3.28. This Monte Carlo simulation was carried out by a software called "SRIM" (Stopping Range of Ions in Matter) (courtesy of Dr Giorgia Franzò, University of Catania).

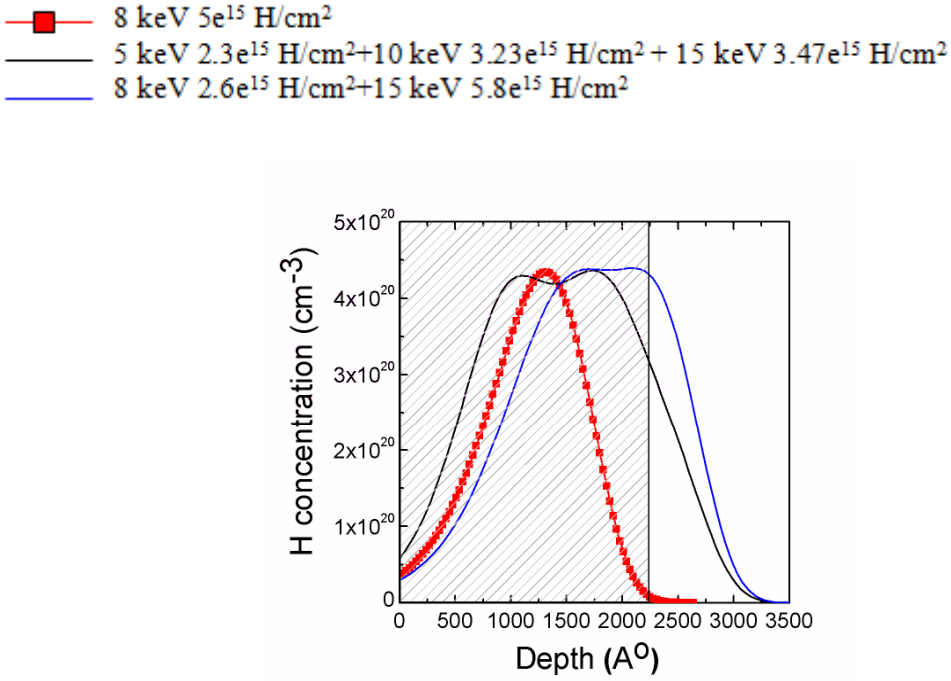

Figure 3.28: Simulation of hydrogen concentration at different depths by using different implantation energies.

The TEM analysis of the multiple depth implanted sample shows that the defects cover more volume compared to the single depth case. The corresponding PL measurements reveal that indeed, the intensity of 1300 nm band increases due to increase of amount of defects by multiple depth implantations, as shown in Figure 3.29.

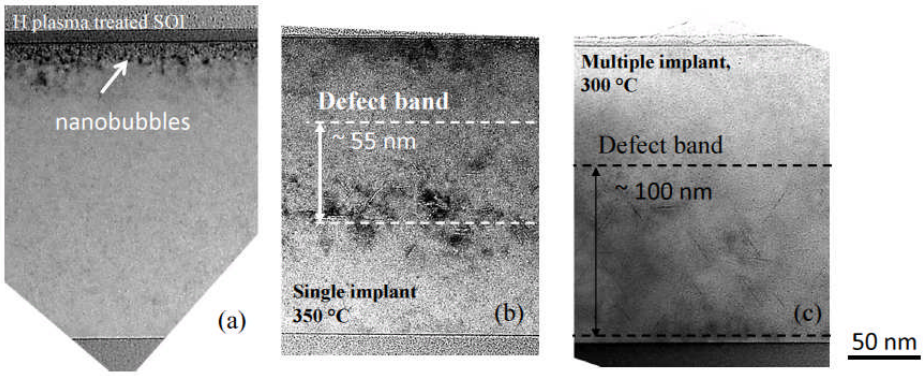

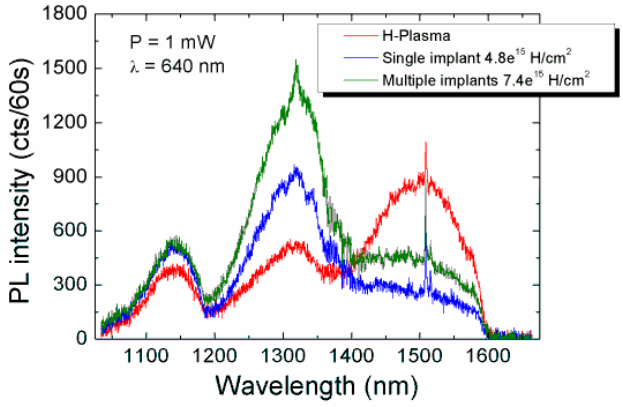

(d)

Figure 3.29: Comparison of the PL level of single and multiple H-implanted SOI with plasma treated SOI (d). The PL level of 1300 nm band increases with multiple implants as the defect volume increases. The corresponding TEM images are also shown (a-c).

Unfortunately, even though the 1300 nm PL band has a higher emission level when multiple implantations are done, the PL of the cavity is still lower compared to the hydrogen plasma treated cavity. The comparison is shown in Figure 3.30.

There can be two possible reasons for the lower PL level of the H-implanted cavity compared to the H-plasma treated cavity. Firstly, the hydrogen plasma passivates the etched side walls of the PhC holes to reduce the non-radiative recombination sites. This passivation mechanism is missing for H-implanted PhC. Secondly, the hydrogen plasma treatment is isotropic, creating defects everywhere, also close to the vertical side walls of the PhC, as shown in Figure 3.27(a). With multiple H-implantations, even though the

defects are created in the entire volume, there are a smaller number of defects along the vertical side walls as H-implantation is not isotropic. This is shown in the TEM image of H-implanted PhC in Figure 3.27(c). These two factors are responsible for lower PL of H-implanted cavity compared to the H-plasma treated cavity.

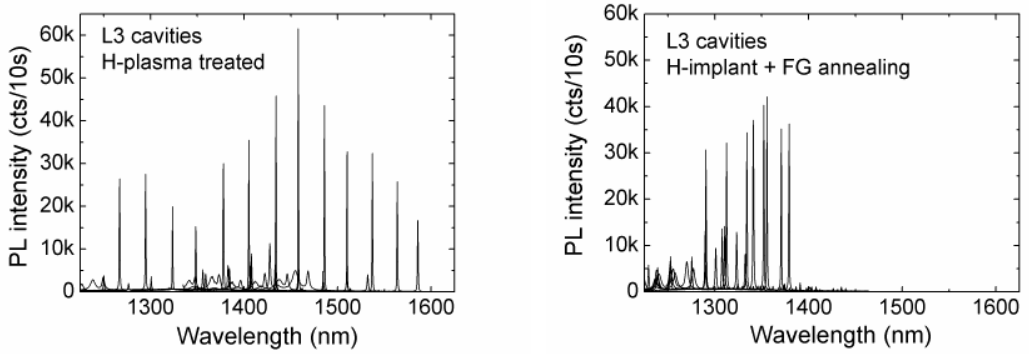

(a) (b)

Figure 3.30: Comparison of the PL level of the H-plasma treated (a) and multiple depths H-implanted PhC cavity (b). The emission level of H-implanted cavity is lower even though the background 1300 nm PL band is higher. The results shown for H-plasma treated cavities are without forming gas annealing, which would increase the PL level even further by a factor of 5.

3.8 Optically pumped all-silicon nanolight source

Applying the best recipe developed in this chapter (pure hydrogen plasma, 40 watts plasma power, 0.1 mbar chamber pressure and treatment duration 30 minutes), an enhancement of up to two orders of magnitude in PL is obtained. A further 5 times enhancement is achieved by forming gas annealing. Thus, we achieve up to 500 times enhancement relative to the untreated SOI at the same wavelength. The emission is enhanced a further 300 times by using the PhC nanocavity, which gives a narrow emission line (<0.5 nm) with an emission level 150,000 times higher than the bulk silicon at sub-bandgap wavelengths. Following these treatments, not only the cavity peak but even the broadband background emission from SOI surface is higher than the band-edge emission of silicon as shown in Figure 3.31.

Thus, by a combination of material processing and device engineering, we obtain an optically pumped narrow emission line (<0.5 nm), all-silicon nanolight source. This silicon light source emits at sub-bandgap wavelengths and operates at room

temperature. The power spectral density of the device, expressed in pW/nm, is given in Figure 3.31. The power spectral density of the fundamental emission line is 8 pW/nm, which is the highest value reported from any silicon emitter to date, even without restricting it to the room temperature operation. An IR image, showing the light emission from the PhC cavity, is also given in Figure 3.31. This image was taken by an IR camera with a low pass filter with a cut-off at 1500 nm.

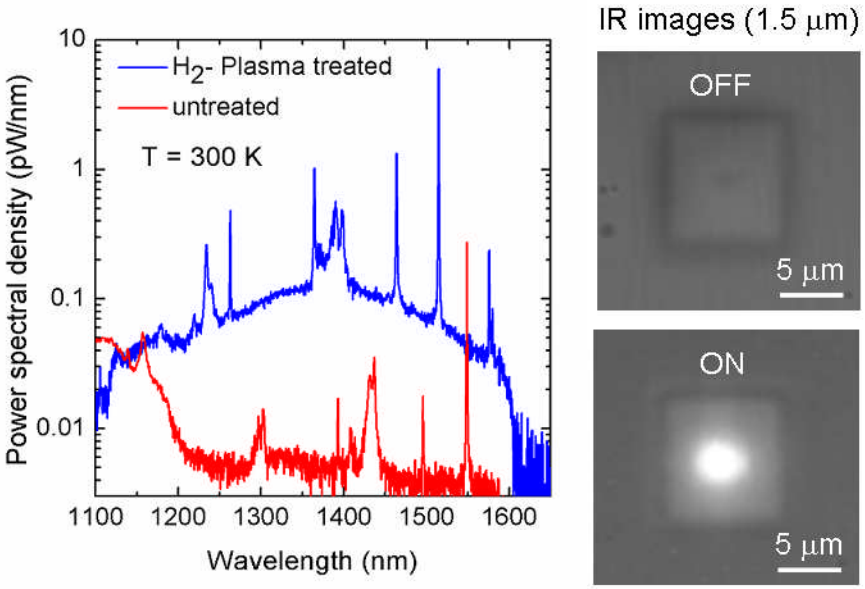

(a) (b)

Figure 3.31: Optically pumped silicon PhC nanocavity light source. The PL spectra is shown in (a). The fundamental emission line of the device is at 1520 nm with a power spectral density of 8 pW/nm at room temperature. (b) The filtered IR image of the device, showing the emission of light when cavity is pumped optically.

3.8.1 Tunability

The fundamental emission line of the silicon PhC nanocavity light source is shown to be at 1520 nm in Figure 3.31. Since the luminescence band generated by hydrogen plasma treatment covers the entire telecommunication band, the emission line of this device can easily be tuned accordingly, i.e. in the full 1300-1600 nm band.

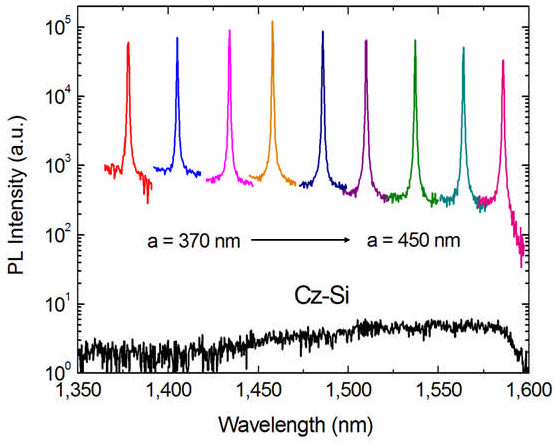

Figure 3.32: Emission line is tuned through 1300-1600 nm by changing the lattice period of PhC. The emission level of these lines is 40,000 times higher than the emission from Cz-Si at same (sub-bandgap) wavelengths [17] [4].

This tunability can be achieved by changing the lattice period of the PhC. By changing the lattice period, the fundamental resonance wavelength of the cavity and hence the emission line will be changed. This is shown in Figure 3.32, where the fundamental emission line of cavities, with different lattice periods is shown, compared to the emission from Cz-Si. We observe more than 4 orders of magnitude enhancement in total. Please note that the results shown in Figure 3.32 are without forming gas annealing, which would improve the emission by a further factor of 5, bringing the total enhancement to 5 orders of magnitude.

3.10 Conclusions

The sub-bandgap emission from silicon can be enhanced by introduction of optically active defects into the silicon lattice, which can be further enhanced by the Purcell effect. Two methods were successfully used to induce defects: the hydrogen plasma treatment in the reactive ion etching and hydrogen ion implantation. The hydrogen plasma gives rise to two broad PL bands, centered around 1500 and 1300 nm, while ion implantation only creates one dominant band centered at 1300 nm. From the TEM and annealing studies, I conclude that, the 1500 nm band arises due to the creation of nano-bubbles, while platelets are responsible for the 1300 nm band. The emission level of these bands is enhanced by coupling them with a PhC L3 cavity by gaining an

advantage of the Purcell effect. A high Purcell factor of 10-12 is achieved, which indicates that although the overall PL bands are broad the emission from individual defects is very narrow. The broad PL band is due to the aggregate of many inhomogeneously broadened narrow emission lines. Higher Purcell enhancement is achieved for hydrogen plasma treated cavities compared to the implanted ones due to isotropic creation of the defects by plasma treatment. For this reason, hydrogen plasma treatment is concluded to be a better approach for silicon PhC cavity emission enhancement compared to ion implantation approach. By a combination of hydrogen plasma treatment and the Purcell effect, an overall emission enhancement factor of 150,000 or 5 orders of magnitude compared to as-bought Si material is achieved. Utilizing this emission enhancement, an optically pumped silicon nanolight source is demonstrated at room temperature. This light source has a narrow (<0.5 nm) tunable emission line in the 1300-1600 nm wavelength range. The collected power of this device is 4 picowatts with power spectral density of 8 pW/nm, the highest ever reported from a Si light source reported to date, even without restriction to room temperature and sub-bandgap operation. The work carried out in this chapter is a step forward in developing an electrically pumped all-silicon nanolight source, which is presented in Chapter 4. The developed light source can be used for practical applications. One such application is refractive index sensing, which is presented in Chapter 5.

References

[1] A. Shakoor, R. Lo Savio, S. L. Portalupi, D. Gerace, L. C. Andreani, M. Galli, T. F. Krauss, and L. O'Faolain, "Enhancement of room temperature sub-bandgap light emission from silicon photonic crystal nanocavity by Purcell effect," Physica B 407, 4027–4031 (2012).

[1]Reprinted with permission. Copyright (2012) Elsevier.

[2] L. C. Andreani and D. Gerace, "Photonic-crystal slabs with a triangular lattice of triangular holes investigated using a guided-mode expansion method," Phys. Rev. B 73, 235114 (2006).

[3] R. Lo Savio, S. L. Portalupi, D. Gerace, A. Shakoor, T. F. Krauss, L. O'Faolain, L. C. Andreani, and M. Galli, "Room-temperature emission at telecom wavelengths from silicon photonic crystal nanocavities," Appl. Phys. Lett. 98, 201106 (2011).

[3]Reprinted with permission. Copyright [2011], American Institute of Physics.

[4] S. G. Cloutier, P. A. Kossyrev, and J. Xu, "Optical gain and stimulated emission in periodic nanopatterned crystalline silicon", Nat. Materials 4, 887 (2005).

[5] J. Bao, M. Tabbal, T. Kim, S. Charnvanichborikarn, J. S. Williams, M. J. Aziz, and F. Capasso, "Point defect engineered Si sub-bandgap light-emitting diode," Opt. Express 15, 6727-6733 (2007).

[6] T. Tanabe, M. Notomi, S. Mitsugi, A. Shinya, and E. Kuramochi, "All-optical switches on a silicon chip realized using photonic crystal nanocavities," Appl. Phys. Lett. 87, 151112 (2005).

[7] P. Barclay, K. Srinivasan, and O. Painter, "Nonlinear response of silicon photonic crystal microresonators excited via an integrated waveguide and fiber taper," Opt. Express 13, 801-820 (2005).

[8] N. Hauke, T. Zabel, K. Müller, M. Kaniber, A. Laucht, D. Bougeard, G. Abstreiter, J. J. Finley and Y. Arakawa, "Enhanced photoluminescence emission from two-dimensional silicon photonic crystal nanocavities," New J. Phys. 12, 053005 (2010).

[2]Reprinted by permission from IOP Publishing Ltd: [New Journal of Physics] (doi:10.1088/1367-2630/12/5/053005), copyright (2010).

[9] J. Weber, "Defect generation during plasma treatment of semiconductors," Physica B 170, 201-217 (1991).

[10] A. Henry, B. Monemar, J. Lindstrom, T. D. Bestwick, and G. S. Oehrlein, “Photoluminescence characterization of plasma exposed silicon surfaces,” J. Appl. Phys. 70, 5597 (1991).

[11] Y. Tanaka, T. Asano, Y. Akahane, Bong-Shik Song, and S. Noda, “Theoretical investigation of a two-dimensional photonic crystal slab with truncated cone air holes”, Appl. Phys. Lett. 82, 1661 (2003).

[12] N. Johnsonn, F. A. Ponce, R. Street, and R. Nemanich, “Defects in single-crystal silicon induced by hydrogenation,” Phys. Rev. B 35, 4166-4169 (1987).

[13] C. Ghica, L. C. Nistor, S. Vizireanu and G. J Dinescu, “Annealing of hydrogen-induced defects in RF-plasma-treated Si wafers: ex situ and in situ transmission electron microscopy studies,” J. Phys. D: Appl. Phys. 44, 295401 (2011).

[14] H. Nordmark, R. Holmestad, J. C. Walmsley, and A. J Ulyashin, “Transmission electron microscopy study of hydrogen defect formation at extended defects in hydrogen plasma treated multicrystalline silicon,” J. Appl. Phys. 105, 033506 (2009).

[15] Wai Lek Ng, M. A. Lourenço, R. M. Gwilliam, S. Ledain, G. Shao, and K. P. Homewood, “An efficient room-temperature silicon-based light-emitting diode,” Nature 410, 192–194 (2001).

[16] N. A. Drozdov, A. A. Patrin, and V. D. Tkachev, “Recombination radiation on dislocations in silicon,” Pisma Zh. Eksp. Teor. Fiz. 23, 651-653, Sov. Phys. JETP Lett. 23, 597-599 (1976).

[17] A. Shakoor, R. Lo Savio, P. Cardile, S. L. Portalupi, D. Gerace, K. Welna, S. Boninelli, G. Franzò, F. Priolo, T. F. Krauss, M. Galli, and L. O'Faolain, “Room temperature all-silicon photonic crystal nanocavity light emitting diode at sub-bandgap wavelengths”, Laser Photonics Rev. 7 , 114-121 (2013).

Chapter 4

Room temperature all-silicon photonic crystal nanocavity light emitting diode

In Chapter 3, I discussed a technique to increase the sub-bandgap emission from silicon by creating midgap defect states. These defect states were created by either hydrogen plasma treatment or hydrogen ion implantation. The enhanced emission from the silicon material was then coupled to a silicon PhC nanocavity operating at telecommunication wavelengths. This gives a narrow emission line at room temperature [1-3]. By using this approach of combining the emission enhancement by material processing (hydrogen plasma treatment) and device engineering (Purcell effect due to PhC cavity), I demonstrated an optically pumped silicon nanolight source [1-3]. This light source has many attractive features such as sub-bandgap emission, room temperature operation, narrow emission line, tunability and nanometer size. Although this light source already has many of these useful features required for practical applications, it would be more useful if it could be pumped electrically [3].

In this chapter, we extend the operation of the device to electrical pumping. The carriers are injected externally by creating *pin* junctions around the cavity, similar to [4-5] and the injected carriers recombine radiatively at the optically active defects in the cavity area. An SEM image/schematic of the device is shown in Figure 4.1.

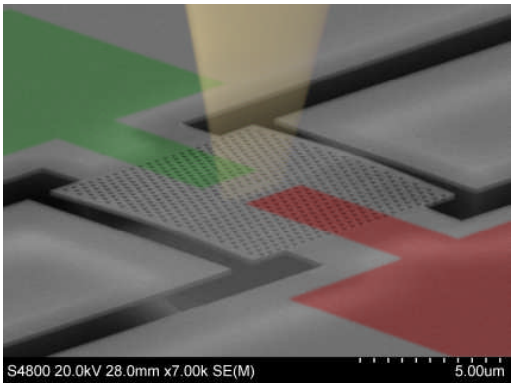

Figure 4.1: SEM picture of the electrically pumped silicon PhC nanocavity light emitting diode. The current is injected by creating a *pin* junction around the cavity. The *p* and *n* doped regions are shown in red and green. Light is emitted vertically with a Gaussian profile by recombination of injected carriers at the defects in the cavity area [3][1]. Artwork courtesy of Dr Christopher Reardon, St Andrews University.

4.1 Fabrication of the device

The creation of a *pin* junction around the cavity involves three lithography and two ion implantation steps, which is feasible with standard technology as PhC fabrication is fully compatible with ultra large scale integration (ULSI) processes [6]. It also involves creating metal contacts and membraning of the PhC. The schematic of fabrication steps is given in Figure 4.2. The stepwise details of the fabrication process are discussed below.

Step 1-4: First e-beam lithography for making alignment marks, PhC cavity and trenches

In the first e-beam lithography step, the alignment marks, PhC cavity and trenches around the PhC were made. The alignment marks were required to align the structures of the second and third e-beam steps with the first ones. The trenches were etched to have a preferential flow of the current through the cavity. In this way, the leakage of the current to the area outside the PhC is reduced. The e-beam resist, e-beam exposure and etching processes are the same as described in Chapter 2. The resist was removed after etching of all the structures into the sample. The PhC cavity and the isolating trenches fabricated in this step are shown in Figure 4.3.

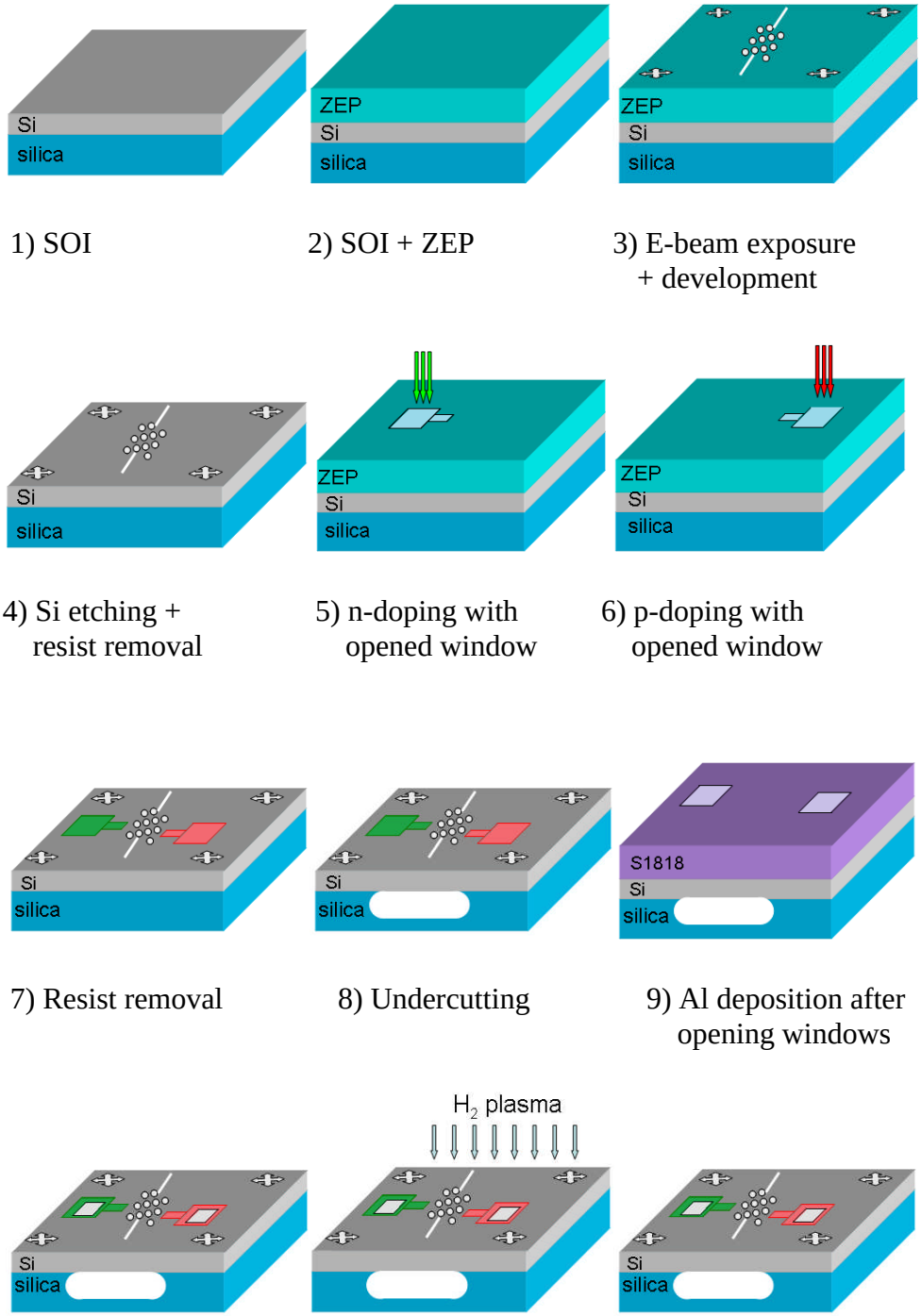

Fig 4.2: Schematic of fabrication steps.

Steps 5-7: Second and third e-beam lithography for opening the windows for ion implantation

The second and third e-beam lithography steps were required to open the windows for the p and n-type doping. Individual e-beam exposure steps are required for opening the windows for each p and n doping. Alignment marks were used to align the exposure area for opening the windows.

Following e-beam exposure and development of the exposed resist, the boron and phosphorous ion implantations for p and n doping, respectively, were carried out by a 400 keV high voltage engineering (HVEE) ion implanter at the University of Catania. The doping levels of both p and n doped areas were $10^{19}/cm^2$. The ion implantation was followed by a rapid thermal annealing step (RTA) at 1000 ^oC for 30 s in a nitrogen environment. The RTA has the dual role of repairing the defects introduced during ion implantation and activating the doped ions.

The doped regions were extended very close to the cavity by a finger-like extension, similar to [4] and shown in Figures 4.1 and 4.3 by the green and red colour. The extended fingers were aligned very carefully by e-beam lithography and separated by a distance of 0.5 µm. This small area between the doped fingers surrounds the PhC cavity and forms the intrinsic region. In fact, this area is not completely intrinsic but has some level of background p doping ($10^{15}/cm^2$). The background doping helps to reduce the resistance and hence improve the electrical properties. Usually, doping damages the optical properties due to an increase of absorption losses but improves the electrical properties by the reduction of resistance. Thus, there is a trade-off between good electrical and good optical properties. For PhC cavities, a Q-factor of 40k has already been demonstrated for the background doping of 10^{18} B/cm^3 [7]. This shows that a slight background doping density is useful to improve the electrical properties without compromising the optical properties. For this reason, it is safe to use SOI material with a background doping density of 10^{15} B/cm^3. The area between the doped fingers, surrounding the cavity, then forms the intrinsic region of the *pin* diode. This region is populated by carriers on injection of current and they recombine in this area due to the low resistivity of the doped fingers. The e-beam resist was removed after each ion implantation step.

Step 8: Undercutting of the PhC nanocavity

Step 8 involves the undercutting of the PhC cavity by removal of the silica layer beneath it. A mixture of HF acid: DI water (1:5) was used for 20 minutes to create an undercut of about 1.5 µm. Before putting the sample into the HF solution, a layer of S1818 resist was spun onto the sample and windows were opened around the PhC cavity by UV exposure and development. In this way, the undercutting takes place only beneath the PhC. The resist was removed after the undercutting process. The undercutting of the PhC to form an air-bridge type suspended structure can be seen in Figure 4.1.

Steps 9-10: Creating metal contacts

This step is carried out to create aluminium metal contacts on the doped areas for the injection of current. A lift-off resist (LOR), followed by S1818 photoresist, was spun on the sample. The windows for metal deposition were opened by UV exposure of S1818 resist. Before the aluminium deposition, the sample was dipped shortly (30 seconds to 1 minute) in HF to remove any layer of native oxide. This helps the adhesion of the metal on the doped silicon. An aluminium layer of 200 nm was then deposited by thermal evaporation. The metal deposition was followed by a lift-off process by the removal of S1818 layer using acetone. The S1818 resist is used for the lift-off process, while the purpose of LOR is only to create an undercut in the S1818 photoresist layer to facilitate the lift-off process. After removal of the resists, the sample was baked at 500 ^{o}C in N_2 environment in a tube furnace. This annealing is necessary to diffuse the aluminium into the silicon to create good metal contacts. The final form of the metal contacts is shown in Figure 4.3.

Step 11: Creating optically active defects by hydrogen plasma treatment

The last and final step was to create the optically active defects in the cavity area by hydrogen plasma treatment. The optimized recipe to obtain highest PL and Q-values discussed in Chapter 3 was used, i.e., using pure hydrogen plasma with 40 W power and 30 minutes treatment duration. The hydrogen plasma treatment slightly roughens the metal contacts, but this does not introduce noticeable losses to impede the measurements. It is necessary to do the hydrogen plasma treatment as the last step, because it is the step with the lowest thermal budget; for example, if the contacts were

deposited after the hydrogen implantation, the hydrogen would diffuse out again during the 500 ^{o}C contact annealing step.

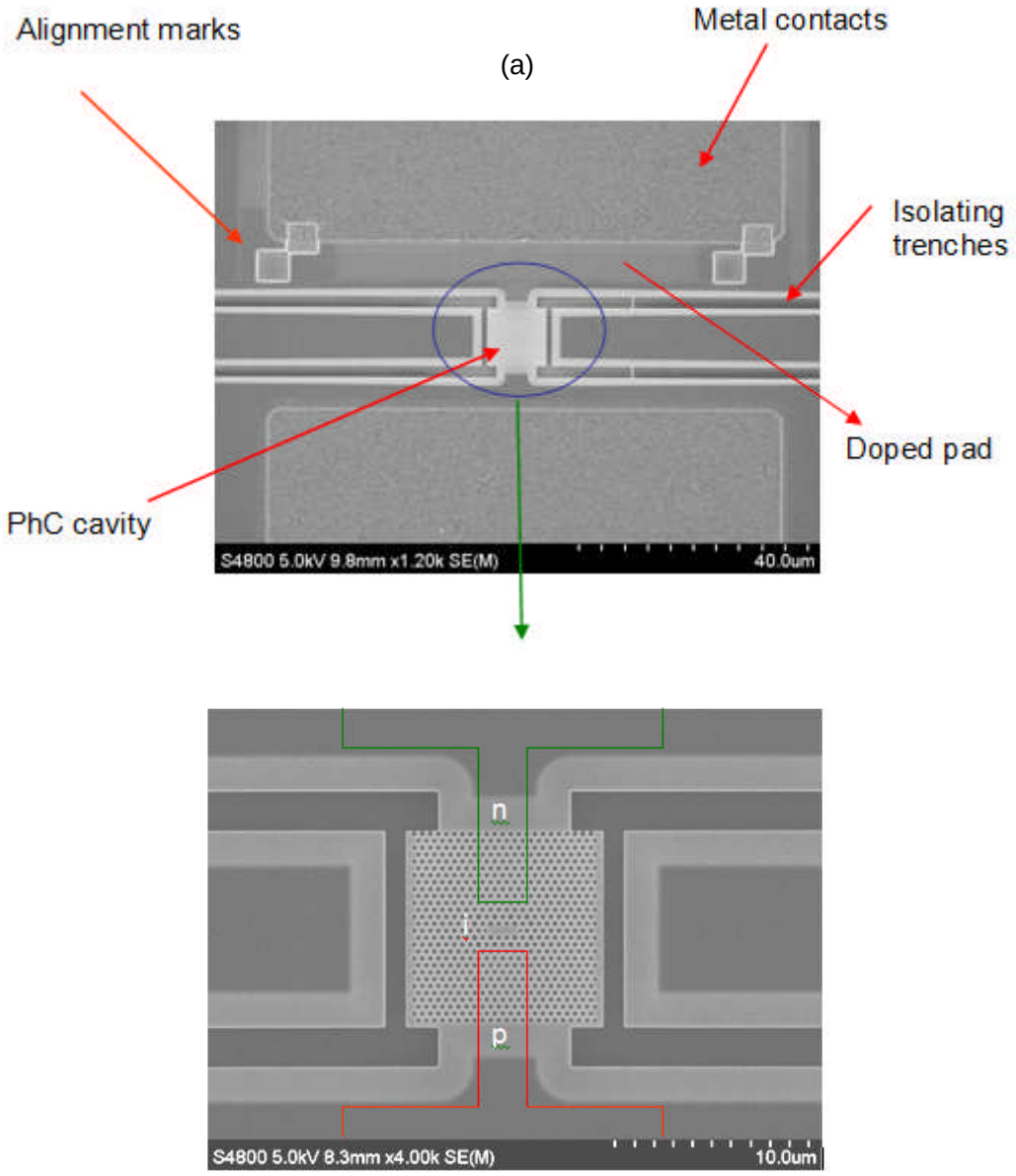

Figure 4.3: (a) SEM image of the fabricated device showing the PhC cavity, isolating trenches and metal contacts. (b) Zoomed image of the area encircled in blue in (a). The doped fingers are indicated by colored lines.

For the final device, a far-field optimized L3 PhC cavity was used, similar to the optically pumped device in Chapter 3. Other cavity configurations such as hetero-

structure cavities [8] and dispersion adjusted cavities [9], with and without oxide cladding were also tested, but their EL level was found to be much lower than that of the L3.

4.2 Characterization

The samples were then placed onto printed circuit boards (PCBs) and multiple cavities were wire bonded as shown in Figure 4.4(a). A forward bias of a few volts was applied to the device and its I-V response is shown below (Fig. 4.4(b)).

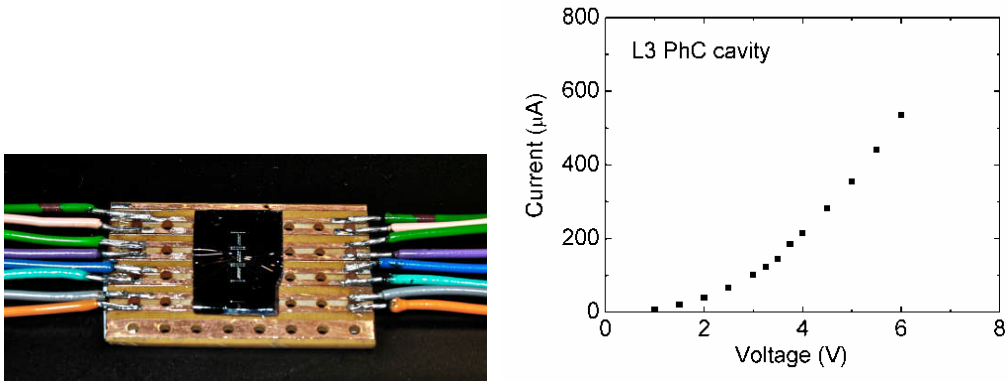

(a) (b)

Fig 4.4: (a) Picture of a set of devices and (b) I-V curve of the device.

The light emitted from the cavity was collected by the same μPL setup as the one used for all the PL measurements of Chapter 3. This allows us to directly compare the PL and EL level of the device.

The voltage applied to the EL devices was 3.5 V at a current of 156.5 μA. This corresponds to an input power of 0.55 mW, which is very similar to the input optical power (0.8 mW) of the optically pumped light source discussed in Section 3.8. The comparison of the output PL and EL levels for the fundamental emission line and expressed in pW/nm is given in Figure 4.5.

Interestingly, the emission level of the electrically pumped device is higher than that of the corresponding optically pumped device. Let us consider the two different processes. For optical pumping, the absorption is relatively low because of the weak absorption of light in the thin silicon slab at the incident wavelength (640 nm); we

estimate that only 5 % of the incident light is absorbed at 640 nm. Thus, from 0.8 mW input power, only 0.04 mW are absorbed to generate carriers. In contrast, the injection of carriers by electrical pumping appears to be more efficient, despite the fact that there are no carrier confinement mechanisms as, e.g. in III-V heterostructures, which gives rise to the higher output power for almost the same input power.

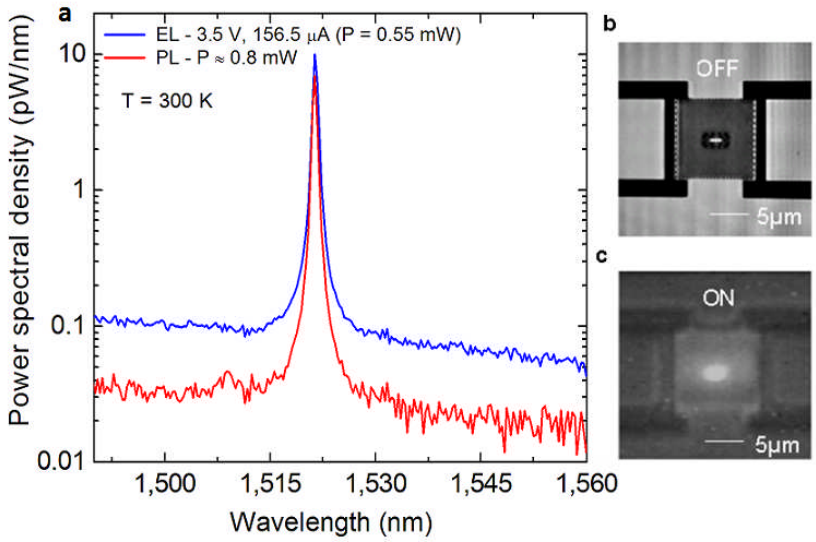

Figure 4.5: (a) Comparison of the power spectral density of an electrically (blue curve) and optically (red curve) pumped silicon PhC nanocavity [3] [1]. IR image of the device at off- state (b) and on-state (c).

In Figure 4.5 (a), the fundamental emission line of the cavity is shown at 1520 nm. This emission line can be easily tuned through the entire telecommunication range (1300-1600 nm) by changing the lattice period of the PhC cavity, similar to the optically pumped device shown in Figure 3.32 of Chapter 3.

An IR image of the device at zero voltage (off-state) and at 3.5 volts (on-state) is also shown in Figure 4.5 (b,c). This image was taken with an IR camera using a low pass filter with a cut-off wavelength around 1500 nm. A bright spot shows the emission of light from the PhC nanocavity on application of the voltage.

The Q-values of the PhC cavities in the electrically pumped device was only 4000. This value is much lower than the Q-values of the bare PhC cavities (without the fabrication steps required for electrical pumping). This reduction in Q-value is most probably due to imperfections introduced during the fabrication of the *pin* junction,

which requires multiple e-beam lithography and ion implantation steps. Free carrier absorption also plays a role in reducing the Q-values of the cavity.

4.2.1 Power spectral density and efficiency of the device

The power emitted from the device was measured directly by power meter in the μPL setup discussed in Section 2.3.2. The light collected from the device was fed to the power meter by the collection fibre. To estimate the power emitted from the cavity, the measured value was normalized to account for different loss mechanisms. These include percentage of light collected in the objective (60 % transmitted), the absorption in the objective (65 % transmitted) and other optical elements and percentage of light coming out vertically in upper plane (50 %). In total, we estimated a collected power of 5 pW for the electrical device by integrating over the entire cavity mode. If we integrate over the entire spectral range, then the power is 45 pW.

The power spectral density of the EL device is measured to be 10 pW/nm, as shown in Figure 4.5. If the emission area (1 μm^2) is considered, we obtain a power spectral density of 800 $\mu W/nm/cm^2$. This is the highest value reported from any silicon emitter to date. This statement holds even without considering the restriction of room temperature and sub-wavelength emission, as given in Table 4.2. The power spectral density of this device is even comparable to organic light emitting diodes (OLED). OLEDs usually have an output power density in the range of few mW/cm^2 and a linewidth of 10-60 nm or more depending on the material. Thus, OLEDs have a power spectral density less than 1 $mW/nm/cm^2$ [10], very much comparable to the value obtained by the silicon light source developed in this project.

For many applications, the power spectral density is the important figure of merit. For example, for multimodal operation in the field of biosensing, WDM applications in communications and spectral coherence in interferometry, all demand high power spectral density. Thus, this device can be of great interest to these applications.

Nevertheless, the measured wall plug efficiency of the device is only $0.7x10^{-8}$. This value is calculated based on the collected power. Such a low efficiency value is expected, considering that the emitting area is very small (1 μm^2) and the emission line is extremely narrow (<0.5 nm). In fact, the high performance of this device becomes evident on comparison with the emitted powers and efficiencies of comparable devices fabricated in direct bandgap (III-V) materials [5,11,12]. In these devices, the emitted

powers are also reported to be in the pW to nW level, similar to the power levels reported here. Also, the efficiency of our device is only an order of magnitude lower compared to the III-V nanolight sources, having the same configuration [5,11,12], where reported efficiencies are 1.6-3x10^{-8} [5] and 8x10^{-8}[12] at sub-threshold levels. A comparison of our device with different light sources based on III-V materials is given in Table 4.1.

4.2.2 Device stability and heating

Since the device is based on the introduction of hydrogen defects into silicon, it is only temperature-stable up to the hydrogen out-diffusion temperature of around 350 ^{o}C. Above 350 ^{o}C, hydrogen diffuses out of the device at which point the EL level drops.

The degree of device heating during operation can be estimated from the wavelength shift of the fundamental emission line. A red-shift of only 0.1 nm is measured experimentally on application of the active bias voltage. This shows that the device only heats by 1-2 ^{o}C at the applied voltage levels, which is consistent with the values reported in the literature for silicon and GaAs membraned PhC nanocavities under similar pumping conditions [13,14]. There might also be a masked blue shift of the cavity line due to free carrier absorption, which is typically of the order of 0.5 nm [2,4]. Considering this blue shift, the overall redshift is higher and the estimated device heating would be around 10-20 ^{o}C. The key point, however, is that none of these values approach the critical temperature for hydrogen out-diffusion, so we can assume that devices are long-term stable. Furthermore, the heat dissipation can be improved by the use of an oxide cladding [15], without compromising the performance of the device.

4.2.3 Features of the device

The light source presented in this chapter has the following main features.

i. Electrical pumping (156 µA current)
ii. Room temperature operation
iii. Small size (nanoscale)
iv. Sub-bandgap emission (1300-1600 nm)
v. Narrow emission line (laser like) (<0.5 nm)
vi. Tunability (through 1300-1600 nm)
vii. Spectral purity

Thus, in principle, this device has almost all the features desired from a Si light source, which were listed in Sections 1.2 and 1.6. For interconnect applications however, µW power level is required. Thus, in terms of emitted power, this device still needs an improvement.

4.2.4 Output behaviour

The integrated collected EL intensity was measured as a function of electrical input power (Fig. 4.6). Following an initial super-linear increase, the EL intensity saturates for 0.55 mW input power. The saturation behaviour is possibly due to free carrier absorption. The saturation of the output shows that FCA and losses are dominant and that there is a need to enhance the emission from Si PhC nanocavities further to have any chance of observing laser action. There is a possibility that the transition is itself saturating, but we believe that FCA is instead responsible for this saturation.

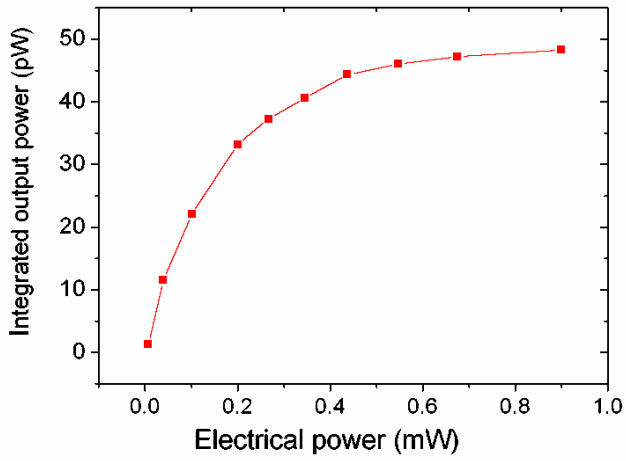

Fig 4.6: Integrated output power versus input electrical power. The output saturates at 0.55 mW input power.

4.3 Comparison with other devices

A comparison of different device features of our device with III-V nanolight sources of the same configuration is presented in Table 4.1 and with other Si light sources in Table 4.2.

Table 4.1: Comparison of our device with direct bandgap III-V nanolight sources with narrow emission lines.

Device	Pumping	λ (nm)	T (K)	Δλ (nm)	I (μA)	V (volts)	ρ (kΩ)	J (kA/cm^2)	P_{out}* (pW)	Power density** (μW/cm^2)	Power spectral density (μW/nm/cm^2)	Wall plug efficiency***	Additional features
InAs QD PhC cavity laser (above threshold) [5]	electrical	1170	<150	0.95	0.5	1.25	2500	0.05	0.2	20	23	$3x10^{-7}$	lasing
InAs QD PhC cavity laser (below threshold) [5]	electrical	1170	<150		0.225	1.25	5555	0.0225	0.01	1.0		$3x10^{-8}$	
InAs QD PhC cavity laser (at room temperature) [5]	electrical	1170	~300		1.0	1.25	1250	0.1	0.02	2.0		$1.6x10^{-8}$	
InGaAsP cavity laser (above threshold) [12]	electrical	1519	~300	0.5	300	1.75	5.8	30	300	30,000	60,000	$5 x10^{-7}$	lasing
InGaAsP PhC cavity laser (below threshold) [12]	electrical	1519	~300	---	150	1.25	8.3	15	15	1500	---	$8 x10^{-8}$	
This work	electrical	1200 to 1600	~300	0.5	150	3.5	23	15	4	400	800	$0.7 x10^{-8}$	

* Measured/detected output power

** Calculated using the emitting area

*** The wall plug efficiency is calculated by considering the measured/detected output power

Table 4.2. Comparison of different sub-bandgap silicon light sources.

Device	Pumping	λ (nm)	T (K)	Δλ (nm)	Power density* (μW/cm^2)	Power spectral density (μW/nm/cm^2)	Wall plug efficiency**	Additional features	Comments
Si:dislocation loops [16]	electrical	1150	~300	90	600	6.6	10^{-4}		broad area device, precludes large scale integration
Band-edge (structured) [17]	electrical	1150	~300	50	300	6	10^{-2} ***		broad area device, precludes large scale integration
A-centers [18]	optical	1280	<70	0.5	a.u	a.u	not reported	gain	works only at cryogenic temperatures
Raman laser [19]	optical	1686	~300	<0.001	~150x10^6	very high	10^{-2}, 0.28	lasing	electrical pumping not possible, large device, precludes large scale integration
W-centres [20]	electrical	1218	6	~1	2.7	2.7	10^{-7}		works only at cryogenic temperatures
Erbium in SiN (membraned) [21]	optical	1565	5.5	0.03	a.u	a.u	not reported	transparency	works only at cryogenic temperatures
Erbium in SiN (on Si) [22]	electrical	visible 1550	~300	100	a.u	a.u	not reported		
Bandedge (PhCs) [23,24]	optical	1100	~300	<0.5	a.u	a.u	not reported		band-edge emission
This work	electrical	1200-1600	~300	<0.5	400	800	10^{-8}		sub-bandgap, room temperature operation, electrically pumped, small size, suitable for interconnect and other silicon photonics applications

* Calculated using the emitting area

** The wall plug efficiency is calculated by considering the measured output power. Where output powers are given in arbitrary units (a.u), it is assumed that the power levels were too low to be measured and expressed in real numbers. As such the efficiency is considered lower than 10^{-10} and expressed as “not reported” in the table.

*** Output powers expressed in a.u. Efficiencies calculated by the power collected from big surface area of 4cm^2.

From Table 4.1, we can see that the output power of our device is comparable to the PhC cavity light sources made using direct bandgap semiconductors. Even the efficiencies are only an order of magnitude lower, a remarkable result for indirect bandgap silicon. The InAs QD PhC laser [5] has an advantage of lower input current densities comparable to our device but the input current densities in InGaAsP PhC cavity lasers [12] are comparable to ours.

From the comparison with other silicon light sources in Table 4.2, it is clear that, the device developed in this project is the first demonstration of an electrically pumped sub-bandgap silicon light source at room temperature. Although there have been reports on band-edge silicon LEDs having wall plug efficiencies higher than our device [16,17], these devices have a large footprint with very broad emitting areas. This would preclude high integration density on chip and hence the advantage of using silicon as a single material platform would not be relevant. Furthermore, this is the first demonstration of an electrically pumped silicon light source at room temperature that has a very narrow (<0.5 nm) laser-like emission. The term "laser-like" is used on the basis of narrow linewidth of the emission line.

4.4 Conclusions

By incorporation of hydrogen defects into a silicon photonic crystal cavity, I have successfully demonstrated an all-silicon nanolight emitting diode (LED). The current injection by incorporation of *pin* junction across the PhC cavity is an efficient process, resulting in greater EL level compared to the PL obtained for the same input power. This efficient current injection has been achieved by extending the fingers of p and n doped regions very close to the cavity, creating a depletion region around the cavity. This region is then populated by the carriers, which in turn become trapped at the hydrogen related defects in the cavity area. The trapped carriers recombine radiatively, to emit light, which is enhanced by the PhC cavity. By using this approach, a Si LED is developed having almost all the useful features listed in Section 1.2. In addition to these features, the device is also temperature stable up to 350 ^{o}C and heats up only by 10-20 ^{o}C at the current levels used for its operation. The collected output power of the device is 45 pW, when integrated over the whole band, while the peak power is 5 pW. The output powers and the efficiency (10^{-8}) of this device are comparable to the light sources

based on direct bandgap materials having the same configuration. The emission level (in picowatts) seems low but considering that this is based on an indirect bandgap material, it is considered a decent power level. With the present power levels, the device can find practical applications in refractive index sensing, discussed in the next chapter.

References

[1] A. Shakoor, R. Lo Savio, S. L. Portalupi, D. Gerace, L. C. Andreani, M. Galli, T. F. Krauss, and L. O'Faolain, "Enhancement of room temperature sub-bandgap light emission from silicon photonic crystal nanocavity by Purcell effect," Physica B 407, 4027–4031 (2012).

[2] R. Lo Savio, S. L. Portalupi, D. Gerace, A. Shakoor, T. F. Krauss, L. O'Faolain, L. C. Andreani, and M. Galli, "Room-temperature emission at telecom wavelengths from silicon photonic crystal nanocavities," Appl. Phys. Lett. 98, 201106 (2011).

[3] A. Shakoor, R. Lo Savio, P. Cardile, S. L. Portalupi, D. Gerace, K. Welna, S. Boninelli, G. Franzò, F. Priolo, T. F. Krauss, M. Galli, and L. O'Faolain, "Room temperature all-silicon photonic crystal nanocavity light emitting diode at sub-bandgap wavelengths," Laser Photonics Rev. 7, 114-121 (2013).

[1]Reprinted by permission © 2012 by WILEY-VCH Verlag GmbH & Co. KGaA, Weinheim.

[4] T. Tanabe, K. Nishiguchi, E. Kuramochi, and M. Notomi, "Low power and fast electro-optic silicon modulator with lateral p-i-n embedded photonic crystal nanocavity," Opt. Express 17, 22505-22513 (2009).

[5] B. Ellis, M. A. Mayer, G. Shambat, T. Sarmiento, J. Harris, E. E. Haller, and J. Vučković, "Ultralow-threshold electrically pumped quantum-dot photonic-crystal nanocavity laser," Nat. Photonics 5, 297-300 (2011).

[6] M. Settle, M. Salib, A. Michaeli, and T. F. Krauss, "Low loss silicon on insulator photonic crystal waveguides made by 193nm optical lithography," Opt. Express 14, 2440–2445 (2006).

[7] P. Cardile, G. Franzò, R. Lo Savio, M. Galli, T. F. Krauss, F. Priolo and L. O' Faolain, "Electrical conduction and optical properties of doped silicon-on-insulator photonic crystals," Appl. Phys. Lett. 98, 203506 (2011).

[8] B.-S. Song, S. Noda, T. Asano, and Y. Akahane, "Ultra-high-Q photonic double-heterostructure nanocavity," Nat. Materials 4, 207-210 (2005).

[9] K. Welna, S. L. Portalupi, M. Galli, L. O'Faolain, T. F. Krauss, "Novel dispersion-adapted photonic crystal cavity with improved disorder stability," IEEE J. Quantum Electron. 48, 1177-1183 (2012).

[10] S. K. Attili, A. Lesar, A. McNeill, M. Camacho-Lopez, H. Moseley, S. Ibbotson, I.D. Samuel, and J. Ferguson, “An open pilot study of ambulatory photodynamic therapy using a wearable low-irradiance organic light-emitting diode light source in the treatment of nonmelanoma skin cancer,” Brit. J. Dermatol. 161, 170-173 (2009).

[11] G. Shambat, B. Ellis, A. Majumdar, J. Petykiewicz, M.A. Mayer, T. Sarmiento, J. Harris, E. E. Haller and J. Vučković, “Ultrafast direct modulation of a single-mode photonic crystal nanocavity light-emitting diode,” Nat. Commun. 2, 539 (2011).

[12] H.-G. Park, S.-H. Kim, S.-H. Kwon, Y.-G Ju, J.-K. Yang, J.-H. Baek, S.-B. Kim and Y.-H. Lee, “Electrically Driven Single-Cell Photonic Crystal Laser,” Science 305, 1444-1447 (2004).

[13] M. E. Kurdi, X. Checoury, S. David, T. P. Ngo, N. Zerounian, O. Kermarrec, Y. Campidelli, and D. Bensahel, “Quality factor of Si-based photonic crystal L3 nanocavities probed with an internal source,” Opt. Express 16, 8780-8791 (2008).

[14] F. Intonti, N. Caselli, S. Vignolini, F. Riboli, S. Kumar, A. Rastelli, O. G. Schmidt, M. Francardi, A. Gerardino, L. Balet, L. H. Li, A. Fiore, and M. Gurioli, “Mode tuning of photonic crystal nanocavities by photoinduced non-thermal oxidation,” Appl. Phys. Lett. 100, 033116 (2012).

[15] S.-W. Jeon, J.-K. Han, B.-S Song, and S. Noda, “Glass-embedded two-dimensional silicon photonic crystal devices with a broad bandwidth waveguide and a high quality nanocavity,” Opt. Express 18, 19361-19366 (2010).

[16] Wai Lek Ng, M. A. Lourenço, R. M. Gwilliam, S. Ledain, G. Shao, and K. P. Homewood, “An efficient room-temperature silicon-based light-emitting diode,” Nature 410, 192–194 (2001).

[17] M. A. Green, J. Zhao, A. Wang, P. J. Reece, and M. Gal, “Efficient silicon light-emitting diodes,” Nature 412, 805-808 (2001).

[18] S. G. Cloutier, P. A. Kossyrev, and J. Xu, ”Optical gain and stimulated emission in periodic nanopatterned crystalline silicon”, Nat. Materials 4, 887 (2005).

[19] H. Rong, R. Jones, A. Liu, O. Cohen, D. Hak, and A. Fang, “A continuous-wave Raman silicon laser,” Nature 433, 725-728 (2005).

[20] J. Bao, M. Tabbal, T. Kim, S. Charnvanichborikarn, J. S. Williams, M. J. Aziz, and F. Capasso, “Point defect engineered Si sub-bandgap light-emitting diode,” Opt. Express 15, 6727-6733 (2007).

[21] Y. Gong, M. Makarova, S. Yerci, R. Li, M. Stevens, B. Baek, S. Woo Nam, L. Dal Negro, and J. Vuckovic, “Observation of transparency of erbium-doped silicon nitride in photonic crystal nanobeam cavities,” Opt. Express 18, 13863-13873 (2010).

[22] S. Yerci, R. Li, and L. Dal Negro, “Electroluminescence from Er-doped Si-rich silicon nitride light emitting diodes,” Appl. Phys. Lett. 97, 081109 (2010).

[23] S. Iwamoto, and Y. Arakawa, “Observation of enhanced photoluminescence from silicon photonic crystal nanocavity at room temperature,” Appl. Phys. Lett. 91, 211104 (2007).

[24] N. Hauke, T. Zabel, K. Müller, M. Kaniber, A. Laucht, D. Bougeard, G. Abstreiter, J. J. Finley and Y. Arakawa, “Enhanced photoluminescence emission from two-dimensional silicon photonic crystal nanocavities,” New J. Phys. 12, 053005 (2010).

Chapter 5

Refractive index sensing using light emission from silicon photonic crystal nanocavities

Refractive index sensing has many applications in our daily life, especially in the life sciences [1-4]. For example, refractive index sensing is used in biomedical laboratories to diagnose diseases by detecting the presence of specific biological components. In addition, refractive index sensing is also used for gas sensing [5,6] and finds applications in mining etc. It can also be used to monitor the presence of harmful gases in the environment. Thus, optical sensors are used extensively in our everyday life and a lot of effort has been put forward by researchers to develop sensors that can sense small variations of refractive index or absorption efficiently [1-6]. Furthermore, a lot of effort has been invested in reducing the size of these sensors so that they are compact and can have a high integration density on a chip [5-7]. Many different designs and materials have been used [1-7] but most of them usually operate on the same working principle, which is stated below.

The resonance wavelength of a resonator shifts when the refractive index surrounding it ($\lambda_n=\lambda_{vacuum}/n$) changes. This shift is then used for sensing of gases or biological compounds, as shown in Figure 5.1.

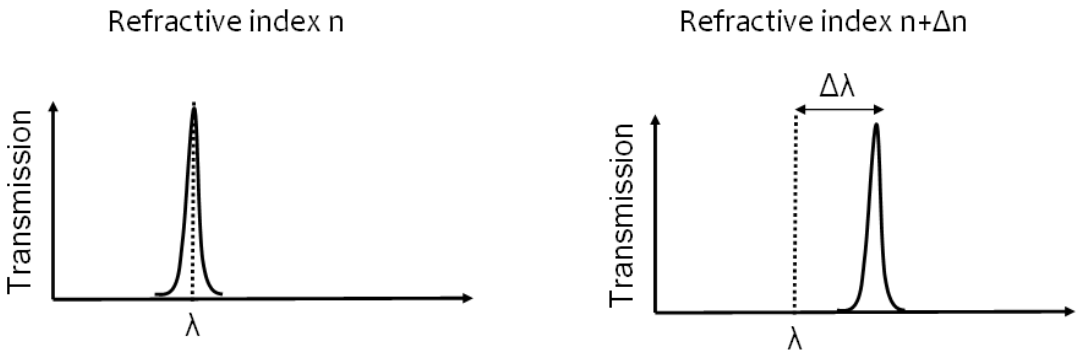

Figure 5.1: The shift of the resonance wavelength of the cavity due to change of refractive index.

5.1 Performance parameters of refractive index sensors

5.1.1 Sensitivity

A key performance parameter of a refractive index sensor is its sensitivity (S). The sensitivity of the sensor is given by the ratio of the change in resonance wavelength (Δλ) to the change in the refractive index (Δn) and is usually expressed in wavelength shift in nanometers per refractive index unit (RIU). The sensitivity of the sensor also depends on the overlap of the mode with the material, η, and the effective index experienced by the mode, as given in the following equation.

$$S = \frac{\Delta\lambda}{\Delta n} = \eta\left(\frac{\lambda}{n_{eff}}\right) \qquad \text{Equation 5.1}$$

Thus, the greater the mode overlap with the element to be sensed, the greater the sensitivity of the device.

5.1.2 Detection limit

The second important performance parameter of a refractive index sensor is the detection limit (DL). This parameter describes the capability of the sensor to detect the minimum possible change of refractive index. It is given as the ratio of the resolution and the sensitivity.

$$DL = \frac{R_{total}}{S} \qquad \text{Equation 5.2}$$

R_{total} stands for the total sensor resolution, which is defined as the smallest possible spectral shift that can be measured. The sensor resolution is limited by three factors, namely a) the spectral resolution, which depends on the resonance linewidth of the cavity (Q-factor) or the spectral resolution of the measurement setup, b) amplitude noise and c) temperature instability. The amplitude noise can be due to many factors like thermal and shot noise in the detector, laser relative intensity noise etc. Due to amplitude noise some error in the exact spectral location of the mode peak is expected. The amplitude noise is quantified by the signal to noise ratio (SNR). Like amplitude noise, the thermal fluctuations in the system also induce errors due to the non-zero thermo-optic coefficient of the sensor material. Hence, there can be a slight mode shift due to temperature variations as well.

Following reference [8] the total resolution can be expressed as a 3σ of the total noise, caused by three error factors listed above, by summing up all the three noise variances in the system as follows:

$$R_{total} = 3\sqrt{\left(R_1^2 + R_2^2 + R_3^2\right)} \qquad \text{Equation 5.3}$$

where R_1, R_2 and R_3 correspond to noise variances caused by spectral resolution, amplitude noise and thermal noise, respectively, all expressed in picometers, and

$$R_1 = \frac{\lambda}{4.5Q\left(SNR\right)^{1/4}} \qquad \text{Equation 5.4}$$

Equation 5.1 shows that the greater the mode overlap with the element to be sensed, the greater the sensitivity, and the lower the detection limit. The limitation on the detection limit due to temperature instability is more pronounced if the mode is mainly carried in a material with a high thermo-optic coefficient such as silicon; for example, in the Ln photonic crystal cavity. Otherwise, the detection limit is mainly limited by the cavity linewidth (Q-value) or the resolution of the measurement setup.

5.2 Photonic crystal cavity based refractive index sensors

The realization of photonic crystal cavities with very high Q/V values allows for strong light matter interaction within a very small volume [9,10]. This strong light matter interaction enables the detection of small changes in the refractive index of the material, allowing the development of a refractive index sensor with a capability of sensing very small changes in the refractive indices [4-6]. As discussed above, higher mode overlap increases the sensitivity of the device. For this reason, for sensing applications, the slotted PhC cavity geometry has been developed recently [4-6]. In a slotted PhC cavity, a narrow (100-150 nm) air slot is introduced. Due to the discontinuity of the electric field at the edges of the slot, TE polarized modes are supported in the air slot. Since the mode is confined in the air slot, the overlap with the refractive index change is increased, increasing the sensitivity of chemical detection. Different designs of slotted PhC cavities have been used in the past to develop refractive index sensors [4-6]. In [5,6] a heterostructure approach [13] was used, resulting in Q-values of up to 50,000, detection limits of 7.8×10^{-6}, and a sensitivity of 1500 nm/RIU [5]. The dispersion

diagram of this device with its resonance wavelength, Q-value and mode profile is given in Figure 5.2(a).

In [6], the cavities are realized by the modulation of the slot width, also giving high Q-value of 26000. The detection limit in this case is reported to be $1x10^{-5}$ with a sensitivity value of 510 nm/RIU. The SEM image, dispersion diagram and mode profile of this device is shown in Figure 5.2(b).

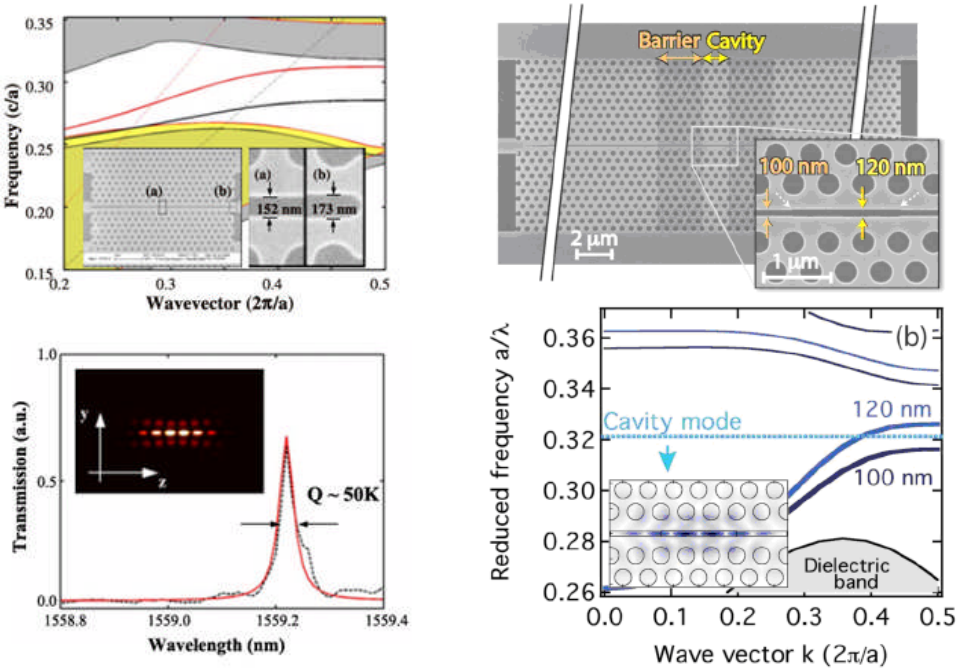

(a) (b)

Figure 5.2: Dispersion diagram, SEM pictures and mode profile of different slotted cavity designs used for sensing applications. (a) HS slotted cavity with reduced central period [5][1]. (b) HS slotted cavity with slot width modulation [6][2].

Drawback

The performance of these slotted cavity sensors is quite remarkable, but they operate in the end-fire scheme, which requires a complex optical setup. To use these devices, an expensive external laser and very fine alignment of the external optical components are required. Thus, although these sensing devices show very good performance, they are difficult to use in practise. Here, we present an alternative approach that should be more amenable for applications.

Solution

The requirements of external laser and fine alignment can be avoided if instead, a PhC nano LED is used as the narrow linewidth light source. The mechanism of sensing is the same, i.e., a shift of the emission peak with the change of the refractive index. This makes the use of PhC cavity based sensors relatively easy and opens up the possibility of large scale integration, all enabled by our silicon nano LED, the cheapest narrow linewidth light source in existence.

5.3 Refractive index sensing using light emission from silicon nanolight source

In this section, I demonstrate gas sensing with sensitivity values comparable to the silicon PhC nanocavity based sensors operating in the end-fire scheme [5,6].

5.3.1 Design of the PhC cavity

Light sources based on two different designs of silicon PhC nanocavities were used.

The first design is a modified L3 PhC cavity, discussed in detail in Chapter 2. We used an r/a value of 0.3 and a period of 360 nm for operation at 1300 nm.
The second design is similar to [5] with a period of 490 nm and an r/a value of 0.26. The slot width is around 100-150 nm, resulting in an emission line around 1500 nm.
I used two different designs to demonstrate the effect of mode overlap and possibility of electrical pumping by using Ln cavities.

The fabrication details of the cavities have been explained in Chapter 2, as well as the hydrogen-treatment described in Chapter 3. The emission wavelength (1500 nm) in our slotted cavity is lower than reported in [5] (1560 nm), although the same design and geometric parameters of the PhC were used. This is because after the fabrication, the diameter of the PhC holes was slightly larger than the target value, causing a blue shift. A further 20 nm blue shift of the emission line was caused by the hydrogen plasma treatment, as shown in Figure 3.15.

5.3.2 Characterization

The μPL setup discussed in Chapter 2 was used for sensing experiments and slightly altered by attaching a gas inlet to the cryostat. The measurements were carried out at

room temperature and the cryostat chamber was used only for the introduction of different gases, i.e. not for cooling.

The position of the emission peak was measured in four different refractive index conditions: vacuum, air, nitrogen and helium. The refractive indices of these gases at 1500 nm wavelength, atmospheric pressure and room temperature are n_{air}=1.000265, n_{vacuum}=1, n_{helium}=1.000032 and $n_{nitrogen}$=1.000270 [6].

The shift of the fundamental emission line for the two different cavity designs following the introduction of gases is given in Figure 5.3. A 70 pm red-shift is observed in the case of L3 cavity by changing the ambient from vacuum to air ($\Delta n=2.65\times10^{-4}$), see Figure 5.3(a). For the slotted PhC cavity, a shift of 150 pm is observed when the ambient is changed to nitrogen from vacuum ($\Delta n=2.7\times10^{-4}$), see Figure 5.3(b).

The shift in the emission peak for the same refractive index change is higher for the slotted cavity due to its larger mode overlap with the gas compared to the L3 cavity, resulting in higher sensitivity. When we introduce helium, the shift is negligible, as the corresponding refractive index change of 3.2×10^{-5} is almost at the detection limit of the device, as shown below.

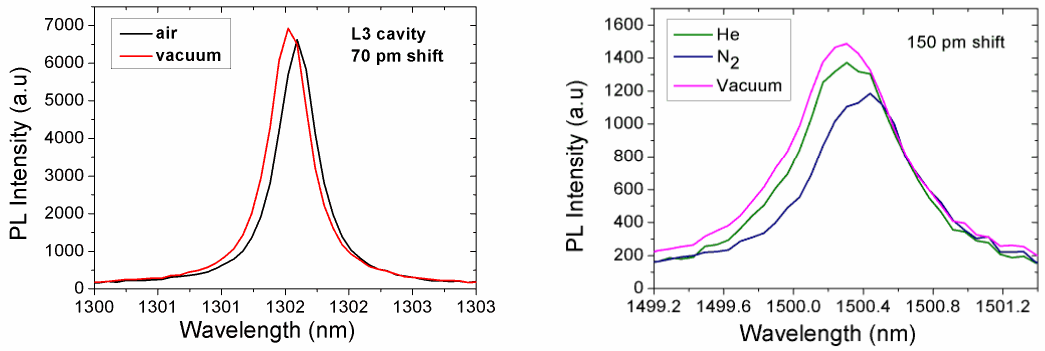

(a) (b)

Figure 5.3: Shift of the fundamental emission line of a silicon PhC light source as a function of the refractive index. (a) L3 PhC cavity based light source, (b) slotted PhC cavity based light source. A larger shift is observed for the slotted PhC cavity (150 pm) compared to the L3 cavity (70 pm) due to the greater mode overlap with the gas.

5.3.3 Calculation of sensitivity and the detection limit of the device

Using Equation 5.1, the sensitivity of a slotted PhC cavity is calculated to be 555 nm/RIU, which is comparable to the value reported in [6].

The detection limit is calculated by using Equations 5.2 to 5.4 using the following values: Active Q-factor = 2000.

R_1 = 5.27 pm, calculated using Equation 5.4. SNR value used is $1x10^6$, taken from [8].

$R_2 = 1.1xR_1$= 5.79 pm.

R_3 = 10 fm, value taken from [8].

R_{total} = 23.5 pm.

Detection limit, DL= $4x10^{-5}$.

The calculated detection limit of our device is almost an order of magnitude higher than the ones reported in [5,6]. This is due to the low active Q-factor of the PhC cavity. The active Q-factor is limited by the free carrier absorption and far-field optimization of the cavity, which gives the maximum vertical out-coupling of the light. There is a compromise between the Q-factor and the vertical light emission linked to the SNR. The use of higher Q-value cavities and the use of less aggressive far-field optimization will help to improve the detection limit.

The devices were pumped optically in all the results shown here. For Ln cavities, the same results can be repeated with electrical pumping which would make our sensing device even more practical to use. The sensitivity would be comparatively lower for electrically pumped devices as the Q-factor is typically limited by free carrier absorption, and the mode is mainly situated in the silicon material, so the overlap with the gas is low; however, the ease of use provided by electrical pumping is a very attractive feature.

One disadvantage of this approach is that it requires an optical spectrum analyzer (OSA) to record the emission spectrum. If the emission power from the light source is lower than the minimum detection limit of the OSA, then very sensitive detectors are required, which adds to the total cost. Thus, there will be not much advantage from the point of view of cost reduction, although the ease of use would still be an advantage. An increase in the output power of the device would enable us to use a cheaper detector, decreasing the cost of its use as a sensor.

5.4 Future application - Biosensing

5.4.1 Approach 1

I have now demonstrated the gas sensing capability of the PhC cavity light source. This approach could be extended further to the sensing of biological components. For example, a microfluidic channel could be integrated to introduce biological substances. The introduction of biological substances would change the refractive index, which would be sensed by the shift of the emission peak as before.

The schematic of the purposed lab-on-a-chip biological sensor is shown in Figure 5.4. This scheme would also require an OSA or a sensitive detector if the maximum output power is below the detection limit of the OSA.

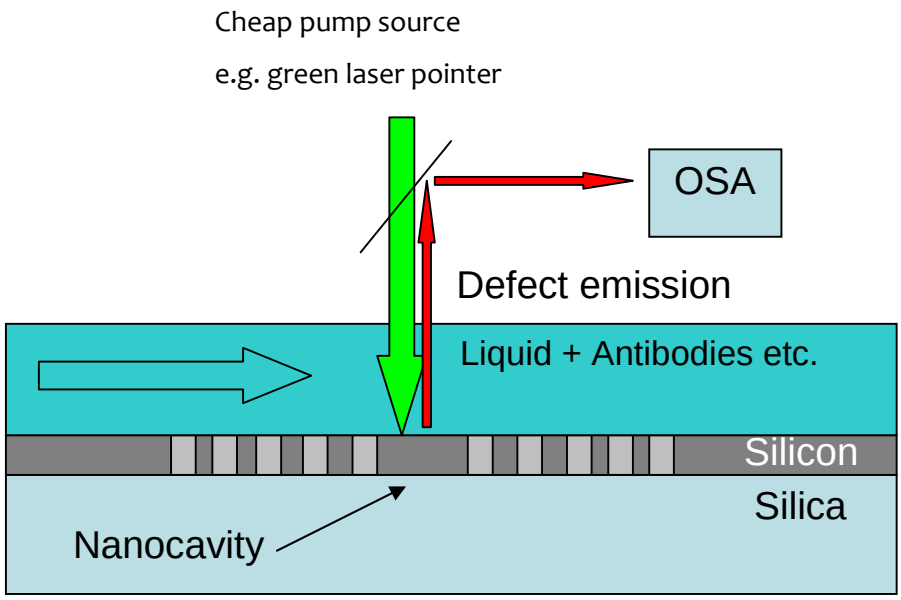

Figure 5.4: Schematic of the proposed lab-on-a-chip biological sensor with on-chip silicon light source.

5.4.2 Approach 2

Another approach can be taken where even the use of an OSA can be avoided and instead a simple detector can be used to record the signal. A schematic of this approach is shown in Figure 5.5. In this design, the Si PhC cavity light source can be pumped either electrically or optically by a simple green laser pointer. The light generated in the

cavity will be collected in the waveguide by side coupling, as shown by the zoomed area around the PhC in Figure 5.5. A suitably designed ring resonator would be placed next to this bus waveguide. If the wavelength of the light emitted by the light source is on resonance with the ring, a low output signal would be detected. Otherwise, the detector will record a high output signal. A change of the detected signal from lower to higher value or vice versa would indicate a change in the refractive index. Instead of a detector, an infrared camera could also be used. In an improved version, two bus waveguides could be used on the ring, i.e. a drop port and a through port, each with their own detector. In this way, one of the detectors will always record the signal. A shift of the signal from one detector to the other would indicate a change of the refractive index.

The device configuration proposed here combines a very cheap source and detection system and could find practical applications in clinics.

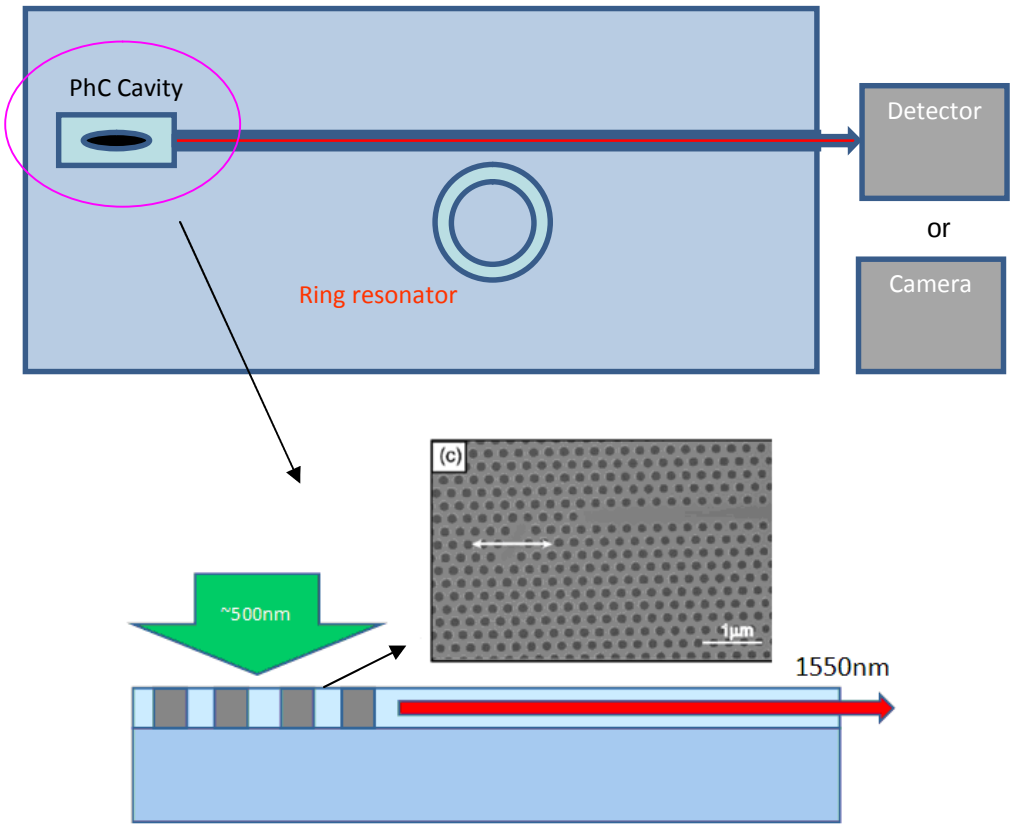

Figure 5.5: Schematic of a proposed biological sensor based on silicon PhC cavity light source. Instead of OSA, the output can be measured by a simple detector or a camera.

5.5 Conclusions

I have demonstrated the refractive index sensing by using the fundamental emission line of a photonic crystal nanocavity light source, developed in Chapters 3 and 4 of this thesis. Using this approach, the sensing has become much easier compared to the end-fire coupled scheme, which requires expensive external pump laser and complex alignment of an optical setup. By using an on-chip Si light source instead, the use of external laser and a complex optical setup are avoided to demonstrate a cheap and an easy to use gas sensor. The sensitivity of the sensor is 555 nm/RIU, comparable to the state of the art PhC refractive index sensors [5,6]. The detection limit of our device is an order of magnitude higher (10^{-5}) compared to [5,6] due to the low active Q-factor of the cavity. This can be improved by increasing the Q-factors of the cavity by using less aggressive far-field optimization. The device can also be pumped electrically by using light emission from Ln cavities, instead of a slotted cavity but with some compromise on sensitivity. The applications of this device can be extended to biological sensing as well. I have proposed two device configurations as a future work direction. These devices would result in a lab on a chip biosensor with a very cheap light source and detection system that could be used easily in clinics.

References

[1] C. L. Baird, and D. G. Myszka, “Current and emerging commercial optical biosensors,” J. Mol. Recognit. 14, 261–268 (2001).

[2] K. De Vos, I. Bartolozzi, E. Schacht, P. Bienstman, and R. Baets, “Silicon-on-Insulator microring resonator for sensitive and label-free biosensing,” Opt. Express 15, 7610–7615 (2007).

[3] H. Li, and X. Fan, “Characterization of sensing capability of opto-fluidic ring resonator biosensors,” Appl. Phys. Lett. 97, 011105 (2010).

[4] M. G. Scullion, A. Di Falco, T. F. Krauss, “Slotted PhC cavities with integrated microfluidics for biosensing applications,” Biosens. Bioelectron. 27, 101-105 (2011).

[5] A. Di Falco, L. O’Faolain, and T. F. Krauss, “Chemical sensing in slotted photonic crystal heterostructure cavities,” Appl. Phys. Lett. 94, 063503 (2009).

[1]Reprinted with permission. Copyright [2009], American Institute of Physics.

[6] J. Jágerská, H. Zhang, Z. Diao, N. Le Thomas, and R. Houdré, “Refractive index sensing with an air-slot photonic crystal nanocavity,” Opt. Lett. 35, 2523-2525 (2010).

[2]Reprinted with permission. Copyright [2010], Optical society of America.

[7] J. Homola, S. S. Yee, and G. Gauglitz, “Surface plasmon resonance sensors: review,” Sens. Actuators B 54, 3–15 (1999).

[8] I. M. White and X. Fan, “On the performance quantification of resonant refractive index sensors,” Opt. Express 16, 1020 (2008).

[9] E. Kuramochi, M. Notomi, S. Mitsugi, A. Shinya, T. Tanabe, and T. Watanabe, “Ultrahigh-Q photonic crystal nanocavities realized by the local width modulation of a line defect,” Appl. Phys. Lett. 88, 041112 (2006).

[10] T. Asano, B. S. Song, Y. Akahane, and S. Noda, “Ultrahigh-Q nanocavities in two-dimensional photonic crystal slabs,” IEEE J. Sel. Top. Quantum Electron. 12, 1123 (2006).

[11] X. Fan, I. M. White, S. I. Shopova, H. Zhu, J. D. Suter, and Y. Sun, “ Sensitive optical biosensors for unlabeled targets: A review,” Anal. Chim. Acta 620, 8-26 (2008).

[12] M. Loncar, A. Scherer, and Y. Qiu, “Photonic crystal laser sources for chemical detection,” Appl. Phys. Lett. 82, 4648 (2003).

[13] T. Akahane, T. Asano, B.-S. Song, and S. Noda, “High-Q photonic nanocavity in a two-dimensional photonic crystal,” Nature 425, 944-947 (2003).

Chapter 6

1280 nm silicon emission line (G-line)

In Section 1.3.3.2.2, I gave a brief overview of the different types of emission lines from silicon. Introducing different impurity atoms in to the silicon creates these emission lines. These lines are called the C-line (1.5 μm) [1], D-lines (different wavelengths) [2], W-line (1218 nm) [3] and G-line (1280 nm) [4]. The most successful attempt to make a light source in silicon has so far been the G-line, as optical gain and stimulated emission have been demonstrated [5]. Unfortunately, the G-line could only be observed at low temperatures (maximum 80 K), negating the possibility of making a practical device. Furthermore, the G-line emission intensity is not sufficient to use it for practical applications. We decided to investigate the possibility of increasing the G-line emission intensity and also make its operation possible at room temperature. In Chapter 3, the Purcell effect was successfully exploited to enhance the sub-bandgap hydrogen related defect luminescence and to achieve temperature stability. In the present chapter, the same approach has been applied to the G-line emission. At the start of the chapter, I have provided a brief overview of the origin of the G-line, its properties and the light emission mechanism. After this, experimental results are presented. I conclude with suggestions for future experiments relating to the G-line emission in silicon.

6.1 G-line

“G-line” is a name given to a narrow emission line in silicon at a wavelength of 1280 nm. It has a linewidth of 0.1-0.2 nm. The G-line emission has already been discussed by a number of authors [4-6]. Initially, the G-line was reported as a result of electron, gamma ray or neutron irradiation. The motivation of this research was not silicon light emission, but to study the effect of such exposure on electronic properties [6,7]. The G-line emission intensity was also used to quantify the presence of carbon content in silicon [8]. It was not until 2005 that the use of the G-line was considered for a light source. Since then, several reports on the study of the G-line from the point of view of enhancing the silicon emission have come forward [5,9].

6.1.1 Mechanism of the G-line emission

The G-line originates from the complex of substitutional and interstitial carbon atoms in silicon. Such complexes are called G-centres, which also give the emission line its name. G-centres can be created by implanting silicon with carbon, which then forms a complex with substitutional carbon already present in silicon as an impurity. The G-line can also be induced by electron irradiation [4]. The high energy e-beam creates silicon self interstitials. The self interstitials are mobile and migrate towards the substitutional carbon. The silicon replaces the carbon at the lattice site, making the carbon interstitial. The interstitial carbon becomes mobile and migrates to other substitutional carbon atoms to form a complex of interstitial and substitutional carbon atoms, called a G-centre. The mechanism of G-line emission has been explained well in reference [10] and is explained below.

The G-centre is bi-stable and can exist in two atomic configurations, referred to as A and B. Only the B-configuration is optically active [6]. The G-centre can trap an electron from the conduction band or a hole from the valence band in both configurations, depending on whether it is in acceptor or donor state, respectively. The B-configuration involves two C-substitutionals and one Si-interstitial. In the neutral ground state, the G-centre usually exists in the B-configuration. These two configurations are shown schematically in Figure 6.1.

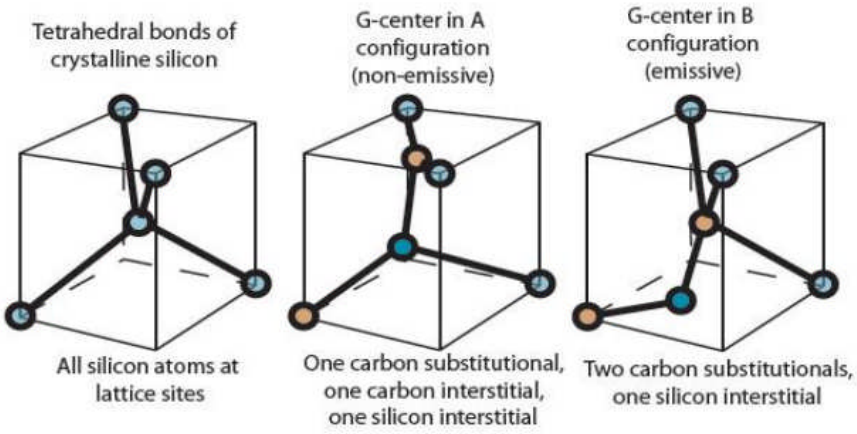

Figure 6.1: Silicon crystal structure and two configurations of G-centres in silicon [10].

Since the SOI used in our experiments is slightly p-type doped, the donor state is above the Fermi level and the G-centre can capture a free hole to become positively charged. It can also capture a hole from a bound exciton. At cryogenic temperatures, the G-centre would stay in the B+ configuration but with the increase of temperature it can transform to A+ configuration, by diffusion of carbon atoms and becomes optically inactive. The symbol "+" means that it is positively charged. At low temperature operation, the G-centre will trap an electron to transform into an excited state from the B+ state, indicated by B* in Figure 6.2. The captured electron and hole then recombine to emit a photon of wavelength 1280 nm and the G-centre will then relax back to the neutral B-configuration. The mechanism of G-line emission in p-type silicon is shown in Figure 6.2.

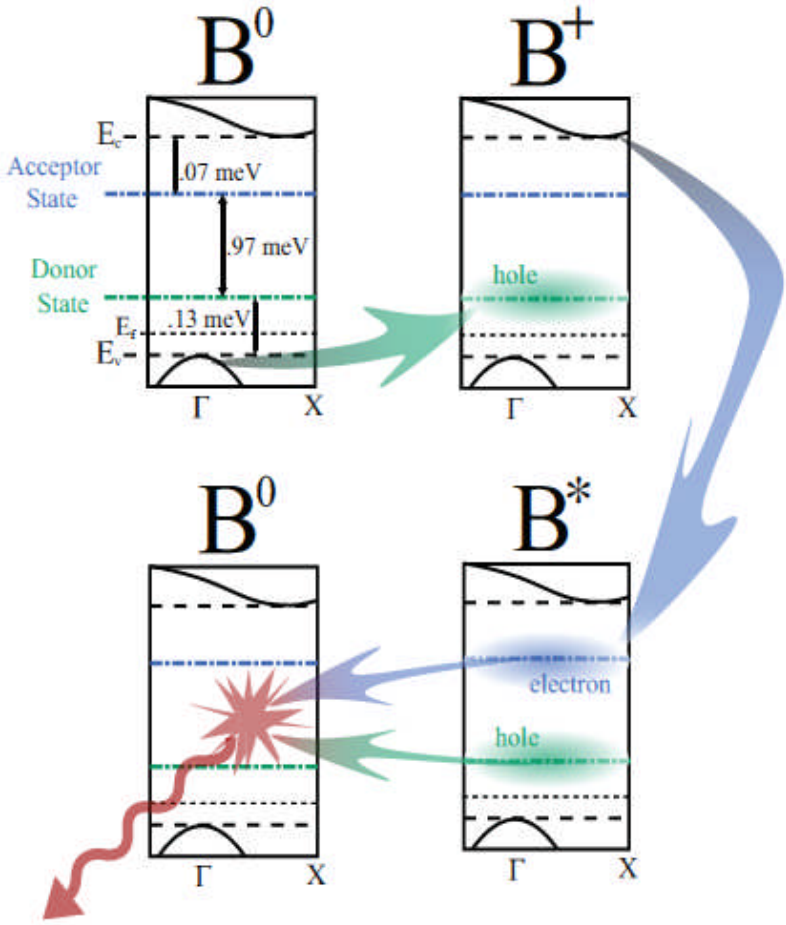

Figure 6.2: Emission mechanism of G-line in p-type silicon [10].

The mechanism explained above is valid only at low temperatures, as with a temperature increase, the G-centre converts to the optically inactive A-configuration. If the hole is captured from the bound exciton instead of free hole from the valence band, then at higher temperature, the exciton would disassociate itself from the G-centre due to diffusion at higher temperature, impeding the emission mechanism. Thus, the G-line only works at lower temperatures.

6.2 Experimental results

6.2.1 Creation of G-line by carbon ion implantation

As a first step, the G-centres were created in the SOI wafer by carbon implantation (courtesy of Dr Giorgia Franzò, Universiy of Catania). Different implantation conditions (implantation energy and carbon dose) were used to maximize the G-line emission intensity. Keeping the implantation energy fixed at 35 keV, the carbon dose was varied from 10^{10} C/cm^2 to 10^{13} C/cm^2. For PL measurements the samples were pumped by a CW laser operating at 640 nm. The PL spectra of implanted SOI, taken at low temperature (7 K), shows that the G-line intensity decreases with increasing carbon dose, as shown in Figure 6.3(a). The maximum carbon concentration with the given implantation conditions was at 120 nm below the surface, i.e. almost in the middle of the top Si layer, Figure 6.3(b). The decrease of the G-line intensity by increasing the carbon dose is probably due to the formation of carbon complexes other than G-centres.

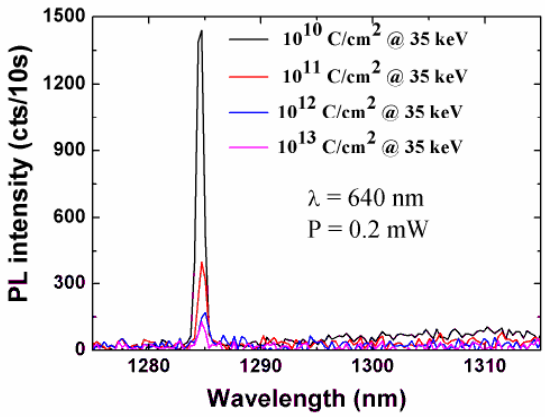

Figure 6.3(a): PL spectra of SOI implanted with different carbon doses. The maximum G-line intensity is achieved with lower carbon doses. The PL spectra were taken at low temperature, 7 K.

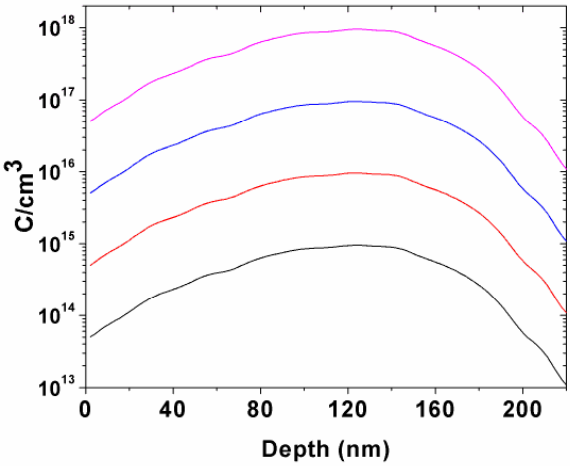

Figure 6.3(b): Maximum carbon concentration occurs at a depth of 120 nm. The legends are the same as in 6.3(a).

Similarly, the increase of the implantation energy also reduces the G-line intensity, as shown in Figure 6.4(a), where PL spectra of SOI implanted with 3 different energies (15, 35 and 50 keV) for a constant carbon dose (10^{11} C/cm^2) are shown. The carbon implantation profile of SOI for different implantation energies is shown in Figure 6.4(b).

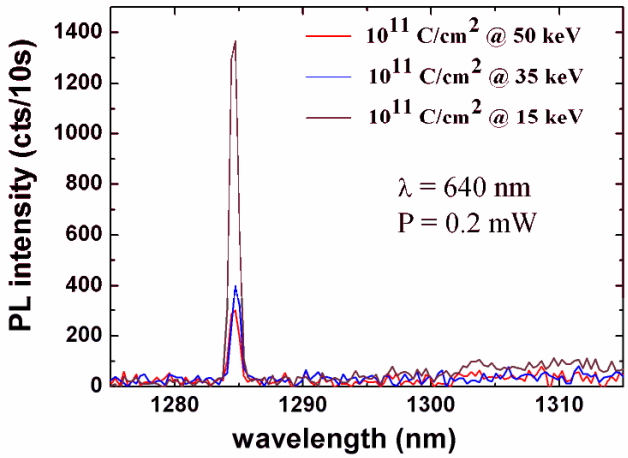

Figure 6.4(a): G-line intensity from carbon implanted SOI using different implantation energies. Spectra taken at 7 K.

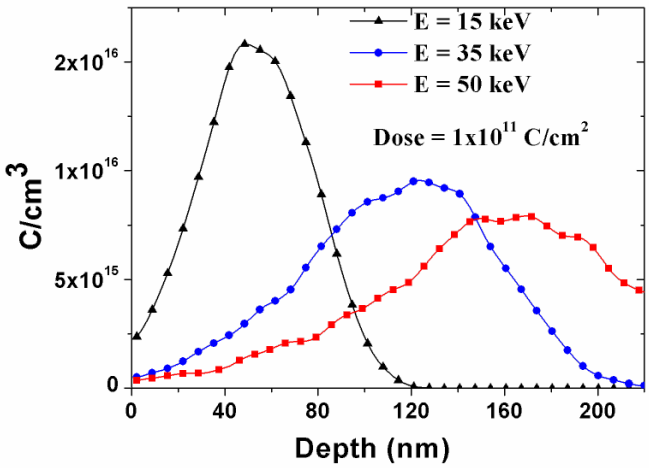

Figure 6.4(b): Implantation profile of SOI using different implantation energies

We propose the following two reasons for the decrease of the G-line intensity by increasing the implantation energy:

1. The G-line may be a surface effect only. Implantation at higher energies creates carbon complexes much deeper inside the material, which might not give rise to G-line emission. This reason is less probable however, as carbon diffusion in silicon is very high even at room temperature.
2. The high energy carbon atoms displace the substitutional carbon atoms already present in the silicon. This decreases the amount of substitutional carbon atoms and hence the G-line concentration. This in turn reduces the G-line intensity.

From these experiments, it is concluded that the highest G-line intensity is obtained by using low implantation energy and carbon dose. For further experiments, the SOI wafers were implanted at 35 keV with a carbon dose of 10^{10} C/cm^3. This implantation energy led to the maximum carbon concentration being at the centre of the top silicon layer.

6.2.2 Gain measurement

Gain measurements of the C-implanted SOI were carried out by pumping the sample from the top and measuring the output intensity from the edge of the sample, as shown in the inset of Figure 6.5. We kept the size of the spot constant, and increased the pump power; if internal gain occurs in this configuration we should observe a super-linear

effect. The pump power was varied from 1 mW to 70 mW, with a maximum power density of 5 W/cm^2. Throughout the pump power range, a linear trend of the output intensity was observed; hence no gain is present in the system. In reference [4], by using the variable strip loaded method, gain had been observed at 65 W/cm^2, much higher than the power levels used in our experiments. The lower input power density used in our experiments was due to the large spot size obtained by the cylindrical lens used in the setup, and the limitation on laser power.

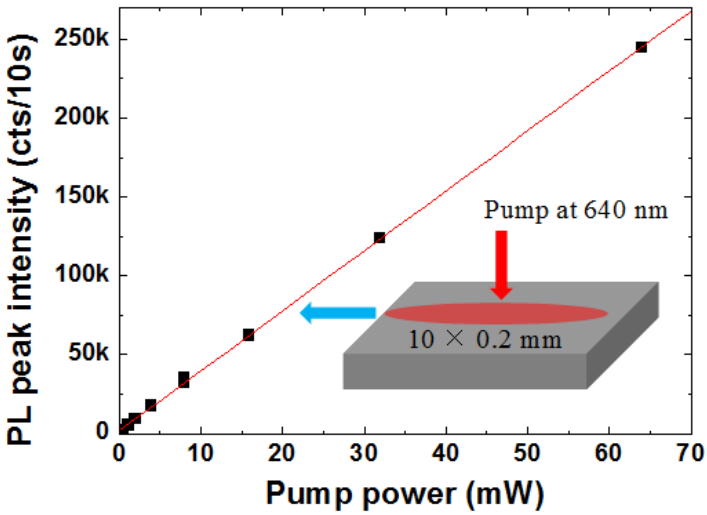

Figure 6.5: Trend of the output PL intensity with respect to the input power.

6.2.3 G-line in the photonic crystal cavity

L3 PhC cavities operating at the G-line wavelength were fabricated in SOI. The design of the cavity was discussed in detail in Chapter 2. Lithographic tuning was carried out to match the cavity resonance with the G-line, as shown in Figure 2.3. The fabrication details are the same as explained in Chapter 2.

Carbon implantation was carried out after the fabrication of PhC cavities. The PL measurements at low temperature reveal that the intensity of G-line emission from the PhC cavity area is drastically lower compared to the unetched SOI, as shown in Figure 6.6. The figure also shows a sharp emission peak at 1310 nm, which arises due to hydrogen related defects, emitting on resonance with the cavity, as discussed in Chapter 3.

We suggest the following reasons for the low G-line intensity from the etched sample.

1. Creation of non-radiative recombination sites due to the etching of the holes. The lifetime of the carriers at the etched hole side walls is very short (≈100 ps) [11] compared to the G-line lifetime, which is in the microseconds range [7].
2. The substitutional carbon atoms are knocked out during the etching process.

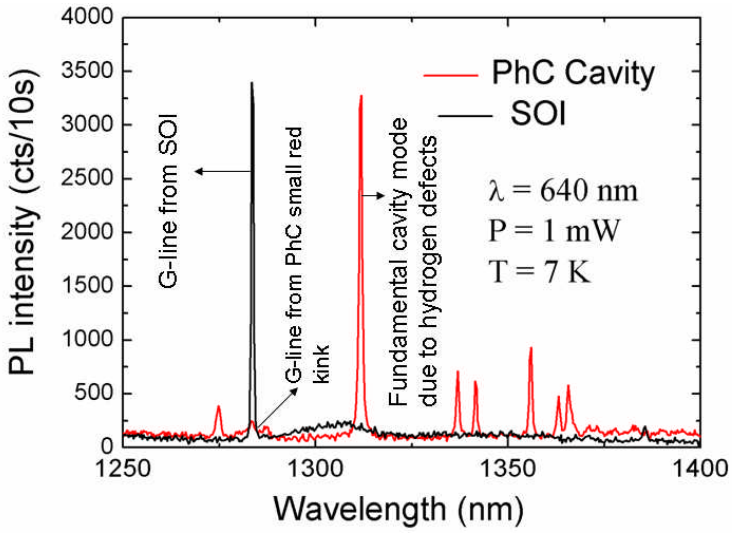

Figure 6.6: PL spectra showing fundamental cavity line (defect luminescence) and G-line from SOI and PhC cavity. The intensity of G-line emission from PhC is lower compared to that from SOI.

As depicted in Figure 6.6, the fundamental cavity line (at 1310 nm) is not spectrally matched with the G-line (1280 nm). When the cavity is tuned to spectrally overlap the G-line, an emission enhancement by a factor of 3 is observed, as shown in Figure 6.7. From Figure 6.6, we can see that the PL intensity of the fundamental cavity line due to defect luminescence is 3200 cts/10sec, while that of G-line is only 200 cts/10sec. When the G-line is on resonance with the cavity, the overall emission intensity is 9000-10,000 cts/10sec, shown in Figure 6.7. Thus, the two emission lines do not just sum up but enhance each other by a factor of 3, which is an indication of interaction between the G-line and the cavity.

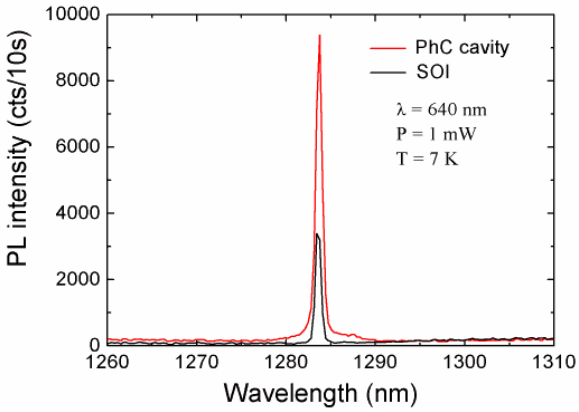

Figure 6.7: When the G-line is on resonance with the cavity, a 3-fold emission enhancement is obtained indicating the presence of the Purcell effect.

6.3 Future work

The indication of interaction between the cavity and the G-line is very promising and shows that the approach of enhancing the G-line emission via the Purcell effect to demonstrate a silicon light source is a possibility. The only major problem in using PhC cavities is the reduction of the G-line intensity due to the etched side walls. The G-line intensity becomes extremely low before coupling with the cavity. To get the maximum advantage of Purcell effect, it is necessary to solve this problem.

I suggest the following two routes as future experiments to solve this problem:

1. Use surface passivation techniques such as low temperature annealing to passivate the etched side walls of the PhC holes and hence increase the carrier lifetime. The carrier lifetime at the etched side walls are in the sub-ns regime while the G-line lifetime is in µs range. Surface passivation techniques might not be successful to fill this large difference.
2. Alternatively, a different device design can be used, where the silicon layer containing the G-centres is not etched and therefore not disturbed. Instead, a cavity is defined on top of the silicon layer. I propose the following two configurations:
    i. Strip loaded silicon waveguide configuration.
    ii. Creating ring resonators in an amorphous-Si layer deposited on top of G-centre containing layer of SOI.

i. Strip loaded silicon waveguide configuration

Polymer waveguides, such as SU-8, can be defined on top of the silicon layer to form strip loaded waveguides, with the mode residing in the silicon slab which contains the G-centre, as shown in Figure 6.8. 1-2 μm wide waveguides were fabricated on the C-implanted SOI.

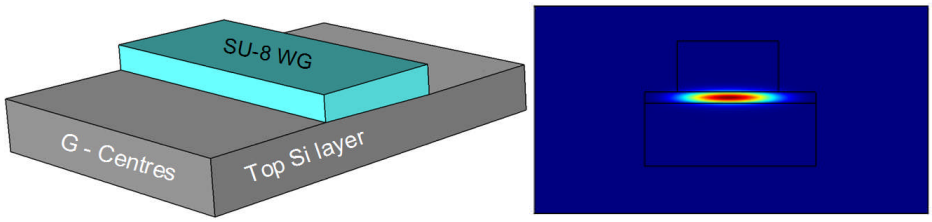

(a) (b)

Figure 6.8: Schematic of strip loaded silicon waveguide containing G-centres (a) with its mode profile (b).

The losses of the waveguides were measured to be only 1.4 dB/cm. This low loss indicates that there is a possibility of observing a gain in the G-centre containing silicon if a cavity is created. The cavity could be formed in the strip loaded waveguide configuration by etching Bragg mirrors at the ends. A schematic of such a proposed design is shown in Figure 6.9.

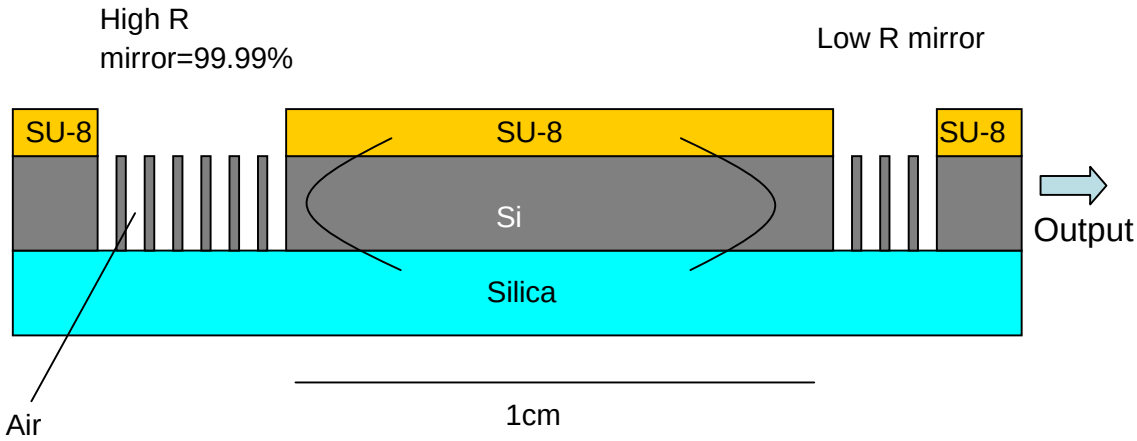

Figure 6.9: Schematic of the proposed design. The strip loaded waveguide provides lateral confinement while the Bragg mirrors form a cavity.

The Bragg mirrors are designed to have a reflectance band centred at the G-line wavelength. This is achieved by using 25 layers of low (air) and high (Si) refractive index with a period of 355 nm, a Si width of 100 nm and air gap of 255 nm width. As the index contrast between the two layers is quite high, a few layers are already sufficient to achieve high reflectance. The output mirror should have lower reflectance to enable the output of light. This can be achieved by reducing the number of layers. The reflectance band of the designed mirror is shown in the figure below (Fig. 6.10 (a)), calculated by using the transfer matrix method (TMM), with 2D FDTD simulation showing the high reflection at 1280 nm, Figure 6.10(b).

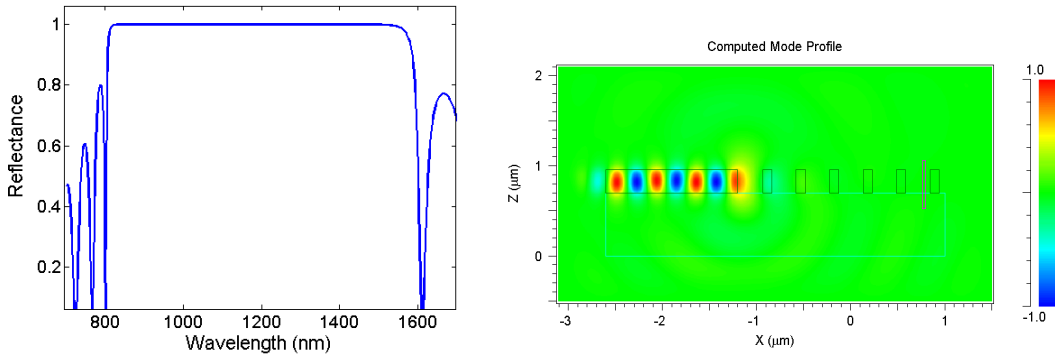

(a) (b)

Figure 6.10: Bragg mirror designed to reflect the G-line. (a) The reflectance of the mirror. (b) FDTD simulation showing the reflectance of the field at 1280 nm.

Gain requirement for lasing

The amount of gain required in this system to observe lasing can be calculated using the following equation:

$$\alpha\Gamma + \frac{2\pi n_{eff}}{\lambda Q} = g\Gamma$$

Equation 6.1

where α is the waveguide loss, Γ the mode confinement factor, g the gain and Q the quality factor of the cavity.

Considering each mirror reflectance as 0.95, then the Q-factor for a 1 mm long cavity would be 270,000. The value of Γ was calculated to be 0.95 by using the commercial

software Fimmwave, while the loss of the waveguide was measured experimentally as 1.4 dB/cm.

Using these values in Equation 6.1, the gain required for lasing is calculated to be as follows:

2.83 dB/cm for 1 mm cavity

8.3 dB/cm for 100 μm cavity

1.56 dB/cm for 1 cm cavity

The fabrication and gain measurements of this proposed system will be carried out in the future.

ii. Amorphous silicon ring resonator on top of SOI

The scheme proposed above is promising but does not achieve the advantage of emission enhancement via the Purcell effect. To increase the G-line emission by utilizing the Purcell effect, a ring resonator can be created on top of the silicon layer of SOI containing the G-centre, as shown in Figure 6.11, instead of etching the layer itself. This would prevent the quenching of the G-line due to etching.

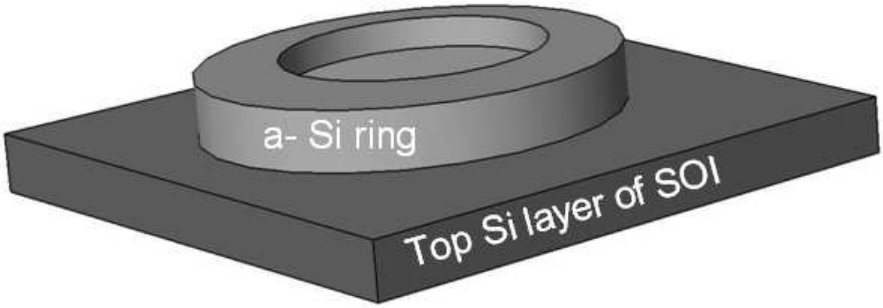

Figure 6.11 Schematic of the proposed scheme. An amorphous silicon ring resonator could be defined on top of the SOI containing the G-centres.

Depositing a layer of amorphous silicon on top of the SOI and etching this layer to form the ring cavity can achieve this. A suitable ring resonator can be designed to have a resonant coupling to the G-line. This approach would benefit from the emission enhancement by exploiting the Purcell effect and could lead to the development of an efficient silicon light source.

6.5 Conclusions

An interaction between the cavity and the G-line emission is observed experimentally, which gives an indication of the presence of the Purcell effect. Due to the etching of silicon, the G-line intensity is reduced dramatically, most probably due to the creation of non-radiative defect sites or the displacement of substitutional carbon atoms. For this reason, the route of coupling the G-line with the PhC cavity could not utilize the full benefit of the Purcell effect. The use of G-line emission to develop a silicon light source could still be promising if the problem of G-line quenching by the etching of silicon could be addressed. For this purpose, two different proposals as a subject of future research have been presented.

References

[1] N-T. Satoko, T. Michio, H. Kazuyuki, O. Takeshi, and I. Hisayoshi, "Characterization of light element impurities in ultrathin silicon-on-insulator layers by luminescence activation using electron irradiation," Jpn. J. Appl. Phys. 48, 031201 (2009).

[2] N. A. Drozdov, A. A. Patrin, and V. D. Tkachev, "Recombination radiation on dislocations in silicon," Pisma Zh. Eksp. Teor. Fiz. 23, 651-653, Sov. Phys. JETP Lett. 23, 597-599 (1976).

[3] J. Bao, M. Tabbal, T. Kim, S. Charnvanichborikarn, J. S. Williams, M. J. Aziz, and F. Capasso, "Point defect engineered Si sub-bandgap light-emitting diode," Opt. Express 15, 6727-6733 (2007).

[4] G. Davies, K. Tat Kun, and T. Reade**.,** "Annealing kinetics of the dicarbon radiation-damage center in crystalline silicon," Phys. Rev. B 44, 12146–12157 (1991).

[5] S. G. Cloutier, P. A. Kossyrev, and J. Xu, "Optical and stimulated emission in periodic nanopatterned crystalline silicon," Nat. Materials 4, 887 (2005).

[6] L. Song, X. Zhan, B. Benson, and G. Watkins, "Bistable interstitial–carbon–substitutional–carbon pair in silicon," Phys. Rev. B 42, 5765 (1990).

[7] G. Davies, "The optical properties of luminescence centres in silicon," Phys. Rep. 176, 83–188 (1989).

[8] J. Weber and M. Singh, "New method to determine the carbon concentration in silicon," Appl. Phys. Lett. 49, 1617 (1986).

[9] K. Murata, Y. Yasutake, Koh-ichi Nittoh, S. Fukatsu, and K. Miki, "High-density G-centers, light-emitting point defects in silicon crystal," AIP Adv. 1, 032125 (2011).

[10] E. Rotem, J. M. Shainline, and J. Xu, "Stimulated emission and emission efficiency enhancement in nano-patterned silicon," Proc. SPIE 6775, 67750I (2007).

[11] T. Tanabe, M. Notomi, S. Mitsugi, A. Shinya, and E. Kuramochi, "All-optical switches on a silicon chip realized using photonic crystal nanocavities," Appl. Phys. Lett. 87, 151112 (2005).

Chapter 7

Erbium based silicon light source

The emission of erbium ions at 1.54 μm and their successful use in silica fiber amplifiers has made erbium an interesting candidate as a dopant in silicon to increase silicon's sub-bandgap light emission. As discussed in detail in Section 1.3.2, a number of efforts have already been made in this regard, but the thermal quenching of emission and low solubility of erbium in silicon which gives rise to a low emission level, has hindered its progress. In Chapter 3, successful results on the enhancement of sub-bandgap defect luminescence in silicon along with the achievement of temperature stability via the Purcell effect have been presented. In the present chapter, the possibility of using the same approach, i.e. the Purcell effect, to enhance the emission from erbium doped silicon is investigated. For these investigations, photonic crystal L3 cavities were fabricated on erbium doped silicon. An alternate approach, in which a layer of erbium disilicate is deposited on top of L3 PhC cavity has also been pursued and is presented in this chapter.

7.1 Erbium doping in SOI

The first step in developing a light source in erbium doped silicon is to have a high erbium doping concentration, which is difficult to achieve as erbium has poor solubility in silicon. The maximum erbium concentration achieved by ion implantation is 3×10^{17} cm^{-3} [1]. Increasing the concentration further causes erbium to precipitate and form optically inactive clusters [2,3]. This problem can be solved to some extent by co-doping with other impurities such as oxygen, nitrogen, carbon or fluorine [4-6]. Erbium acts as a donor in silicon, thus erbium emission also depends on whether the silicon layer is p-type or n-type. A high n-doped silicon material would also enhance the non-radiative Auger processes and reduce the emission. In contrast, this effect is lesser in p-doped material because the presence of acceptors increases the probability of electron-hole recombination compared to electron getting lost via Auger recombination. Thus, it is better to use p-doped SOI. In our experiments, a slightly p-doped (1×10^{15} B/cm^3) SOI was used. The erbium was co-doped with oxygen, as shown in the schematic in

Figure 7.1, by using ion implanter. The implantation was followed by thermal annealing at 900 ^{o}C for 30 min to activate the ions.

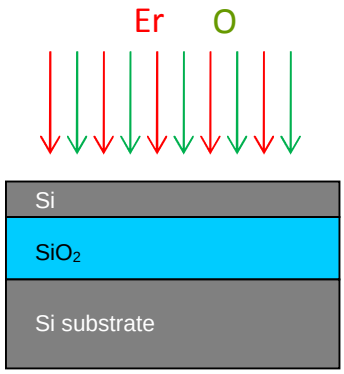

Figure 7.1: Co-doping erbium with oxygen into top silicon layer of SOI.

Different ion implantation conditions (dose of erbium and oxygen) were used to optimize the implantation conditions to achieve the highest possible emission from the doped SOI. The PL from erbium doped SOI, co-doped with oxygen for different doping doses is shown in Figure 7.2(a). We found out that an oxygen dose of $5x10^{13}$ O/cm^2 combined with an erbium dose of $1x10^{13}$ Er/cm^2 gave the highest PL level. The resulting concentration of oxygen at these doping conditions ends up as $5x10^{18}$ O/cm^3 . Increasing the oxygen concentration further reduces the PL intensity, as shown in Figure 7.2(b).

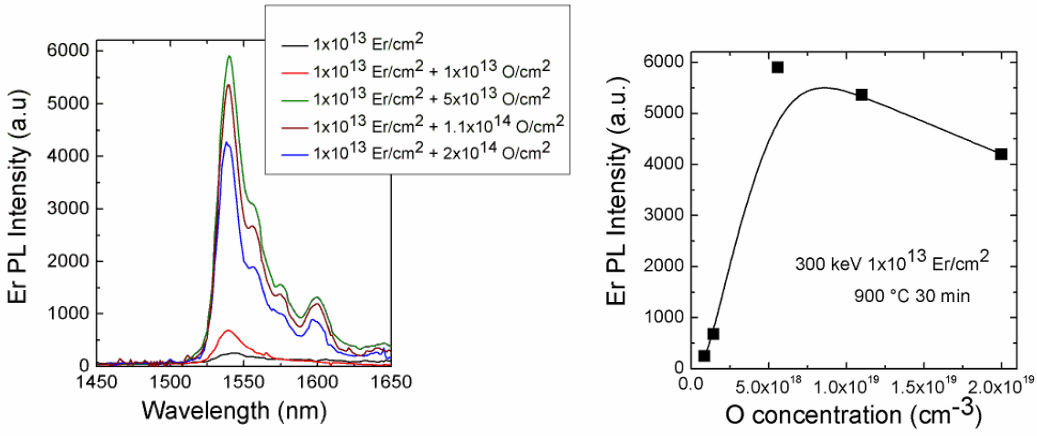

(a) (b)

Figure 7.2: (a) PL intensity from erbium doped SOI co-doped with different oxygen doses. (b) PL intensity for different oxygen concentrations in silicon. The PL decreases for oxygen concentrations higher than $5x10^{18}$ O/cm^3.

The doping profiles for erbium and oxygen are given in Figure 7.3. Oxygen was doped at 40 keV while erbium at 300 keV to have the maximum doping concentration at the same depth. The curves for oxygen are simulations while the doping profile of erbium was measured experimentally by secondary ion mass spectroscopy (SIMS).

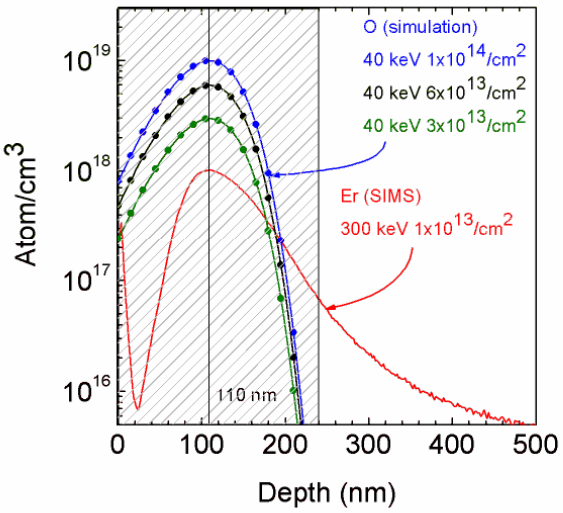

Figure 7.3: Erbium doping profile for different doping conditions (courtesy of Dr Giorgia Franzò, University of Catania).

7.2 Erbium doped photonic crystal cavities

L3 photonic crystal cavities with fundamental resonance wavelengths around 1.54 µm were fabricated on an SOI wafer, doped with the most optimized doping conditions, i.e erbium doping at 300 keV with a dose of $1x10^{13}$Er/cm^2 co-doped with oxygen at 40 keV with a dose of $5x10^{13}$ O/cm^2. The low temperature PL measurements of these samples were taken by the µPL setup at the University of Pavia. The PL spectra of the erbium doped L3 PhC cavity are shown in Figure 7.4.

For the enhancement of erbium emission via the Purcell effect, it is necessary to match the fundamental mode of the cavity at the erbium emission wavelength (1538 nm). Although the cavity is designed to have its fundamental resonance at the erbium emission wavelength, it is not possible to control the resonance with nanometer

accuracy. Thus, a post fabrication tuning of the cavity resonance is essential to exactly match the cavity resonance with the erbium emission.

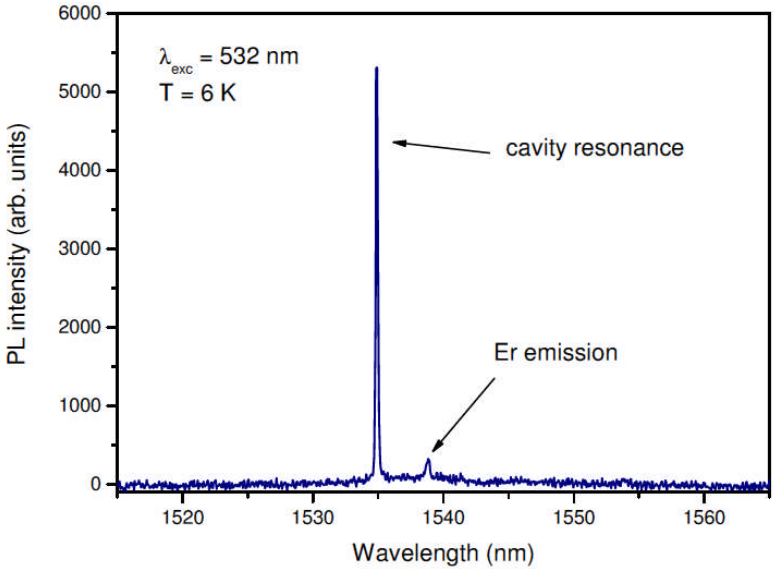

Figure 7.4: PL spectra of erbium doped L3 PhC cavity. The peak at 1535 nm is the L3 fundamental mode, with the emission line due to optically active hydrogen related defects feeding the cavity. The small peak at 1538 nm is the erbium emission.

A technique called “gas tuning” [7] was used as a post fabrication method for tuning the resonance wavelength of PhC cavity. In this method, nitrogen gas is introduced into the cryostat, which condenses on top of the PhC cavity, thereby slightly changing the refractive index and increasing the resonance wavelength of the cavity. With this method, the resonance wavelength can be controlled accurately, as shown in Figure 7.5. Thus, by combining lithographic tuning and post fabrication gas tuning, full control over the cavity resonance wavelength is achieved.

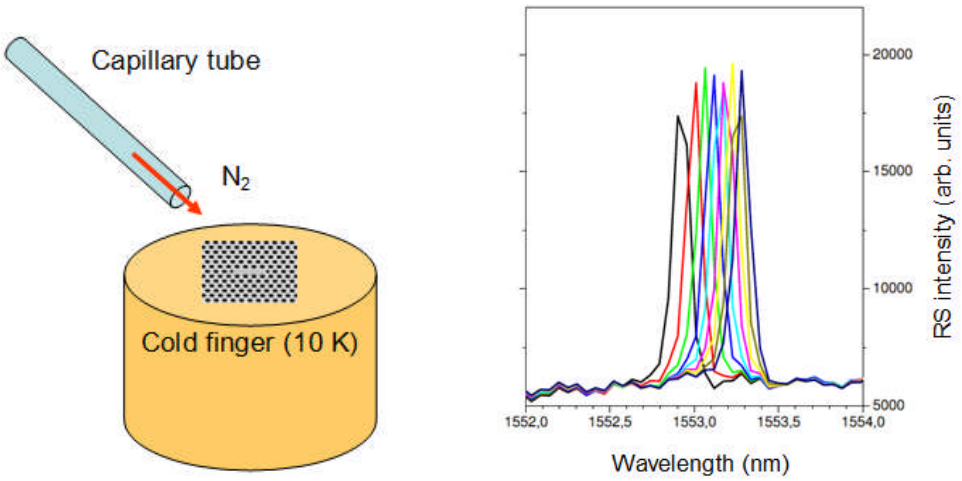

(a) (b)

Figure 7.5: Gas tuning to shift the resonance wavelength of L3 PhC cavity. (a) The method. (b) The colored lines show the fine tuning of the resonance wavelength by condensed nitrogen.

7.3 Lack of erbium-cavity interaction

Combining lithographic and gas tuning, the spectral overlap of the cavity and the erbium emission was achieved. Unfortunately, it was observed that the emission signal does not increase resonantly but instead, the two emission lines (defect emission line and erbium line) only add up, as shown in Figure 7.6. Thus, there is no apparent interaction between the cavity and the erbium and hence no Purcell effect. The absence of the Purcell effect can be proven by comparing the time resolved PL of the erbium doped PhC cavity at off- and on-resonance conditions. From time resolved PL measurements, the lifetimes of erbium emission at off- and on-resonance were measured to be 0.93 and 0.85 ms, respectively, as shown in Figure 7.7 (a,b). Thus, there is only a very small change in the lifetime for the two conditions, indicating the absence or presence of only a very weak Purcell effect.

In addition to the slow decay, the time resolved PL measurements show a component with a very fast decay, which could not be resolved by our setup. The upper lifetime limit of this fast decaying component is 100 ns, i.e. the limit of the setup. This component is probably the hydrogen defect luminescence, which has a very short lifetime, as discussed in Section 3.5.1.5 in Chapter 3.

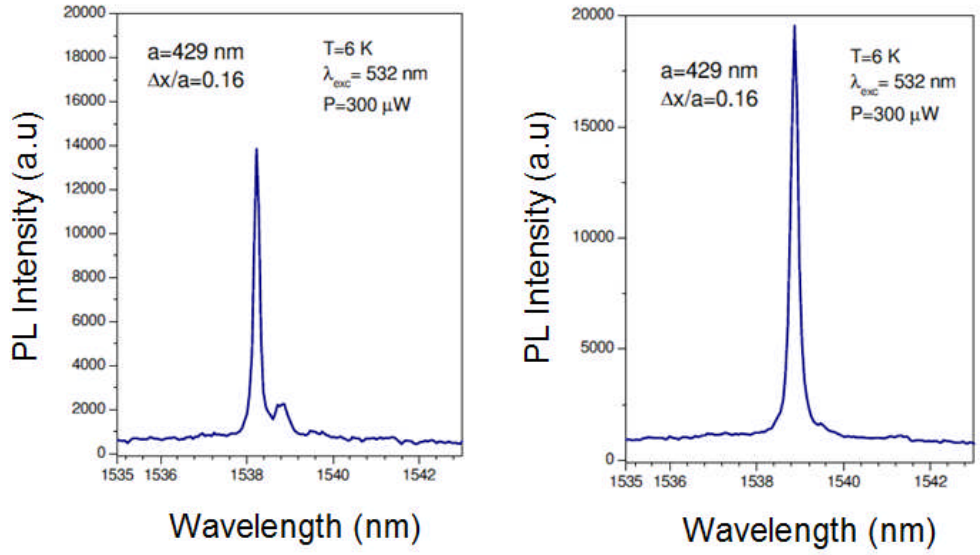

(a) (b)

Figure 7.6: Lack of cavity-erbium interaction. (a) Cavity resonance not matched with erbium emission. (b) Gas tuning to match the cavity resonance exactly with the erbium emission. Even when spectral overlap is achieved, there is no resonant interaction between the erbium emission and the cavity.

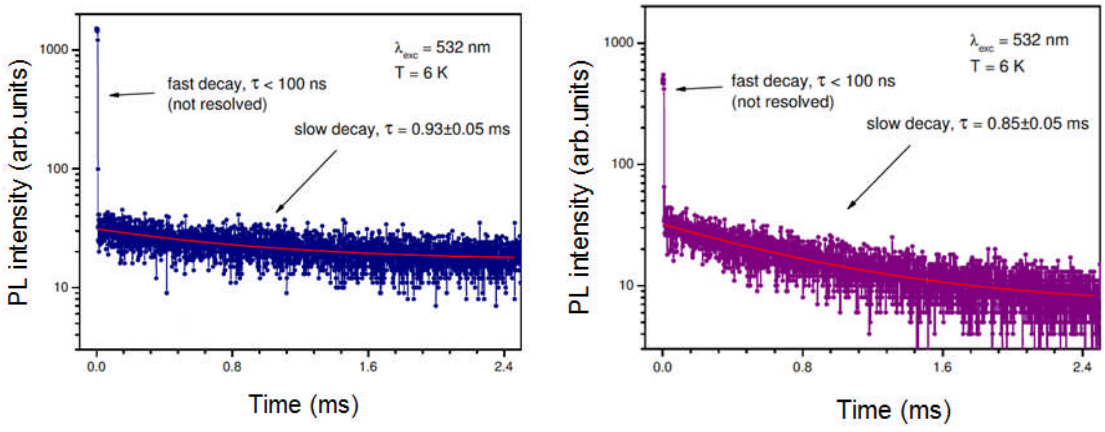

(a) (b)

Figure 7.7: Time resolved PL measurements of an erbium doped PhC cavity at off-resonance (a) and on-resonance conditions (b). There is only a small change in the lifetime for the two cases. The fast decay component is due to defect luminescence.

7.3.1 Reasons for the lack of cavity-erbium interaction

We suggest the following three possible reasons for the lack of cavity-erbium interaction:

1. The cavity line is much narrower than the erbium emission.
2. Lack of active erbium ions in the cavity area.
3. High background emission

Evidence for the first reason is depicted in Figure 7.8. The cavity line is narrower than 0.1 nm, while the FWHM of erbium emission is more than 10 nm. Thus, only a very small amount of erbium emission feeds into the cavity.

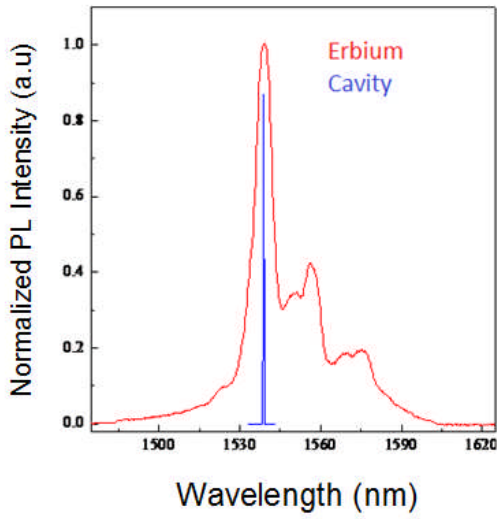

Figure 7.8: Cavity linewidth is much narrower than the erbium emission, which causes the lack of interaction.

The second reason is due to the low erbium concentration. Furthermore, only small fraction of these ions is expected to be optically active. Thus, the lack of active erbium ions in the cavity area can be one of the main reasons of lack of Er-cavity interaction.

Thirdly, there is a strong background emission due to hydrogen defects, shown in Figure 7.9 and discussed in Chapter 3, which competes for the carriers. To increase the coupling of the cavity modes with the erbium transition, removing this competing recombination route will be very beneficial.

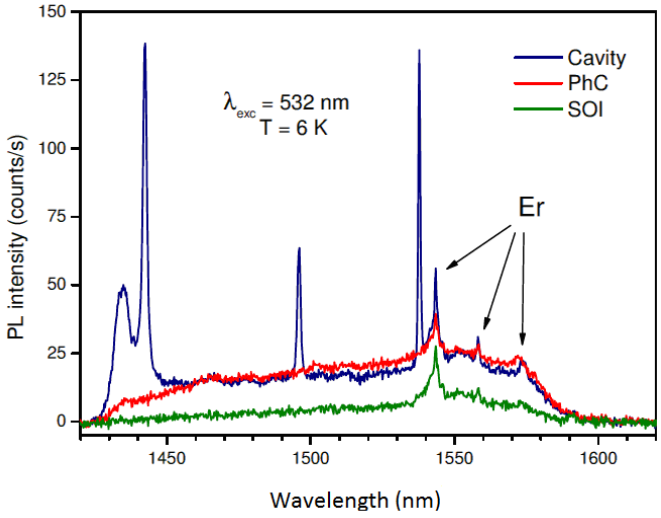

Figure 7.9: Strong background defect emission, detrimental for the erbium-cavity coupling.

As we have already reached the maximum erbium concentration, it is not possible to increase the amount of erbium ions further as it would form optically inactive clusters. The use of a low Q cavity would increase the cavity linewidth to match the erbium emission but using a cavity with very low Q-factor would not offer high emission enhancement via the Purcell effect. Thus, we do not see how the above problems can be solved at this point and conclude that the approach of enhancing erbium emission by coupling it with a PhC cavity is not successful.

7.4 An alternate approach: Er-Y disilicate layer on top of PhC cavity

Next, we explored an alternative approach for Purcell enhancement. The idea is to deposit a thin layer of an erbium-containing compound on top of the PhC cavity; the trade-off is much higher erbium solubility against reduced mode overlap. We used yttrium-erbium disilicate film with the chemical formula $Y_{2-x}Er_xSi_2O_7$, where $0 < x \leq 2$ or more conveniently expressed as Y-Er.

Using Y-Er disilicate film has the following advantages:

1. Yttrium is optically inactive and thus, the optical properties of the compound only depend on the optically active erbium.

2. By using Y-Er, an erbium doping concentration as high as 10^{22} Er/cm^3 can be achieved. Thus, the problem of low solubility is solved.
3. Using Y-Er, luminescence and internal gain in ridge waveguides has already been demonstrated, indicating its potential for developing a light source [8-10].
4. Room temperature operation, as is well known from erbium doped fiber amplifiers.

7.4.1 Deposition of Y-Er disilicate layer on PhC cavity

For the experiments, an air-bridge L3 PhC cavity was used. In order to ensure that we could match the cavity resonance with the erbium emission, we again used very tight lithographic tuning range, i.e. from 405 nm to 430 nm, with a step of 1 nm, while keeping the fill factor, r/a, constant at 0.275. Similar to the design used in the previous chapters, the holes adjacent to the cavity were reduced in size and moved laterally outwards to increase the Q-factor of the cavity. Far-field optimization was added to increase the vertical out-coupling of light. Three (Δr=0, +6 nm and +21 nm) values for the far-field optimization were used.

A 10 nm layer of Y-Er disilicate film was deposited on top of the cavity by using magnetron sputtering in an ultrahigh vacuum chamber. Three targets, Er_2O_3, Y_2O_3 and SiO_2 arranged in a confocal geometry were co-sputtered to produce the required thin film of Y-Er disilicate. The sample temperature was maintained at 400 ^oC throughout the deposition process. After deposition, the sample was annealed at 1250 ^oC for 30 s in an O_2 environment. This high temperature annealing serves two purposes: crystallization of the deposited film and reduction of non-radiative recombination sites to increase the emission of erbium ions present in the film [8,11]. The composition of the deposited film was determined by Rutherford back-scattering spectroscopy, resulting in $8x10^{20}$ Er/cm^3 (1.2 atm %) and disilicate-like stochiometry ([Y+Er]: [Si]:[O]=2:2:7) of the film. (Deposition and characterization of Y: Er film: courtesy of Dr Maria Miritello, University of Catania).

The schematic of the device and an SEM image of the L3 PhC cavity after deposition of 10 nm layer of Y-Er are shown in Figure 7.10.

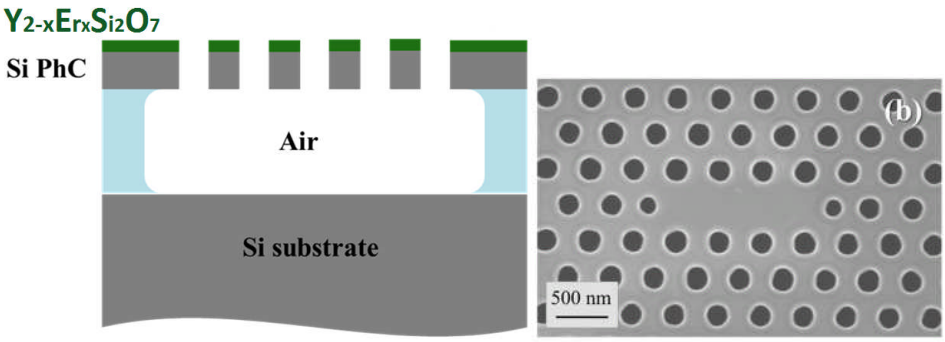

(a) (b)

Figure 7.10: (a) Schematic of the PhC cavity coated with Y-Er disilicate film, (b) SEM image (top view) of L3 PhC cavity with 10 nm Y-Er layer deposited on the top.

7.4.2 Emission characteristics

The PL of the sample was measured in the µPL setup, explained in detail in Section 2.3.2. A pump wavelength of 980 nm was used, which is resonant with the erbium transition from the ground state to the second excited state, $I_{15/2}$ to $I_{11/2.}$ Following excitation, the atoms first undergo a quick non-radiative transition from $I_{11/2}$ to $I_{13/2.}$ This is then followed by the radiative transition to the ground state, accompanied by the emission of photons at 1.54 µm wavelength. The PL spectra of the Y-Er disilicate film deposited on the unpatterned SOI and on the L3 PhC cavity (on-resonance) are shown in Figure 7.11.

The black dashed line corresponds to the PL spectrum of the film deposited on unpatterned SOI while the spectra with the sharp peaks are obtained when the emission is on resonance with the cavity. As shown in Chapter 3, the cavity has seven modes in total, but only the fundamental mode is shown in Figure 7.11 for different lattice periods for a fixed far-field parameter of 6 nm. The peaks are superimposed on a weak background, which is the emission of erbium ions present in the Y-Er film. The emission intensity of the peaks follows the background emission level and shifts towards longer wavelengths with increasing lattice constant, as shown in Figure 7.11.

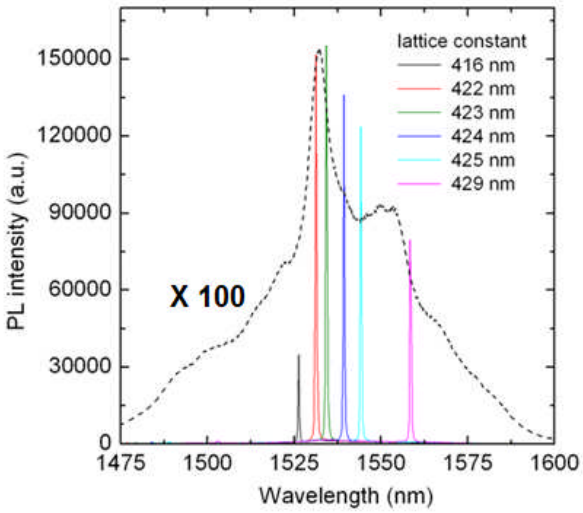

Figure 7.11: PL spectra of Er-Y layer deposited on top of unpatterned SOI (black curve) and on PhC cavities of different lattice constants for a fixed far-field optimization parameter of 6 nm. The peaks show the fundamental emission line of the cavities having different lattice constants. The background emission level is multiplied by 100 to match the cavity peak level.

As expected, the emission intensity from the far-field optimized cavities is higher than from the un-optimized ones but at the expense of linewidth broadening, as shown in Figure 7.12.

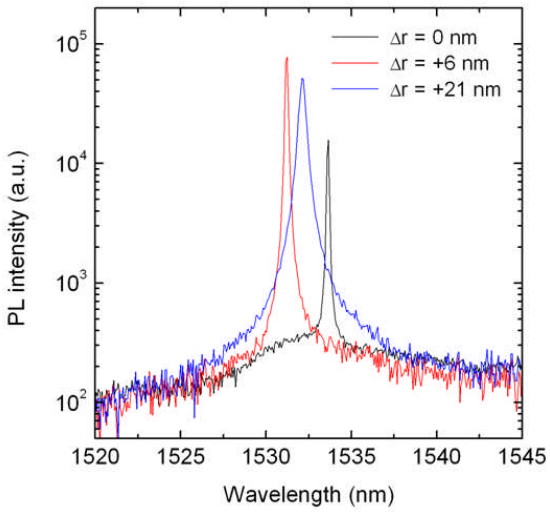

Figure 7.12: Cavity resonance enhances the erbium emission intensity by two orders of magnitude over the background.

The Q-factors measured by the RS method [12] for the three values of far-field optimization parameters (Δr=0, +6 nm and +21 nm) were 26000, 16200 and 4000, respectively. By taking the peak to background ratio, it is clear that the erbium emission level increases by 2 orders of magnitude by coupling it on resonance with the cavity. This enhancement is consistent with the values achieved with the cavity-enhanced band-edge and defect luminescence [13,14].

The output emission intensity for increasing pump powers was measured to investigate the maximum possible emission. It was found out that the emission intensity increases up to a pump power of 6 mW, after which it saturates. Further increases in pump power then decrease the output intensity, as shown in Figure 7.13. The emission levels are normalized as indicated in the legend of the figure for better comparison.

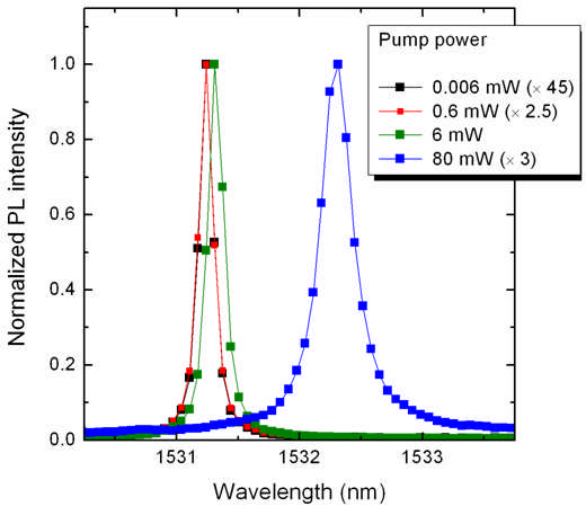

Figure 7.13: Peak PL intensity for different pump powers. The PL intensity is normalized with the multiplication factors shown in the legend.

In addition to a decrease in the emission intensity with pump powers higher than 6 mW, the emission line also red shifts and becomes broader. The red-shift is due to heating. Increasing the pump power from 6 mW to 80 mW red shifts the peak by 1 nm, which corresponds to an increase of the sample temperature by 20 ^{o}C. The broadening of the linewidth is due to the increase in the free carrier absorption in silicon, which reduces the Q-factor of the cavity. In fact, a higher percentage of light is absorbed in silicon rather than by the erbium atoms. Considering the erbium absorption cross section of 10^{-21} cm^2 [15], it is estimated that only $8x10^{-5}$ % of the incident photons are

absorbed by the erbium, while 0.2 % are absorbed by the silicon underneath it. Thus, there is a limit, as higher pumping leads to heating effects, free carrier absorption and reduction of the PL signal due to detuning from the maximum emission point on the erbium emission spectrum. The effect of pump power on the Q-factor and the resonance wavelength of the cavity are shown in Figure 7.14. From this figure, it is clear that the Q-factor and the resonance position of the cavity are almost unchanged up to 12 mW pump power. Increasing the pump power further drastically changes these values and thus for the present sample, the maximum pump power is limited to 12 mW.

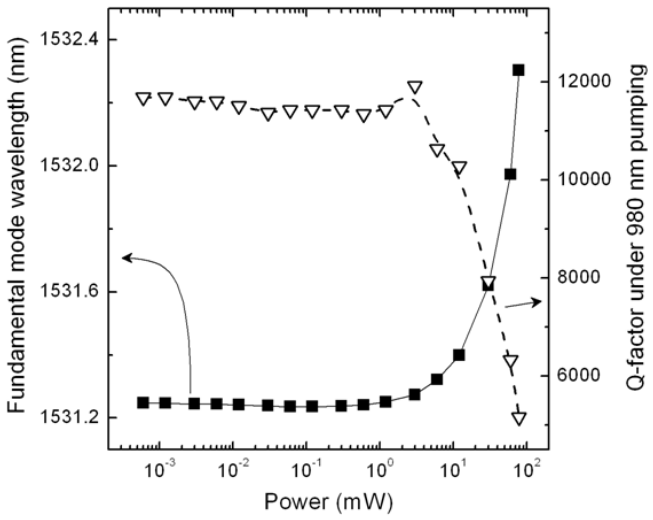

Figure 7.14: Cavity Q-factor and resonance wavelength versus pump power.

7.4.3 Output power and efficiency

The maximum output power was measured by an InGaAs power meter. The photons below 1500 nm were removed with a low pass filter, so that any contribution not from erbium could be eliminated. The total collected power of the cavity peak was estimated to be 85 pW for 12 mW input power. This value was obtained after normalizing the measured value to account for different loss mechanisms, such as the absorption in the setup, the fraction of light emitted vertically and the background emission.

As mentioned above, only 8×10^{-5} % of incident light is absorbed by erbium. Thus, of 12 mW incident power, only 9.6 nW are absorbed in erbium which in turn emits 85 pW of light. Thus, the efficiency is 0.9 % for 12 mW pump power and higher for lower

pumping power, considering the sub-linear trend of the output power against the input power, shown in Figure 7.15 by black filled circles. The resulting 0.9 % efficiency is quite remarkable for a silicon light source.

7.4.4 Estimation of excited erbium atoms

The percentage of the excited erbium atoms for a given pump power can be estimated from the output power and by considering that each erbium atom emits a power of $1.3\text{x}10^{-19}/\tau$ watts, where τ is the on-resonance emission lifetime. The total number of excited atoms can be found from the ratio of total emitted power to the power emitted by a single atom. Using 85 pW as the total output power for 12 mW input power and on-resonance lifetime value of 2.1 ms (measured experimentally and explained in the next section), the total number of excited erbium atoms are estimated to be $1.4\text{x}10^{6}$. Considering that the erbium atoms occupy the entire 10 nm thickness of erbium disilicate layer and the cavity area is 1 μm^2, the concentration of the excited erbium atoms in the cavity area would be $1.4\text{x}10^{20}/cm^3$. As mentioned in Section 7.4.1, the total erbium concentration in the Y-Er layer is $8\text{x}10^{20}/cm^3$, thus the percentage of the excited erbium atoms in the cavity area is 17 %.

The rate equation for the first excited erbium level is given below. A two level approximation has been used in this equation by assuming that all the atoms resonantly excited to $^4I_{11/2}$ level are de-excited immediately to $^4I_{13/2.}$

$$\frac{dN_1(t)}{dt} = \sigma\phi\left(N_{Er} - N_1(t)\right) - \frac{N_1}{\tau} - C\left[N_1(t)\right]^2 \qquad \text{Equation 7.1}$$

In this equation C is the upconversion parameter. Since the PL trend, as shown in Figure 7.14, is sub-linear, upconversion occurs, which depletes the first excited level. For this reason, the upconversion process has been included in the rate equation. The value of C is $1.3\text{x}10^{-16}$ cm^3/s, obtained by extrapolating the values reported in reference [16].

The other terms appearing in the equation are defined as follows:

$N_1(t)$ Erbium population in the first excited level ($^4I_{13/2}$) at a certain time t

σ Erbium excitation cross section having value $1\text{x}10^{-21}cm^2$ at 980nm. Value taken from [15].

ϕ Pumping flux

N_{Er} Atomic concentration of erbium

For the steady state condition reached under CW pumping, we can describe the excited erbium population as a function of pumping flux $N_1(\phi)$ with the following equation.

$$N_1(\phi) = \frac{1}{2C\tau}\left[\sqrt{1+\sigma\phi\tau\left(2+4CN_{Er}\tau+\sigma\phi\tau\right)} - \left(1+\sigma\phi\tau\right)\right] \qquad \text{Equation 7.2}$$

Substituting all the values listed above, N_1 (ϕ) can be plotted, which is shown in Figure 7.15 (red curve). The curve matches well with the experimental data.

Considering the population inversion threshold as 50 % of the excited erbium population, shown by the horizontal green line in Figure 7.15, it can be inferred that population inversion could be achieved for pumping levels higher than 12 mW. Unfortunately, as discussed above and shown in Figures 7.14 and 7.15, it is not currently possible to increase the pump power above 12 mW under the present conditions as it creates the problem of free carrier absorption and heating effects, which in turn reduces the emission level.

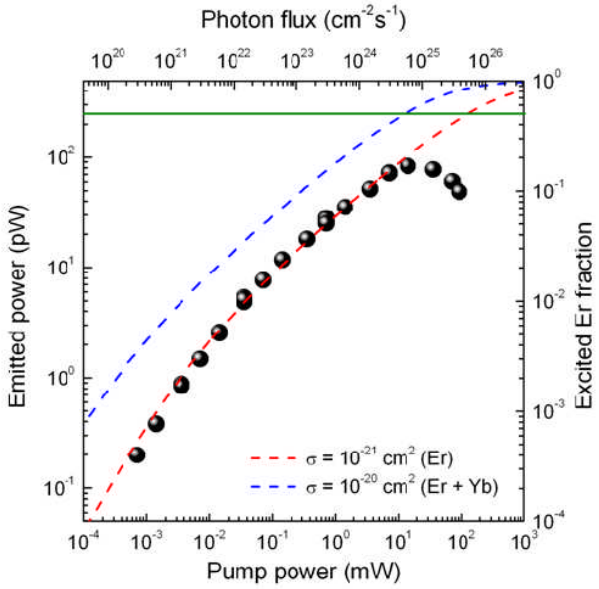

Figure 7.15: Output power vs. pump power (black balls). The excited erbium fraction as a function of pumping flux is shown for Y-Er (red curve) and for Yb-Er (blue curve). The horizontal green curve shows the population inversion threshold (50 % of excited erbium atoms), which could be achieved at 12 mW for Yb-Er but requires higher power levels for the Y-Er used here.

It might be possible to achieve population inversion by taking the following two routes:

1. Use 1480 nm pumping wavelength. This would reduce the absorption in silicon and hence reduce the free carrier absorption, allowing us to pump at higher powers.
2. Replacing yttrium (Y) with ytterbium (Yb) can increase the population of excited erbium ions. This is because, the excitation cross section of Yb is an order of magnitude higher than that of Y [17,18], which leads to the higher luminescence power shown in Figure 7.15. If we would use Yb, the population inversion could be achieved with 12 mW pump power, which we will explore in further work.

7.4.5 Estimation of the Purcell factor

As discussed earlier in Chapter 3, the Purcell factor can be estimated via the change in the lifetime when the emitter is on resonance with the cavity [19]. For this purpose, time resolved PL measurements were carried out at room temperature on the μPL setup at University of Pavia. The signal from the pump was mechanically chopped at 30 Hz. The emitted light collected from the sample was fed into a super conducting single photon detector (SSPD), which was cooled to 4.2 K. Time correlated single photon counting was used to record the lifetime. Figure 7.16 gives the time resolved PL of erbium when on-resonance with the cavity (black curve) and off-resonance (red curve). The signal was collected only from a wavelength range of 1500-1800 nm with the rest filtered out. The lifetime values were extracted by fitting the decay curves with the solution of Equation 7.1 for t=0 and thus φ=0, leading to the following equation:

$$\frac{I_1(t)}{I(0)} = \frac{1}{\left(1 + N_1(0)C \times \tau\right)e^{-\frac{t}{\tau}} - N_1(0)C \times \tau} \qquad \text{Equation 7.3}$$

The fitting parameters are τ and $N_1(0)C$. The fitting is shown in Figure 7.16 with the green dotted line, giving the lifetime value of 2.1ms for the on-resonance case. The extracted lifetime is 3 ms when the erbium emission is not coupled with the cavity. By using these values, the Purcell factor can be estimated as follows.

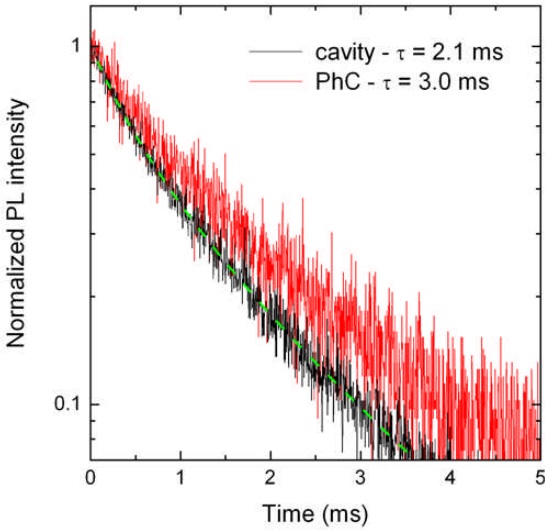

Figure 7.16: Time resolved PL of erbium on-resonance with the cavity (black curve) and off-resonance (red curve).

The decay rate of erbium in the absence of Purcell effect (off-resonance with the cavity) can be expressed in terms of radiative and non-radiative lifetimes as follows:

$$\left(\frac{1}{\tau}\right)_{PhC} = \frac{1}{\tau_R} + \frac{1}{\tau_{NR}} \qquad \text{Equation 7.5}$$

and in the presence of Purcell effect (on-resonance) as

$$\left(\frac{1}{\tau}\right)_{cavity} = \frac{1}{\frac{\tau_R}{F_p}} + \frac{1}{\tau_{NR}} = \frac{F_p}{\tau_R} + \frac{1}{\tau_{NR}} \qquad \text{Equation 7.6}$$

Assuming that the non-radiative lifetime in both cases is the same, Equations 7.5 and 7.6 lead to the following equation of Purcell factor:

$$F_p = \left[\left(\frac{1}{\tau}\right)_{cavty} - \left(\frac{1}{\tau}\right)_{PhC}\right]\tau_R + 1 \qquad \text{Equation 7.7}$$

The value of the radiative lifetime is calculated by using the values reported in reference [20] for erbium in Y_2O_3. Since the radiative lifetime of erbium only depends on the refractive index of the host material and has an inverse square relationship with it [21], this value can be used to extract the erbium radiative lifetime in Y-Er. Y_2O_3 has a refractive index value of 1.9 and the erbium radiative lifetime is 8 ms. Thus, the radiative lifetime in Y-Er is around 9 ms. Using this value and the lifetime values

calculated from the decay curves (2.1 ms for on-resonance with the cavity and 3 ms for off-resonance) in Equation 7.7, the Purcell factor we obtain is 2.2. The experimentally calculated Purcell factor is very close to the theoretically calculated value of 3.2. (Theoretical calculation of Purcell factor credit to Dr Dario Gerace, University of Pavia).

7.5 Future work - Emission enhancement by increase of Purcell factor

The major shortcoming in the device presented in this chapter is the low overlap of the cavity mode with the active medium. The emitters are placed on top of the cavity while the maximum modal field is in the center of the silicon slab. This causes very low interaction of the emitters with the cavity, leading to the weak Purcell enhancement. The overlap factor between the cavity mode and the emitting dipole can be described as follows:

$$\Gamma = \frac{\int_{\Omega} |E(r)|^2 dr}{\int |E(r)|^2 dr} \qquad \text{Equation 7.8}$$

Here Ω is the active volume, while integral in the denominator extends to the whole 3D space.

The efficiency of the device can be improved by increasing the overlap factor. This can be achieved by using slotted PhC cavities, where the electromagnetic field E is concentrated in the air slot rather than in the silicon, as discussed in Section 5.2, Chapter 5. On deposition, the active Y-Er layer will penetrate the slot region of the PhC cavity and have a better overlap with the cavity mode, offering higher Purcell enhancement and hence higher output emission power.

7.6 Conclusions

From the work in this chapter, I conclude that depositing a thin layer of Y-Er disilicate on top of a L3 PhC cavity to create a silicon light source is successful. The high concentration ($8x10^{20}$ Er/cm^3) of active erbium ions in Y-Er enables the Er-cavity interaction to gain the advantage of the Purcell effect. From time resolved PL

measurements, a value of 2.2 is extracted for the Purcell factor, which is close to a theoretically calculated value of 3.2. Using this approach, a silicon light source emitting at 1.54 μm is demonstrated at room temperature with 85 pW power. To increase the performance of the device, two proposals for future research are given. The first is to use Yb-Er, which has an order of magnitude higher excitation cross section compared to Y-Er. The second is to increase the overlap between the emitting dipole and the cavity mode by using a slotted PhC cavity.

I also conclude that an approach to use a PhC cavity in erbium doped silicon is not successful because of the lack of Er-cavity interaction. The low concentration of active erbium ions in crystalline silicon is the main reason for this lack of interaction between the emitting dipole and the cavity.

References

[1] A. Polman, “Erbium implanted thin film photonic materials,” J. Appl. Phys. 82, 1 (1997).

[2] H. Efeoglu, J. H Evans, T. E Jackman, B. Hamilton, D. C Houghton, J. M Langer, A. R Peaker, D. Perovic, I. Poole, N. Ravel, P. Hemment, and C. W. Chan, “Recombination processes in erbium-doped MBE silicon,” Semicond. Sci. Technol. 8, 236 (1993).

[3] D. J. Eaglesham, J. Michel, E. A. Fitzgerald, D. C. Jacobson, J. M. Poate, J. L. Benton, A. Polman, Y.-H. Xie, and L. C. Kimerling, “Microstructure of erbium‐implanted Si,” Appl. Phys. Lett. 58, 2797 (1993).

[4] J. D. Carey, R. C. Barklie, J. F. Donegan, F. Priolo, G. Franzò, and S. Coffa, “An EPR study of Er-impurity Complexes in Si,” J. Lumin. 80, 297 (1998).

[5] P. Liu, J. P. Zhang, R. J. Wilson, G. Curello, S. S. Rao, and P. L. F. Hemment, “ Effect of fluorine co−implantation on MeV erbium implanted silicon,” Appl. Phys. Lett. 66, 3158 (1995).

[6] F. Priolo, G. Franzò, S. Coffa, A. Polman, S. Libertino, R. Barklie, and D. Carey, “The erbium‐impurity interaction and its effects on the 1.54 μm luminescence of Er^{3+} in crystalline silicon,” J. Appl. Phys. 78, 3874 (1995).

[7] K. Srinivasan and O. Painter, “Optical fiber taper coupling and high-resolution wavelength tuning of microdisk resonators at cryogenic temperatures,” Appl. Phys. Lett. 90, 031114 (2007).

[8] M. Miritello, R. Lo Savio, F. Iacona, G. Franzò, A. Irrera, A. M. Piro, C. Bongiorno, and F. Priolo, “Efficient luminescence and energy transfer in erbium silicate thin films,” Adv. Mater. 19, 1582-1588 (2007).

[9] K. Suh, M. Lee, J. S. Chang, H. Lee, N. Park, G. Y. Sung, and J. H. Shin, “Cooperative upconversion and optical gain in ion-beam sputter-deposited $Er_xY_{2-x}SiO_5$ waveguides,” Opt. Express 18, 7724-7731 (2010).

[10] Y. Yin, W. J, Xu, F. Wei, G. Z. Ran, G. G. Qin, Y. F. Shi, Q. G. Yao, and S. D. Yao, “Room temperature Er^{3+} 1.54 μm electroluminescence from Si-rich erbium silicate deposited by magnetron sputtering,” J. Phys. D: Appl. Phys. 43, 335102 (2010).

[11] R. Lo Savio, M. Miritello, A. M. Piro, F. Priolo, and F. Iacona, “The influence of stoichiometry on the structural stability and on the optical emission of erbium silicate thin films,” Appl. Phys. Lett. 93, 021919 (2008).

[12] M. Galli, S. L. Portalupi, M. Belotti, L. C. Andreani, L. O’Faolain, T. F. Krauss, “Light scattering and Fano resonances in high-Q photonic crystal nanocavities,” Appl. Phys. Lett. 94, 071101 (2009).

[13] S. Iwamoto, Y. Arakawa, and A. Gomyo, “Observation of enhanced photoluminescence from silicon photonic crystal nanocavity at room temperature,” Appl. Phys. Lett. 91, 211104 (2007).

[14] R. Lo Savio, S. L. Portalupi, D. Gerace, A. Shakoor, T. F. Krauss, L. O’Faolain, L. C. Andreani, and M. Galli, “Room-temperature emission at telecom wavelengths from silicon photonic crystal nanocavities,” Appl. Phys. Lett. 98, 201106 (2011).

[15] W. J. Miniscalco, “Erbium-Doped glasses for fiber amplifiers at 1500 nm,” J. Lightwave Technol. 9, 234-250 (1991).

[16] M. Miritello, R. Lo Savio, P. Cardile, and F. Priolo, “Enhanced down conversion of photons emitted by photoexcited $Er_xY_{2-x}Si_2O_7$ films grown on silicon,” Phys. Rev. B 81, 041411(R) (2010).

[17] H.-S. Hsu, C. Cai, and A. M. Armani, “Ultra-low-threshold Er:Yb sol-gel microlaser on silicon,” Opt. Express 17, 23265-23271 (2009).

[18] M. Miritello, P. Cardile, R. Lo Savio, and F. Priolo, “Energy transfer and enhanced 1.54 μm emission in erbium-ytterbium disilicate thin films,” Opt. Express 19, 20761-20772 (2011).

[19] E. Snoeks, P. G. Kik, and A. Polman, “Concentration quenching in erbium implanted alkali silicate glasses,” Opt. Mater. 5, 159-167 (1996).

[20] L. C. Andreani, G. Panzarini, J. M. Gerard, “Strong-coupling regime for quantum boxes in pillar microcavities: Theory,” Phys. Rev. B 60, 13276-13279 (1999).

[21] M. J. Weber, “Radiative and multiphonon relaxation of Rare-Earth ions in Y_2O_3,” Phys. Rev. 171, 283-291 (1968).

[22] E. M. Purcell, “Spontaneous emission probabilities at radio frequencies,” Phys. Rev. 69, 674–674 (1946).

[23] Q. Xu, V. R. Almeida, R. R. Panepucci, and M. Lipson, “Experimental demonstration of guiding and confining light in nanometer-size low-refractive-index material,” Opt. Lett. 29, 1626-1628 (2004).

Chapter 8

Conclusions

In this PhD project, I have successfully demonstrated an all-silicon nanolight source that operates at room temperature. I have achieved this success by combining emission enhancement in the silicon material with optical enhancement via the Purcell effect.

With the support of my collaborators at the University of Pavia and Catania, Italy, I was able to take three routes to increase emission from silicon. The possibility of enhancing the emission further by using a photonic crystal cavity for all three cases was also investigated.

The first route was the incorporation of defects into the silicon host by hydrogen plasma treatment and ion implantation. From transmission electron microscopy (TEM) studies of the treated samples, we concluded that hydrogen plasma treatment creates three types of defect, namely nano-bubbles, platelets and coffee-bean shaped dislocation loops. The nano-bubbles have a diameter of few nanometers and are located within 10 nm of the top surface. The platelets have a mean diameter of 10-15 nm and are created deeper than the nano-bubbles and are oriented in the (100) and (111) direction. The coffee-bean shaped dislocation loops are located in the area between the nano-bubbles and the platelets. Hydrogen implantation creates platelets only. From the photoluminescence data, we concluded that the hydrogen plasma treatment creates two PL bands, which are centered at 1300 and 1500 nm. On the other hand, only a 1300 nm band is created by the implantation. Comparing the PL spectra of the treated samples with the TEM images, we concluded that the 1500 nm band is formed due to the creation of nano-bubbles, while the platelets are responsible for the formation of the 1300 nm band. Annealing out the defects and studying its effect on the intensity of the PL bands further confirm this.

I carried out a detailed analysis of the effect of plasma treatment on the PL and Q-values of the PhC cavities. Different plasma compositions and treatment parameters were used in the reactive ion etching setup. I found that the PL level increases up to a treatment duration of 30-45 minutes at a power of 20-40 W, after which the PL level saturates. Further treatment reduces the PL level due to excess physical damage. The

maximum PL enhancement of 2 orders of magnitude was achieved when pure hydrogen was used. The use of pure hydrogen has the additional benefit of increasing the Q-factors of the PhC cavity. I noticed that the hydrogen plasma treatment polishes the side walls of the PhC, causing an increase in the Q-factors by reducing the scattering losses. This reduction of the surface roughness was confirmed by surface roughness analysis of the treated samples using an atomic force microscope (AFM). For this purpose, I used silicon on insulator samples but similar results would be obtained for the PhC side walls. The addition of argon ions to elucidate the defect formation is found out to be detrimental, as it causes physical damage to the PhC and reduces the Q-factors drastically. Furthermore, I found out that the emission enhancement is only obtained when the plasma contains hydrogen gas. From all the experimental studies, I conclude that hydrogen plays three important roles in the emission enhancement process. Firstly, it creates physical defects, secondly, it decorates the defects and thirdly, it passivates non-radiative recombination centres. This conclusion is further supported by the fact that light emission from hydrogen implanted samples requires hydrogen exposure by forming gas annealing in order to achieve emission enhancement.

I fabricated L3 PhC cavities on SOI wafer with optically active defects. The defects feed the cavity and the emission is enhanced by a factor of 300 compared to the PL level of SOI at the corresponding wavelengths. The emission is then enhanced by a further 2 orders of magnitude by hydrogen plasma treatment. An additional 5-fold enhancement can be achieved by annealing the samples in the forming gas at 300 ^{o}C for 30 min. Altogether; this yields an impressive 150,000-fold enhancement. In addition to the emission enhancement, the Purcell effect has the additional benefit of providing temperature stability by reducing the radiative lifetime of the carriers.

By separating the light extraction effect from the total emission enhancement, a Purcell factor of 10-12 is calculated, which is a very respectable value – many theoretical papers claim much higher values being achievable, but realising high Purcell factors experimentally is much more elusive. Time resolved lifetime measurements were carried out to obtain a more accurate estimate of the Purcell factor. These lifetime measurements gave a clear indication of lifetime reduction on-resonance, but were unfortunately limited by the time-response of the system. However, from these

experiments, we conclude that the upper limit of the lifetime is around 1 ns, which is quite remarkable.

By creating a *pin* junction around the cavity, I was also able to demonstrate an electrically pumped silicon light source. This was achieved by placing the cavity inside a *pn* junction. The collected emitted power from this device is 45 pW, when integrated over the entire spectrum and 5 pW, when integrated over the fundamental peak. The power spectral density of the device is hence, 10 pW/nm, the highest value reported for any silicon emitter reported to date.

Using the silicon light source developed in this project, I have also demonstrated refractive index sensing. The spectral shift of the emission peak was measured by the change of the refractive index surrounding the cavity. Using an on-chip internal light source instead of an external laser simplifies the sensor architecture, although the low emission power demands the use of a high quality detector; with further improvements in output power, we hope that simpler detectors can be used in due course. A sensitivity of 555 nm/RIU was measured, which is comparable to PhC based sensors, demonstrated in the end-fire coupled scheme. I also discussed some proposals for extending the use of this device for biological sensing to demonstrate an all-silicon lab-on-a-chip biological sensor.

The second approach to enhance silicon light emission was to create a narrow emission line in the SOI by carbon implantation. An intense and narrow emission line at 1280 nm (“G-line”) was successfully created by carbon implantation. Carbon implantation creates the G-line emission, but the emission intensity is low when the implantation is performed in a structured PhC cavity in comparison to the same in SOI. We believe that this poor performance is due to the short lifetime of the carriers at the etched side walls, compared to the much longer G-line emission lifetime, which is in the microseconds range. Thus, I conclude that the advantage of the Purcell effect cannot be obtained for photonic crystal cavities in G-line material unless the problem of G-line quenching due to surface recombination is solved.

The third approach for creating emission from the material was to dope silicon with erbium and to couple the emission to the PhC cavity. Unfortunately, no Er-cavity interaction was observed. We then used lifetime measurements to confirm the lack of the Purcell effect in the Er-PhC cavity scheme. The low erbium concentration, lack of

active erbium ions and saturation of erbium at very low pump powers are considered to be the main problems in this scheme. We concluded that an approach to enhance the silicon emission by making PhC cavities in erbium doped silicon would not be successful. Alternatively, we developed another approach whereby a thin layer of erbium compound (yttrium-erbium, Y-Er) was deposited on top of an L3 PhC cavity. In Y-Er, a higher Er concentration can be achieved compared to crystalline silicon due to the higher erbium solubility. With careful optimization of doping conditions, we achieved doping concentration of 10^{20} Er/cm^3, compared to a limit of order 10^{17} Er/cm^3 for erbium in silicon. This high concentration of the erbium ions increases the probability of higher concentration of active ions and allowed the interaction of the emitting dipole and the cavity. The interaction was confirmed by time resolved lifetime measurements, from which the value of the Purcell factor was extracted to be 2.2, very close to the theoretically calculated value of 3.2. This value was lower than that observed for the hydrogen-plasma treated cavities as the active film is now situated on top of the cavity, and the overlap with the mode is much lower. The output power of this device was measured to be 85 pW.

The comparison of the three approaches is given in Table C.1 below.

Table C.1 Comparison of silicon light sources made by taking three different routes.

Sr No	Features	Hydrogen defects in PhC cavity	G-line in PhC cavity	Y-Er film on top of PhC cavity
1	Room temperature	✓	×	✓
2	Electrical pumping	✓	×	×
3	Small size	✓	✓	✓
4	Sub-bandgap emission	✓	✓	✓
5	Narrow emission line	✓	✓	✓
6	Tunability	✓	×	×
7	Output power >10 µW	×	×	×

From the comparison provided in Table C.1, I conclude that the approach of utilizing the optically active hydrogen defects is more promising than the other two as it satisfies the maximum number of desired features. The only area, which needs

improvement is the output power level, which at present is 5 pW. Although this seems low but considering that it is based on an indirect bandgap material, it is still a descent level. Furthermore, it has almost the same output power and only a magnitude lower efficiency compared to light sources made by using direct bandgap materials having the same configuration. The low performance of electrically pumped direct bandgap PhC based light sources is due to surface recombination.

The silicon nanolight sources developed in this project can be used in those applications where higher powers are not required, e.g. biological sensing. For on-chip communications however, at least a microwatt power level is required. Thus, there is a need to continue this research to increase the output power levels.

Future work

The results achieved in all three approaches are promising and are worth pursuing further as there is a margin for improvement. I suggest the following steps that can be taken as a future work:

1. **For approach I - Hydrogen defects in silicon**

   i. Use the cavities with higher Q/V values with suitable far-field optimization to increase the enhancement by the Purcell effect.

   ii. The cavities I used in this project had very small mode volume. This gives a benefit in terms of higher Purcell factor but is a limitation on the higher output power. A suitably designed coupled cavity scheme, which is a promising route to combine large mode volumes while keeping the Purcell factor high is worth trying.

   iii. As the emission induced by hydrogen plasma treatment is overall very broad, only a small fraction of emitters are on resonance with the cavity and contributing to the overall output power. An investigation to develop a way to narrow down the band would be a step forward.

2. **For approach II - G-line**

The G-line intensity reduces drastically when the silicon layer containing the G-centres is etched. Thus, an alternate approach is required to avoid silicon etching. The following two proposals are worth exploring:

i. Making polymer waveguides on top of the silicon to form strip loaded silicon waveguides. The Bragg mirrors having high reflectivity at the G-line wavelength can be fabricated at the end of the waveguides to form a cavity. This configuration has the potential to demonstrate optical gain by using the G-line.

ii. Making a suitably designed ring resonator on top of the silicon layer that contains the G-centres. Amorphous silicon can be deposited on top, which could be etched to form the resonator, designed to be on resonance with the G-line.

3. For approach III - Erbium disilicate film

i. Increase the overlap between the emitters and the cavity mode. One way of doing this is using slotted PhC cavities. By optimizing the deposition of Er-Y, the film could infiltrate into the slot, giving a better mode overlap.

ii. Second approach could be to use ytterbium-Er instead of yttrium-Er, which has an order of magnitude higher excitation cross section.